

University of Alberta

**The Effects of Natural Convection and Wind on Water  
Vapour Transport from a Porous Medium: Application to  
Water Transport on Mars**

by

Alireza Farahani Nia



A thesis submitted to the Faculty of Graduate Studies and Research in partial  
fulfillment of the requirements for the degree of Master of Science

Department of Mechanical Engineering

Edmonton, Alberta

Fall 2008



Library and  
Archives Canada

Bibliothèque et  
Archives Canada

Published Heritage  
Branch

Direction du  
Patrimoine de l'édition

395 Wellington Street  
Ottawa ON K1A 0N4  
Canada

395, rue Wellington  
Ottawa ON K1A 0N4  
Canada

*Your file* *Votre référence*

*ISBN: 978-0-494-47249-1*

*Our file* *Notre référence*

*ISBN: 978-0-494-47249-1*

**NOTICE:**

The author has granted a non-exclusive license allowing Library and Archives Canada to reproduce, publish, archive, preserve, conserve, communicate to the public by telecommunication or on the Internet, loan, distribute and sell theses worldwide, for commercial or non-commercial purposes, in microform, paper, electronic and/or any other formats.

The author retains copyright ownership and moral rights in this thesis. Neither the thesis nor substantial extracts from it may be printed or otherwise reproduced without the author's permission.

**AVIS:**

L'auteur a accordé une licence non exclusive permettant à la Bibliothèque et Archives Canada de reproduire, publier, archiver, sauvegarder, conserver, transmettre au public par télécommunication ou par l'Internet, prêter, distribuer et vendre des thèses partout dans le monde, à des fins commerciales ou autres, sur support microforme, papier, électronique et/ou autres formats.

L'auteur conserve la propriété du droit d'auteur et des droits moraux qui protègent cette thèse. Ni la thèse ni des extraits substantiels de celle-ci ne doivent être imprimés ou autrement reproduits sans son autorisation.

---

In compliance with the Canadian Privacy Act some supporting forms may have been removed from this thesis.

Conformément à la loi canadienne sur la protection de la vie privée, quelques formulaires secondaires ont été enlevés de cette thèse.

While these forms may be included in the document page count, their removal does not represent any loss of content from the thesis.

Bien que ces formulaires aient inclus dans la pagination, il n'y aura aucun contenu manquant.



**Canada**

To my Father and Mother...  
...and to all the “giants” that I stood on their shoulders.

“I’m sure the universe is full of intelligent life. It’s just been too intelligent to come here!”, Arthur C. Clarke

“A central lesson of science is that to understand complex issues (or even simple ones), we must try to free our minds of dogma and to guarantee the freedom to publish, to contradict, and to experiment. Arguments from authority are unacceptable.”, Carl Sagan

“What we see of the real world is not the unvarnished real world but a *model* of the real world, regulated and adjusted by sense data, a model that is constructed so that it is useful for dealing with the real world.”, Richard Dawkins

# Abstract

Vapour transport in a gas saturated porous medium with surface convection occurs in many applications. For the Phoenix Mars mission, local convection over the regolith is studied to obtain a better insight into water vapour transport in the vicinity of the Lander. A 3-D, transient, transport model, extended to admit a layer of porous material is used to model two different local atmospheric flows: an early phase of the near surface natural convection and horizontal winds. Variable parameters are regolith thickness, domain pressure and temperature, imposed wind velocity (inflow) and surface temperature. The results of the numerical simulations are summarized by means of a special Sherwood number to quantify these complex effects. Theoretical and experimental data were used to partially validate the numerical simulations. Lastly, experiments were performed to investigate the effects of surface natural convection on vapour transport in a porous medium to partially validate the numerical model.

# Acknowledgements

I wish to sincerely thank all the people who made this thesis possible.

First and foremost, my deepest gratitude is given to my supervisor and mentor, Dr. Carlos F. Lange, whom his patience, kindness, openness and insight has supported me throughout this work. I will forever cherish the invaluable bond between us.

I would like to gratefully thank Prof. Mark Ackerman. His experience, patience, knowledge and his magic finger greatly contributed to the conclusion of this work. Also I would like to thank Prof. John D. Wilson, my thesis examiner, for his much valuable suggestions and corrections to my thesis.

I wish to thank my undergraduate professors at the University of Tehran, Drs. Ashjaee, Nikkhah-Bahrami, Sadeghi, Noori and especially Dr. Farshad Kowsary, for they have built the foundation of my engineering knowledge. I would like to thank my professors at the University of Alberta, Dr. Peter Flynn and Dr. Tony Yeung for the incredible knowledge and inspiration that they have provided me.

I gratefully acknowledge the assistance and support of the department of mechanical engineering staff at the University of Alberta. Machine shop staff: Roger Marchand, Rick Bubenko, Liana Ireland, Tuula Hilvo, Greg Miller and especially Bernie Faulkner (always knows how to do things). Electronics staff: Terry Nord and especially Rick Conrad (a miracle for this thesis). The IT technicians: Wayne Pittman, Alan Wilson, Ravina Brar and Jonathan Clark. Office staff: Gail Anderson, Amanda Webb, Donna Waring and especially Linda Paulic, Linda Kelly and Ayako Ohtake (also very fun friends).

I would like to sincerely thank my Labmates, who are also my best friends, Rocky Chen and Jakob Zubik, for all the help and super-fun moments that they have provided me. Also my student-friends at the department: Roberto Gallardo, Anwar Hasan, Nima Usefi, Vahid Hosseiny, Sina Ghaemi and especially Aydin Jafarnejad, Alireza Monfared, Ahmad Ghazi, Farshid Chini and Mahdi Shahbakhti for all the fun times and inspirational conversations that we shared together.

Most specially, I extend my sincerest gratitude to my best friend, Lisa Gosset. She has shown me the meaning of love and has always, endlessly supported me with her special warm fuzzies through times when everything seemed impossible. Lisa, you gave me courage, hope and confidence when I needed most.

Most importantly, with all my heart, I wish to thank my Father, Mother and my sister Ellie, for the infinite support that they have provided me. Father, you are my true hero and you have always been the main inspiration of my life. Mother, I will never forget that you have literally been my first teacher.

Gratefully, I acknowledge the financial support from the Canadian Space Agency (CSA) and the National Sciences and Engineering Research Council of Canada (NSERC).

# Contents

<b>1</b>	<b>Introduction</b>	<b>1</b>
1.1	Mars . . . . .	4
1.2	Study of Water Transport on Mars . . . . .	6
1.3	The Martian Regolith . . . . .	9
1.4	The Martian Atmosphere . . . . .	15
1.5	Surface Net Solar Irradiation at the Atmosphere-Regolith Interface . . . . .	19
<b>2</b>	<b>Theory</b>	<b>23</b>
2.1	Modelling Atmospheric Flows on Mars . . . . .	23
2.1.1	Winds . . . . .	23
2.1.2	Natural Convection . . . . .	27
2.2	Modelling Water Vapour Transport in the Martian Regolith . . . . .	33
2.2.1	Porous Media . . . . .	34
2.2.2	Water Vapour Diffusion in CO <sub>2</sub> . . . . .	36
2.2.3	Water Vapour Diffusion in the Martian Regolith . . . . .	38
2.3	Numerical Method . . . . .	42
2.3.1	Numerics in Fluid Mechanics . . . . .	42
2.3.2	Solving with CFX . . . . .	43
2.3.3	Winds and Natural Convection Transport Equations in CFX . . . . .	43
2.3.4	Meshing . . . . .	44
2.3.5	Discretization of the Transport Terms . . . . .	46
2.3.6	Solving the Algebraic Equations and Convergence . . . . .	47
2.3.7	Grid and Domain Independence . . . . .	48

2.4	The Special Sherwood Number . . . . .	50
<b>3</b>	<b>Numerical Simulations</b>	<b>52</b>
3.1	Horizontal Winds . . . . .	52
3.1.1	Effect of Wind Velocity and Regolith Depth . . . . .	67
3.1.2	Effect of Pressure . . . . .	70
3.1.3	Effect of Temperature . . . . .	71
3.1.4	Laminar Assumption versus the $k-\epsilon$ Turbulence Model . . . . .	75
3.1.5	The Special Sherwood Number for Horizontal Winds . . . . .	79
3.1.6	Grid and Domain Independence Analysis . . . . .	82
3.2	Effect of Local Natural Convection on Water Vapour Transport . . . . .	84
3.3	Partial Theoretical Validation of the Numerical Model . . . . .	85
3.3.1	One Dimensional Model Validation . . . . .	85
3.3.2	An Informative Larger Scale Two Dimensional Simulation of the Atmosphere . . . . .	87
3.3.3	Natural Convection Model Validation . . . . .	90
3.3.4	Selection of a Proper Turbulence Model . . . . .	93
3.3.5	Case studies . . . . .	98
<b>4</b>	<b>Experimental Validation</b>	<b>101</b>
4.1	The Experimental Setup . . . . .	102
4.1.1	The Water Tank . . . . .	103
4.1.2	The Natural Convection Enclosure . . . . .	104
4.1.3	Measurements and Electronics . . . . .	106
4.1.4	Hydraulics . . . . .	109
4.2	Calibration Procedure . . . . .	109
4.2.1	Thermocouples . . . . .	109
4.2.2	Humidity and Temperature Sensors . . . . .	110
4.2.3	The Scale . . . . .	112
4.3	Experiments . . . . .	112
4.3.1	First Series . . . . .	113



4.3.2	Second Series . . . . .	125
4.4	Numerical Model Validation . . . . .	127
4.4.1	Numerical Setup . . . . .	127
4.4.2	Results . . . . .	130
<b>5</b>	<b>Conclusions</b>	<b>137</b>
	<b>Bibliography</b>	<b>141</b>
	<b>Appendix</b>	<b>152</b>
<b>A</b>	<b>Humidity/Temperature Sensor Calibration Data</b>	<b>152</b>

# List of Tables

1.1	$G_s$ ( $\text{W m}^{-2}$ ) for different albedo and optical depths at the starting and ending $L_s$ of the Phoenix mission. As mentioned previously, these values for $\tau_o$ and $a$ (especially $a=0.23$ ) have been used in literature to represent the values at the Lander's site. . . . .	22
2.1	Effective diffusion coefficients ( $D_{eff}$ , $\text{cm}^2 \text{s}^{-1}$ ) for samples of 40-70 $\mu\text{m}$ Glass Beads at different regolith depths, pressures and temperatures from experimental work of Hudson et al. [2007] . . . . .	41
3.1	Transport properties of $\text{CO}_2$ air used in the numerical simulation. . .	62
3.2	Effective molecular diffusion coefficients ( $D_{eff}$ , $\text{cm}^2 \text{s}^{-1}$ ) of water vapour in the regolith for samples of 40-70 $\mu\text{m}$ Glass Beads at different regolith depths, pressures and temperatures. Rounded, linearly interpolated or extrapolated from experimental work of Hudson et al. [2007]. . . . .	62
3.3	Surface integral of water vapour density at a horizontal plane 5 mm above the surface, calculated at four grid levels. . . . .	82
3.4	Comparison of the average Nusselt number at the cold wall for simulation flow models and the experimental result from Leong et al. [1998].	93
3.5	Special Sherwood numbers ( $\overline{\text{Sh}}^*$ ) for the natural convection cases. . .	99
3.6	Surface integral of water vapour density at a horizontal plane 5 mm above the surface, calculated at three grid levels. . . . .	100
4.1	Transport properties used in the numerical simulation for air at 35°C.	129
4.2	Thermal properties used in the numerical simulation for air at 35°C. .	129
4.3	The foam properties. . . . .	129

A.1	Regression coefficients for sensors 1 to 32. . . . .	152
A.2	Regression coefficients for sensors 33 to 64. . . . .	153
A.3	Regression coefficients for sensors 65 to 96. . . . .	153
A.4	Regression coefficients for sensors 97 to 128. . . . .	154

# List of Figures

2.1	The tetrahedra element. . . . .	45
2.2	An illustration of the local locations of interest for calculating $Sh^*$ . . .	51
3.1	View of the unstructured tetrahedra mesh with local structured refinement used for the horizontal winds domain. . . . .	53
3.2	A detailed view of the local structured refinement at the atmosphere-regolith interface, used for the horizontal winds domain. . . . .	54
3.3	Example of an interpolated velocity profile at the domain inlet boundary with the Akima interpolation scheme. (case of $10 \text{ m s}^{-1}$ free stream velocity). . . . .	56
3.4	Example of an interpolated velocity profile at the domain inlet boundary with a 2nd order polynomial (case of $10 \text{ m s}^{-1}$ free stream velocity). . . . .	57
3.5	Example of an interpolated velocity profile at the domain inlet boundary with the Spline interpolation scheme (case of $10 \text{ m s}^{-1}$ free stream velocity). . . . .	57
3.6	Horizontal velocity ( $U_x$ ) at 2 m above the surface versus the free stream velocity of the original inlet wind profiles. . . . .	58
3.7	Horizontal velocity ( $U_x$ ) at 2 m above the surface versus the free stream velocity of the inlet wind profiles. . . . .	58
3.8	Horizontal velocity ( $U_x$ ) profiles for 0.5, 1, 2, 5, 10, 20, 35 $\text{m s}^{-s}$ winds. . . . .	59
3.9	The local scale domain for the horizontal wind simulations. . . . .	60
3.10	The location of planes where $U_x^*$ (plane A) and water vapour concentration (plane B) are calculated at, in the horizontal winds domain. . . . .	61

3.11 Water vapour contours in the domain. Case-1: no wind, $T=263$ K, $P=600$ Pa, 10 cm thick porous regolith. Elevation “0” is the regolith surface. . . . .	63
3.12 Water vapour contours in the domain. Case-0: no wind, $T=263$ K, $P=600$ Pa, 10 cm thick fluid “regolith”. Elevation “0” is the “regolith” surface. . . . .	64
3.13 Detailed water vapour contours in the regolith. Case: no wind, $T=263$ K, $P=600$ Pa, 10 cm thick porous regolith. . . . .	64
3.14 Detailed water vapour contours in the “regolith”. Case: no wind, $T=263$ K, $P=600$ Pa, 10 cm thick fluid “regolith”. . . . .	65
3.15 Water vapour amount along a line at the middle of the domain. Case: no wind, $T=240$ K, $P=800$ Pa, 10 cm thick porous regolith. . . . .	65
3.16 Water vapour amount along a line at the middle of the domain. Case: no wind, $T=240$ K, $P=800$ Pa, 10 cm thick fluid “regolith”. . . . .	66
3.17 Velocity magnitude profile on a plane at the middle of the domain along the wind direction. Case: $10\text{ m s}^{-1}$ free stream wind, $T=263$ K, $P=600$ Pa, 5 cm thick regolith. . . . .	67
3.18 Water vapour logarithmic contours on a plane at the middle of the domain along the wind direction. Case: $10\text{ m s}^{-1}$ free stream wind, $T=263$ K, $P=800$ Pa, 5 cm thick regolith. . . . .	68
3.19 Average water vapour concentration versus laminar wind velocity and regolith depth. In the domain, $T=263$ K and $P=600$ Pa. . . . .	69
3.20 Average water vapour flux versus laminar wind velocity and regolith depth. In the domain, $T=263$ K and $P=600$ Pa. . . . .	70
3.21 Average water vapour flux versus the regolith thickness. In the domain, $T=263$ K, $P=600$ Pa and the turbulent wind velocity is $5\text{ m s}^{-1}$ . . . . .	70
3.22 Average water vapour concentration versus laminar wind velocity and domain pressure. In the domain, $T=263$ K and the regolith depth is 5 cm. . . . .	71

3.23	Average water vapour flux versus laminar wind velocity and domain pressure. In the domain, $T=263$ K and the regolith depth is 5 cm. . .	72
3.24	Average water vapour concentration versus laminar wind velocity and regolith depth. In the domain, $T=253$ K and $P=600$ Pa. . . . .	73
3.25	Average water vapour concentration versus laminar wind velocity and domain temperature. Regolith depth is 5 cm. . . . .	73
3.26	Average water vapour flux versus laminar wind velocity and regolith depth. In the domain, $T=253$ K and $P=600$ Pa. . . . .	74
3.27	Average water vapour flux versus laminar wind velocity and domain temperature. Regolith depth is 5 cm. . . . .	74
3.28	Velocity magnitude profile on a plane at the middle of the domain along the wind direction. Case: $20 \text{ m s}^{-1}$ free stream wind, $T=263$ K, $P=600$ Pa, 5 cm thick regolith. . . . .	77
3.29	Average water vapour flux versus wind velocity. Comparison of the $k-\epsilon$ model with a laminar assumption. $T=263$ K and $P=600$ Pa. . . . .	77
3.30	Average water vapour concentration versus turbulent wind velocity and regolith depth. $T=263$ K and $P=600$ Pa. . . . .	78
3.31	Average water vapour flux versus turbulent wind velocity and regolith depth. $T=263$ K and $P=600$ Pa. . . . .	78
3.32	Special Sherwood number versus laminar wind velocity and regolith depth. $T=263$ K and $P=600$ Pa. . . . .	80
3.33	Special Sherwood number versus laminar wind velocity and domain pressure. In the domain, $T=263$ K and the regolith depth is 5 cm. . .	80
3.34	Special Sherwood number versus laminar wind velocity and domain temperature. In the domain, $P=600$ Pa and the regolith depth is 5 cm.	81
3.35	Surface integral values of water vapour at different grid levels. . . . .	83
3.36	1-D resistance diagram of a heat transfer model from the regolith surface to the atmosphere and the ice-table. . . . .	86
3.37	Thermal plumes rising in the near surface atmosphere after 60 s of solar irradiation. . . . .	88

3.38	Velocity vectors in the near surface atmosphere after 170 s of solar irradiation. . . . .	89
3.39	The numerical domain of the experimental configuration of Ampofo and Karayiannis [2003]. . . . .	90
3.40	Comparison of temperature profiles along $X=x/L$ at mid length and height across the cavity, between the hot and cold walls. . . . .	91
3.41	Comparison of the local Nusselt number along $Y=y/L$ at the middle of the hot wall. . . . .	92
3.42	Numerical local domain for surface natural convection simulations. . .	95
3.43	Thermal plumes rising in the near surface atmosphere after 12 s of solar irradiation. . . . .	96
3.44	Velocity vectors in the near surface atmosphere after 12 s of solar irradiation. . . . .	96
3.45	Water vapour concentration in the near surface atmosphere after 60 s of solar irradiation. . . . .	96
3.46	Logarithmic contours of water vapour concentration in the near surface atmosphere for the case of pure linear diffusion. . . . .	97
3.47	Average water vapour concentration on a plane at 5 mm above the surface versus heat source at the surface and the regolith depth. . . .	98
3.48	Average water vapour flux versus heat source at the surface and the regolith depth. . . . .	99
3.49	Average water vapour values at different grid levels. . . . .	100
4.1	Diagram of the experiment setup . . . . .	103
4.2	Diagram of the water tank . . . . .	104
4.3	The heat flux calculated as a fraction of Intensity along the table length. 105	
4.4	Diagram of roof showing placement of coils and direction of flow in the troughs. . . . .	106
4.5	Diagram of the electronics layout. . . . .	108
4.6	Diagram of the sensor cable path in the tank. . . . .	108

4.7	The experimental setup. . . . .	109
4.8	Control temperatures measured by thermocouples at various locations.	115
4.9	Control temperatures measured by sensors at various locations in the room. . . . .	115
4.10	Water vapour density measured by sensors at various locations in the room. . . . .	115
4.11	Control temperatures measured by sensors at various locations in the enclosure. . . . .	116
4.12	Water vapour density measured by sensors at various locations in the enclosure. . . . .	116
4.13	Instantaneous tank weight during the experiment period. . . . .	116
4.14	Linearized instantaneous tank weight during the experiment period. .	117
4.15	Temperatures measured by several sensors located under the foam in the middle of the tank. . . . .	119
4.16	Temperatures measured by several sensors located between the two foam layers in the middle of the tank. . . . .	120
4.17	Temperatures measured by several sensors located at the foam surface in the middle of the tank. . . . .	120
4.18	Water vapour density measured by several sensors located under the foam in the middle of the tank. . . . .	121
4.19	Water vapour density measured by several sensors located between the two foam layers in the middle of the tank. . . . .	121
4.20	Water vapour density measured by several sensors located at the foam surface in the middle of the tank. . . . .	122
4.21	Layer averaged temperatures of several sensors located in the middle of the tank. . . . .	122
4.22	Layer averaged water vapour density of several sensors located in the middle of the tank, sample 1. . . . .	123
4.23	Layer averaged water vapour density in the foam comparison for after and before the surface heating of the foam. . . . .	123



4.24	Layer averaged water vapour density of several sensors located in the middle of the tank, sample 2. . . . .	124
4.25	Control temperatures measured by thermocouples at various locations, series 2. . . . .	125
4.26	Instantaneous tank weight during the experiment period, series 2. . .	126
4.27	Temperatures measured by several sensors located at the foam surface in the middle of the tank, series 2. . . . .	126
4.28	Water vapour density measured by several sensors located at the foam surface in the middle of the tank, series 2. . . . .	126
4.29	The 3-D model of the experiment setup and the mesh at the ZX plane.	128
4.30	Thermal plumes and the transport of heat after 120 s of surface heating is evident from this temperature contour. . . . .	132
4.31	Initial water vapour density contour in the domain. . . . .	132
4.32	Water vapour density contour in the domain after 21 s of surface heating.	133
4.33	Velocity vectors in the XZ plane of the domain after 120 s of surface heating. . . . .	133
4.34	Velocity vectors in the YZ plane of the domain after 120 s of surface heating. . . . .	134
4.35	Streamlines in the domain and the foam surface temperature variation after 120 s of surface heating. . . . .	134
4.36	Water vapour density contour at a horizontal plane at the bottom of the foam. . . . .	135
4.37	Water vapour density contour at a horizontal plane in the middle height of the foam. . . . .	135
4.38	Water vapour density contour at a horizontal plane located at 1 mm under the foam surface. . . . .	136
4.39	Experimental, layer averaged, water vapour density profile in the foam compared to the profiles obtained from the numerical simulation at different times, on a vertical line in the middle of the foam. . . . .	136

# List of Symbols

$A$  = Area,  $\text{m}^2$

$a$  = Albedo

$C$  = Dimensionless constant

$C_{\text{material}}$  = Specific heat capacity of a material,  $\text{J kg}^{-1} \text{K}^{-1}$  or  $\text{J mol}^{-1} \text{K}^{-1}$

$C_{1\epsilon}$  = k- $\epsilon$  model constant = 1.44

$C_{2\epsilon}$  = k- $\epsilon$  model constant = 1.92

$C_{\mu}$  = k- $\epsilon$  model constant = 0.09

$c$  = Local speed of sound,  $\text{m s}^{-1}$

$d$  = Particle size

$D_{wa}$  = Binary air-water vapour diffusion coefficient,  $\text{m}^2 \text{s}^{-2}$

$D_{wc}$  = Binary  $\text{CO}_2$ -water vapour diffusion coefficient,  $\text{m}^2 \text{s}^{-2}$

$D_{12}$  = Binary diffusion coefficient for the component 1 into 2,  $\text{m}^2 \text{s}^{-2}$

$D_T$  = Thermal mass transfer diffusion coefficient,  $\text{m}^2 \text{s}^{-2}$

$D_P$  = Pressure mass transfer diffusion coefficient,  $\text{m}^2 \text{s}^{-2}$

$D_{\text{eff}}$  = The effective mass transfer diffusion coefficient,  $\text{m}^2 \text{s}^{-2}$

$e$  = Euler or Napier number,  $e=2.71828182845904523536$

$e_M$  = Mars' orbit eccentricity,  $e_M = 0.093377$

$f$  = A fitting parameter

$\vec{g}$  = Gravity vector,  $\text{m s}^{-2}$

$G_s$  = Sum of the direct solar and diffuse irradiation,  $\text{W m}^{-2}$

$Gr$  = Grashof number

$H$  = Height scale,  $\text{m}$

$h$  = Grid level

$h$  = Convective heat transfer coefficient,  $\text{W m}^{-2} \text{K}^{-1}$

$h_t$  = Total specific enthalpy,  $\text{m}^2 \text{s}^{-2}$

$h_s$  = Static specific enthalpy,  $\text{m}^2 \text{s}^{-2}$

$I$  = Thermal inertia,  $\text{J m}^{-2} \text{K}^{-1}$

$I_a$  = Direct solar irradiation at the top of the atmosphere,  $\text{W m}^{-2}$

$I_s$  = Direct solar irradiation at the surface,  $\text{W m}^{-2}$

$j$  = Diffusive flux,  $\text{kg s}^{-1}$

$K$  = Permeability,  $\text{m}^2$

$K_n$  = Knudsen number

$k$  = Turbulence kinetic energy,  $\text{m}^2 \text{s}^{-2}$

$k$  = Thermal conductivity,  $\text{W m}^{-1} \text{K}^{-1}$

$k_m$  = Mass transfer coefficient,  $\text{m s}^{-1}$

$L$  = Dimension scale, m  
 $L_s$  = Aerocentric longitude at the solar noon on Mars  
 $M$  = Mach number  
 $M_{CO_2}$  = molecular weight of  $CO_2$ , 44.01 g mol<sup>-1</sup>  
 $M_w$  = molecular weight of water, 18.01 g mol<sup>-1</sup>  
 $\dot{m}$  = Mass rate, kg s<sup>-1</sup>  
 $m_a$  = Air mass adjusting factor  
 $N$  = Total nodes  
 $Nu$  = Nusselt number  
 $n$  = Number of molecules  
 $O.F.$  = Obstruction factor in a porous medium  
 $P$  = Domain pressure, Pa  
 $p$  = Order of the numerical scheme  
 $PR$  = Precipitable water in microns (PR  $\mu m$ ),  $\mu m$   
 $Pr$  = Prandtl number  
 $Pr_t$  = Turbulent Prandtl number  
 $P_{sat}$  = Saturated pressure, Pa  
 $P'$  = Modified pressure, Pa  
 $q$  = Quartz content of dry soil  
 $r$  = Mixing ratio, ppm  
 $\bar{R}$  = Universal gas constant, 8314 J kmol<sup>-1</sup> K<sup>-1</sup>  
 $Ra$  = Rayleigh number  
 $Re$  = Reynolds number  
 $RH$  = Relative humidity  
 $S_i$  = Additional momentum sources, tensor notation  
 $\vec{S}_0$  = Additional momentum sources, vector notation  
 $S_\varphi$  = Additional sources of  $\varphi$   
 $Sc$  = Schmidt number  
 $Sc_t$  = Turbulent Schmidt number  
 $Sh$  = Sherwood number  
 $Sh^*$  = The special Sherwood number  
 $s_{CO_2}$  = Volume fraction of  $CO_2$  in soil pore space  
 $s_{H_2O}$  = Volume fraction of  $H_2O$  in soil pore space  
 $T$  = Domain temperature, K  
 $t$  = Time, s  
 $\vec{U}$  = Velocity vector, m s<sup>-1</sup>  
 $\vec{U}_g$  = Geostrophic wind velocity, m s<sup>-1</sup>  
 $\vec{U}_m$  = Time averaged velocity vector, m s<sup>-1</sup>  
 $\vec{u}$  = Time-varying fluctuating velocity vector, m s<sup>-1</sup>  
 $V$  = Total volume of the fluid mixture, m<sup>3</sup>

#### Greek symbols

$\alpha$  = Thermal diffusivity, m<sup>2</sup> s<sup>-1</sup>  
 $\beta$  = Thermal expansivity, K<sup>-1</sup>

$\Gamma_\phi$  = Diffusion coefficient of  $\phi$   
 $\gamma$  = Adiabatic index of a gas  
 $\delta$  = Declination angle  
 $\delta_0$  = Mars obliquity of rotation axis,  $\delta_0=24.936^\circ$   
 $\varepsilon$  = Emissivity  
 $\epsilon$  = Turbulence eddy dissipation rate,  $\text{m}^2 \text{s}^{-3}$   
 $\epsilon^d$  = Discretization error  
 $\mu$  = Dynamic viscosity, Pa s  
 $\mu_t$  = Eddy viscosity, Pa s  
 $\phi$  = Porosity  
 $\phi_l$  = Latitude  
 $\varphi$  = Conserved quantity per unit mass  
 $\Phi$  = Conserved quantity per unit volume  
 $\Psi_{ij}$  = quadratic pressure-strain correlation,  $\text{kg}/\text{m}\cdot\text{s}^3$   
 $\rho$  = Density,  $\text{kg m}^{-3}$   
 $\varrho$  = Density,  $\text{kg m}^{-3}$   
 $\rho_{air}$  = Air density,  $\text{kg m}^{-3}$   
 $\rho_{CO_2}$  =  $\text{CO}_2$  density,  $\text{kg m}^{-3}$   
 $\rho_w$  = Water vapour density,  $\text{kg m}^{-3}$   
 $\sigma$  = The Stefan-Boltzmann constant,  $\sigma = 5.7 \times 10^{-8} \text{ W m}^{-2} \text{ K}^{-4}$   
 $\sigma_k$  = k- $\epsilon$  model constant = 1.0  
 $\sigma_\epsilon$  = k- $\epsilon$  model constant = 1.3  
 $\sigma_{ij}$  = Stress tensor  
 $\Psi$  = Viscous stress tensor  
 $\tau$  = Tortuosity  
 $\tau_o$  = Optical depth  
 $\omega$  = Turbulence frequency  
 $\omega_h$  = Hour angle  
 $\omega_w$  = Mass fraction of water vapour

### System of coordinates

$x, y, z$  = Cartesian coordinate system  
 $X, Y, Z$  = Cartesian coordinate system  
 $i, j, k$  = index notation

### Overbar

- = average conditions; time mean; average surface integral

### Overarrow

$\rightarrow$  = vector

### Operators

$\nabla$  = Nabla

$\Delta$  = Delta, difference

$\partial_i = \frac{\partial}{\partial x_i}$

log = Logarithm to the base of 10

ln = Natural logarithm

# Chapter 1

## Introduction

The research work in this thesis investigates the effect of forced and natural convection on vapour transport in porous media with application to the water vapour transport mechanism on Mars.

Gas transport has long been an interesting topic for researchers, with the first studies dating back to 1829 in Thomas Graham's work. With these preliminary observations and after Adolf Fick introduced his law of diffusion, formulation of gas transport and the subject of transport by diffusion have been constantly progressing in many applications. With the advances in continuum mechanics, thermodynamics, statistical mechanics and molecular dynamics and kinetics, our knowledge of gas diffusion has increased significantly and many formulations and correlations have been developed for this kind of transport. When the diffusion mechanism takes place in a physically and mathematically complex domain (e.g. a porous domain) and is subject to physically complex conditions (very low pressures and temperatures, complex geometries, low gravity and temperature gradients), the correlations for simple diffusion are not valid any more. Therefore, implementing the basic diffusion formulas in such advanced applications will result in high levels of error.

In this study, focus is on the diffusion of a trace vapour in a porous domain that is saturated with a primary gas. This transport process is studied when the domain is subject to imposed horizontal winds of different velocities and to natural convection flows of different characteristics under both Earth ambient conditions and very low pressures and temperatures found on Mars. The initiative for such a detailed study of the gas diffusion mechanism

in this research project is the application to water vapour transport on Mars.

After the discovery of evidence of abundant water on Mars [Kieffer et al., 1976, Hecht, 2002, Mitrofanov et al., 2003, Christensen, 2006, Baker, 2006, Smith, 2008], the study of water transport on this planet has been pursued with great interest. This has led to different observations and theories on the history of water on Mars, its possible cycle on the planet and the forms of its existence and transport.

The dominant transport mechanism of water in the Martian soil is known to be the diffusion of water vapour, which occurs in a porous domain. On Mars, water transport takes place under very low temperatures (generally less than 240 K), low pressures (less than one hundredth of that on Earth), unsteady temperature gradients (caused by surface solar irradiation), winds and natural convective plumes [Smith et al., 2004, Lemmon et al., 2004] near the surface.

In this thesis, to study the three dimensional water vapour transport mechanism in the Martian soil, all the complexities mentioned above are mathematically implemented and then the resulting equations are numerically solved. The main motive to pursue a 3-D analysis is that, since the majority of the current transport models for Mars and its permafrost are 1-D [Mellon et al., 2004, Schorghofer and Aharonson, 2005], a more specific 3-D model can potentially resolve cases with complex geometries and provide a better understanding of the water vapour transport process.

In addition, to partially validate the numerical simulations, the water vapour transport mechanism was investigated with experiments. The experiments consist of water vapour diffusion through a porous medium having convective plumes at the surface. As an outcome of this study, the effects of some surface flows on vapour transport through a porous medium can be quantified.

Gas transport in porous media occurs in many scientific and industrial applications, such as subsurface contamination control, de-desertification and fuel cells [Litster et al., 2006]. These applications are further discussed below due to their importance and widespread use.

Subsurface contamination is usually caused by various volatile substances, which are transported through soil and contaminate water and natural reservoirs. Contaminations can

originate from many common sources, e.g. pesticides and fertilizers, industrial waste disposal, commercial and residential discharges and oil-sand waste from processing facilities. The transport of these contaminants in the soil is mainly due to diffusion. In order to control and constrain contaminant spreading, an accurate and thorough understanding of the diffusion process and the effect of surface flows on its transport is required.

Desert treatment and desert cultivation requires salt and harmful ore removal and irrigation. Such activities are expensive and require a great amount of water. Therefore, transport of water in the soil needs to be controlled. The more accurately the water transport is modeled, the better the outcome in terms of food production and water preservation.

On the other hand, in the case of landing missions on Mars, which is the main application of this study, it is necessary to have as much information as possible about the landing site. Knowledge about the landing site will assist in the general design of the lander, operation procedure and the measurement instruments that it could utilize during its mission. For example, a three dimensional model which simulates the flow conditions at the landing site, in a domain where scale is close to the order of magnitude of the lander, would give a better insight into the parameters that would affect its measurements.

With detailed knowledge of the landing site, the transport model can be used to estimate the effect of winds and thermal plumes on the water vapour transport through the soil, one of the main goals of the Phoenix mission. Additionally, the lander itself may affect its landing environment. Again knowledge of how the lander may affect its surrounding is important for its own operation and environmental effect on the planet. Therefore, this research assists in investigating the effect of the Lander on the local atmospheric conditions in its landing site, especially helping to distinguish altered transport processes from original, undisturbed ones.

## 1.1 Mars

Mars is the fourth planet in the solar system between Earth and Jupiter, 80 million km away from Earth. Many attempts have been made to reach and explore Mars, starting with the Marsnik-1 in 1960 which failed. Mars exploration continued with many successful and unsuccessful missions. Among the successful missions are the Viking I&II missions, the Mars Pathfinder, the Mars Rovers (Spirit and Opportunity), the Mars Odyssey, the European Mars Express, the Mars Reconnaissance Orbiter (the latter four still operating) and the Phoenix Mars Lander, which landed on the 25th of May, 2008. The Phoenix Lander is one of NASA's scout missions. After failures with the Mars Climate Orbiter in 1998 and the Mars Polar Lander in 1999, NASA proposed a new perspective on space exploration which are cheap and safe missions to maintain constant feasible space explorations. Phoenix was chosen out of 24 proposals, mainly because it re-used some equipment of the Mars Polar Lander and the Mars Surveyor, giving it flight heritage and increasing its chances of success. Phoenix is a fixed lander and does not move, unlike the Rovers. It is equipped with a robotic arm for excavation and sample collection.

To keep the overall project cheap and safe, rather than designing a multipurpose mini-laboratory lander, Phoenix was designed to investigate the most interesting subject on Mars, i.e water. The main objective of the Phoenix Lander is studying the history of water on the planet, the present water cycle, the exchange between subsurface permafrost and the Martian soil and atmosphere. Since water is an essential element for life, more knowledge about water on Mars will provide more information on whether life existed (or exists) on the planet. Such information would also assist future residence and manned missions on the planet.

The first semi-scientific evidence of water on Mars goes back to the time when Giacomo Miraldi in 1704 observed white caps on the poles of Mars and later on suggested that they could be ice caps. After starting Mars explorations, existence of water was predicted by the pictures and data obtained by the spacecrafts sent to Mars (for example in the pioneering research work by [Kieffer et al., 1976]). Furthermore, water cycles on Mars were predicted from numerical simulations, such as the early numerical simulations of Jakosky [Jakosky et al., 1997]. Also from the pictures taken from Mars, geological evidence of great



floods, ocean beds and water channels were obtained. In June 2000, NASA announced the discovery of evidence of liquid water on Mars, confirming the previous anticipations and removing any doubt of the existence of liquid water in the Martian past. Along with the geological indications of water on Mars (surface images), various other methods and instruments are used to measure water abundance on the planet. Devices, such as the Mars Orbiter Laser Altimeter (MOLA), High Energy Neutron Detector (HEND), the Neutron Spectrometer (NS), Thermal Emission Spectrometer (TES), which measures thermal infrared energy (heat), Mars Express PFS/LW, SPICAM and OMEGA, the Gamma Ray Spectrometer (GRS), which detects gamma ray photons coming from the surface, are all used for water detection [Mellon and Jakosky, 2000, Fisher et al., 2002, Fouchet et al., 2007, Haberle et al., 2007]. Most of these devices measure the abundance of hydrogen at the surface or at the near surface atmosphere, thus relating the hydrogen abundance to a high water content. From the HEND and GRS instruments<sup>1</sup> of the Mars Odyssey, a high concentration of water is evident at the north pole with up to 70% concentration, as a percentage of soil weight [Mitrofanov et al., 2002, Boynton et al., 2002, Mitrofanov et al., 2003]. Phoenix was expected to encounter ice at a depth very close to the surface in this area.

On Mars, at the latitudes where Phoenix will land, water does not exist in its liquid form on the surface, due to the atmospheric conditions with very low temperatures and pressures making it unstable on the surface. Existence of liquid water in the regolith is also doubted. However, there are some studies that suggests liquid water transport could exist in the regolith and it is possible for liquid water to reach the surface in some special conditions [Mellon and Phillips, 2001, Haberle et al., 2001, Hecht, 2002]. Such phenomena will most likely happen near an artificial heat source and when water is not pure, e.g a solution like brine or another mixture. The whole process would also be very transient. Therefore, the existence of water, in the form of ground ice and/or ice slabs within the regolith is a greater possibility.

---

<sup>1</sup>Detected surface hydrogen.

## 1.2 Study of Water Transport on Mars

After the discovery of evidence of water on Mars, especially those suggesting recent liquid flows<sup>2</sup>, the study of water transport on this planet has been pursued with great interest. This has led to different observations and theories on the history of water on Mars, its possible cycle on the planet and the forms of its existence and transport. There have been various studies on planetary scale water transport in the atmosphere, from the regolith<sup>3</sup> to the atmosphere and the global water cycle. However, very few have studied the effects of environmental parameters on the water transport on Mars at a local scale.

The water vapour mass flux from a subterranean ice-table to the surface is governed mainly by a vapour diffusion mechanism through the regolith. The water flux is proportional to the water mass concentration gradient in the regolith and this gradient, in general, is non-linear. Different flow types and regimes on the surface influence the water vapour concentration gradient in the regolith and in the near surface atmosphere and change its profile. Therefore, one method of calculating the water vapour flux from the regolith is to have a detailed knowledge of the regolith properties and the water vapour gradient in it. For this purpose, in order to evaluate the water vapour flux to the atmosphere with a higher accuracy, the regolith and its properties should be included in a transport model.

Another method in determining water vapour mass flux to the atmosphere, is by using concentration values at a point near the surface in the atmosphere and another point at a higher elevation. This method is less reliable because the water vapour concentration at the surface is highly unstable and irregular, both spatially and temporally (as will be seen later, natural convective plumes can greatly be a source of this irregularity). Hence in this thesis, the former method, i.e. investigating the regolith to determine water vapour flux is considered.

Since the diffusion of water vapour in the soil above the ice-table is a very important process

---

<sup>2</sup>Young ( $\simeq$  one Martian year) flow channels have been observed on Mars [Malin and Edgett, 2000]. Also as mentioned before, recent studies show that water can exist on Mars in its liquid form, under certain conditions[Mellon and Phillips, 2001, Haberle et al., 2001, Hecht, 2002].

<sup>3</sup>Regolith, as referred to in this text, is defined as a layer of loose heterogeneous material covering solid rock. The Martian regolith is, in general, composed of mainly basalt material and a granular surface of basalt and montmorillonite clay [Jakosky, 1983].

in the atmospheric water vapour simulations [Jakosky et al., 1997], various numerical models have been developed on water transport through the Martian regolith. Most codes, such as the REGO-v33, solve 1-D water transport in the regolith [Fisher, 2007]. Since these models only involve the regolith, they exclude the effects of near surface atmospheric phenomena [Hecht, 2006, Painter and Grimm, 2007], or include them in a highly simplified way [Sizemore and Mellon, 2006].

Few large scale, planetary, atmospheric transport models include water transport in the regolith and for those that do, the inclusion of the regolith is limited and very primitive, when compared to the more sophisticated models that exclusively deal with the transport processes in the regolith. For example, a Mars General atmospheric Circulation Model (GCM) described by Hourdin et al. [1993] consists of 11 computational nodes in the regolith, which assumes a 1-D homogeneous soil. Or, to include the regolith effects, Wing and Austin [2006] have modelled it as a 1-D slab, with constant density, thermal diffusivity and heat capacity and the heat transfer to the soil from the atmosphere is by 1-D diffusion.

Additionally, near surface conditions are very important inputs to such general circulation models, which allow them to better predict dust and water vapour transport. Most important surface flow phenomena that affect water vapour transport are natural convection, dust devils and turbulent winds, which occur in the near surface atmosphere ( $\sim 100$  m above surface). In contrast, the GCMs cannot directly simulate (at least with current computational tools) near surface conditions, because of their inadequate resolution. For example the GCM model from Forget et al. [1999], only has 25 layers in the vertical direction from the surface, with the mid-points of the lowest three layers located at 4, 19 and 44 m above the surface and the uppermost node at 100 km. Therefore, a three dimensional model that can locally resolve the water vapour transport in a shallow regolith, including the near surface atmospheric phenomena, is required in order to improve simulations in both the regolith and the atmosphere.

The rate of diffusion in the regolith depends on near surface atmospheric conditions (e.g. temperature, pressure and surface flows) and regolith characteristics (such as porosity, permeability and tortuosity). Sears and Moore [2005] noted that many such parameters may significantly affect the evaporation rate of water on Mars, e.g. change in wind velocity,

ambient temperature and pressure. Considering the important influence of near surface atmospheric phenomena on water vapour evaporation and transport, the effects of two common phenomena, i.e. horizontal winds and natural convection are studied in this thesis. Convection and evaporation both depend on air flow. On Mars, in the case of water vapour transport, flow of thin air above a water vapour source exists most of the time, hence water evaporation is not always a diffusive process and is mostly coupled with convection (free or forced).

The importance of studying the effect of natural convection on water vapour transport is highlighted also because of the analogy of heat and mass transfer. These two types of transport are closely related and many water transport phenomena on Mars have been quantified by using the equivalent coupled heat transfer correlations, especially in the case of natural convection [Ingersoll, 1970, Hecht, 2002]. Thus more detailed study of the convection phenomena at the atmosphere-regolith interface would lead to a better estimate of water vapour evaporation and transport. Furthermore, convection will have the same effect on other trace gases, volatiles and dust<sup>4</sup>. The near surface convection on Mars is different from Earth. Therefore in this thesis, to better observe these differences, many cases are numerically modelled and simulated under Mars conditions.

To properly model water transport in the Martian regolith as realistically as possible, the Martian environment should be studied and its geological, geographical and atmospheric conditions should be considered. What we know about the planet, although extensive, is not sufficient compared to the way we know Earth and there are significant uncertainties associated with most of the information we have. However, our knowledge is sufficient to lay foundations for physical models and possibly in the future, refine the model as more accurate data becomes available.

---

<sup>4</sup>Dust is a very important factor in determining the atmospheric and surface temperatures, therefore affecting the whole Martian climate [Gierasch and Goody, 1972]. There are several major global and local dust storms during each Martian year, some of them caused by local convection [Ryan and Henry, 1979, Peterfund, 1985].

### 1.3 The Martian Regolith

One major source of water vapour flux in the Martian water cycle is from vast ice tables, which are known to exist beneath the north polar region. These ice tables are estimated to stretch for meters in depth within a few centimeters under the surface [Bandfield et al., 2008]. On top of this ice table, there is a shallow regolith, which is estimated to be 5 to 10 cm thick at the Phoenix landing site. This is the region of interest of water vapour diffusion in the regolith in the current study. This top layer, has the general characteristics of the typical Martian regolith and may contain adsorbed water, seasonal surface CO<sub>2</sub> ice and an ice-regolith compound which is different in the amount of water/ice content from place to place. Therefore, when developing mathematical models, having two distinct regions of a pure regolith and an ice table is not realistic, but this can be assumed depending on the model for regolith. Other researchers have also used similar separate soil/ice-slab assumptions, for example Fisher [2007] assumed 6 cm of “normal” dirt (defined as 1 part ice, 2 parts rock grains and 1 part void volume) on top of an ice-slab.

Fortunately, the Phoenix lander is expected to provide us with detailed information on the regolith physical properties at its landing site, e.g. grain size, rock types and quantities, pore types and crack scale. For example, it will measure relative humidity and thermal conductivity in the regolith, which are two important parameters in water vapour transport and regolith property evaluation. These parameters can be measured by Phoenix’s Thermal and Electrical Conductivity Probe (TECP). The heat capacity of the regolith at the landing site can as well be calculated from the TECP observations. The results are expected to have accuracies in the order of 10 % [Fisher, 2007].

In the current thesis, regolith properties and characteristics will be adapted for the models from various theoretical and experimental studies. Several studies have focused on determining regolith properties such as porosity, permeability, tortuosity and thermal conductivity, using a variety of theoretical, numerical and experimental techniques. These methods mainly use Fick’s law of diffusion, the Dusty Gas Model (DGM), which is the kinetic gas theory applied to porous medium [Ho and Webb, 1996], and many empirical formulas.

The Martian regolith is composed mainly of dusty basaltic material [Kieffer et al., 1976,

Sullivan et al., 2005], therefore it completely falls under the definition of porous media. From previous studies on the Martian surface and soil characteristics, a shallow layer of dust with Basalt type property is known to exist in most areas of Mars, and from thermal infrared spectrometry readings, this layer is almost entirely composed of fine grain material [Christensen, 1986a,b, Arvidson et al., 1989, Christensen et al., 1992, Crown et al., 1992]. In the north pole region, these grains are coated with ice [Sharp, 1973a,b,c],[More1996]. Further evidences of a dusty regolith on most flat surfaces are dust mantles, which are a couple of meters deep [Christensen et al., 1992] (also observed by the Pathfinder and Viking landers), or indications of soft and loose texture on the surface, e.g. the great quantity of dust transferred to the atmosphere each year [Conrath, 1975, Pollack et al., 1979, Zurek, 1982]. These dust deposits have been created during the geologic periods of Mars due to various phenomena, for example eolian processes, thermal shocks, CO<sub>2</sub> frost and water ice cycles, volcanic activities, cosmic impacts, weathering and insolation gradients. However, the Martian regolith properties vary with location, for example Tanaka and Leonard [1995], Tanaka [1997] estimated that the thermal conductivity on most of the surface matches that of a dry sand like material with medium to coarse particle size (approximately 500  $\mu\text{m}$  of mean diameter size)[Haberle, 1991, Edgett and Christensen, 1991].

Regolith physical and thermodynamical properties have been estimated in numerous studies using various techniques and approaches, and a few of them are discussed in the next sections. In most cases, knowledge of the regolith temperature is essential in obtaining regolith properties (e.g. thermal conductivity and heat capacity). Temperature throughout the regolith depends on the surface irradiation and atmospheric conditions. Maximum and minimum temperatures at the surface are around 300 K and 190 K and for the ice table, are 235 K and 200 K, respectively, which correspond to noon and midnight temperatures at the Phoenix landing site [Fisher, 2007].

In order to theoretically evaluate the porous properties of the regolith, its density is usually required and if the regolith is involved in a heat transfer model, the thermal conductivity should be known. Both these quantities are discussed in the next sections. Moreover, to model the water vapour transport from the regolith to the atmosphere, the effective diffusivity of water vapour in the atmospheric fluid for both the porous and fluid domains should be evaluated. This is discussed in 2.2.3.

## Density of the Regolith

Density of the polar regolith is estimated to be  $1.0 \pm 0.5 \text{ g cm}^{-3}$  [Malin, 1986], which includes ice,  $\text{CO}_2$  frost, dust, grains and pores. At the Viking I site, density is estimated to be  $1.15 \pm 0.15 \text{ g cm}^{-3}$  for light material and  $1.6 \pm 0.4 \text{ g cm}^{-3}$  for larger, heavier material [Moore and Jakosky, 1989]. At the Opportunity landers' site, the small fine grains beneath the surface are assumed to have a density of  $3 \text{ g cm}^{-3}$  [Jerolmack et al., 2006]. These results indicate a significant density variation due to location.

In general, the porosity of the near surface regolith is not well known. Porosities of  $54 \pm 6 \%$  and  $36 \pm 16 \%$  for silicate grain density of  $2.5 \text{ g cm}^{-3}$  correspond to the mentioned estimated densities at the Viking site [Boynton et al., 2002]. More recent experimental values can be obtained from Sizemore and Mellon [2007]. They conducted experiments with various Mars-like samples to obtain a better estimate of Mars' regolith properties. In their study, they chose Helium and Argon to diffuse through the porous media to avoid the adsorption effects. This procedure, however, fails to include the important effects of time dependent adsorption of water molecules in the regolith, which will change the regolith properties as water vapour diffuses through it. Sizemore and Mellon [2007] claimed that their measured tortuosity values were much less than other studies. For the JSC-Mars-1 sample, their reported values of porosity, tortuosity and permeability (defined in 2.2.1) are in the range of  $0.5053 < \phi < 0.5837$ ,  $1.55 < \tau < 1.88$  and  $5.47 \times 10^{-12} < K < 1.04 \times 10^{-12}$ , respectively.

## Thermal Conductivity

To select a thermal conductivity value for the regolith, it is not reasonable to assume a value for a completely basaltic material, a porous basaltic material or pure ice. Since the Martian upper regolith is a porous soil mixed with water and sometimes  $\text{CO}_2$  ice, a combination of these values contribute to the overall regolith thermal conductivity, called the effective thermal conductivity. On the other hand, it is difficult to account for all the properties of the regolith components, for example, the amount of water (all phases) in the porous regolith has a spatio-temporal variety. When water vapour density becomes greater than the saturated density value at the corresponding temperature in the pores, then the vapour

density decreases due to sublimation of ice and adsorbed water, which leads to the increase of water density in its non vapour state [Fisher, 2007]. Therefore, with assuming uniform property throughout the region of study, a single value for effective thermal conductivity, which depends on the ice and soil properties can be determined.

The effective thermal conductivity can be calculated by selecting from the soil properties and ice properties at the region of interest. As for the properties of ice in the regolith, density can be assumed  $0.92 \text{ g cm}^{-3}$  [Eisenberg and Kauzmann, 1969], which is the value for hexagonal water ice (Ih H<sub>2</sub>O) at atmospheric Earth pressure. At higher pressures, the density of ice increases so the density of Ih ice on Mars would be slightly less than  $0.92 \text{ g cm}^{-3}$ . Thermal conductivity for Ih H<sub>2</sub>O ice is approximately  $3.2 \text{ W m}^{-1} \text{ K}^{-1}$  at 200 K and  $2.4 \text{ W m}^{-1} \text{ K}^{-1}$  at 250 K at Earth atmospheric pressures [Slack, 1980]. For Ih H<sub>2</sub>O ice, thermal conductivity increases with pressure but at low pressures in the range of 0 to 0.2 GPa, this effect is negligible [Andersson and Suga, 2002].

At 223 K, Fisher et al. [2002] assumed the thermal capacity of ice to be  $C_{ice}=1741 \text{ J kg}^{-1} \text{ K}^{-1}$  and for loose dry soils  $C_{soil}=1000 \text{ J kg}^{-1} \text{ K}^{-1}$ . They assumed thermal diffusivity to be  $\alpha = 2 \times 10^{-2} \text{ cm}^2 \text{ s}^{-1}$  at 200 K for ice and icy soils and  $\alpha = 3.1 \times 10^{-3} \text{ cm}^2 \text{ s}^{-1}$  for desiccated cold soils.

One method of calculating thermal conductivity ( $k$ ), is by using thermal inertia ( $I$ ), which are related together by,

$$k = \frac{I^2}{\rho C_{reg}} \quad (1.1)$$

From TES readings from the Mars Global Surveyor, thermal inertia between 60 to 70 degree northern latitude is  $200 < I < 500 \text{ J m}^{-2} \text{ K}^{-1}$  [Mellon and Jakosky, 2000]. This range of  $I$  along with a density of  $1500 \text{ kg m}^{-3}$  and  $C_{reg}=628 \text{ J kg}^{-1} \text{ K}^{-1}$  yields thermal diffusivities in the range of  $0.04 < k < 0.27 \text{ W m}^{-1} \text{ K}^{-1}$ .

In another procedure to calculate the effective thermal conductivity, Painter and Grimm [2007] used the modified series-parallel model<sup>5</sup> [Mellon et al., 1997, Peters-Lidard et al.,

---

<sup>5</sup>With this method, soil thermal conductivity is calculated as a function of its saturation, quartz abundance, porosity, the thermodynamical state of water and the dry density of the same soil.



1998, Painter, 2003] along with a modified representation of experimental values [Peters-Lidard et al., 1998]. They assumed water in its three phases can exist in the pores of the dry regolith. Since we assume that only water ice and CO<sub>2</sub> gas can exist in the pores, the model will become,

$$k_{eff} = k_{dry} + (s_{H_2O}^2 + s_{CO_2}^2)^f (k_{sat} - k_{dry}) \quad (1.2)$$

where:

$$s_{H_2O} + s_{CO_2} = 1 \quad (1.3)$$

$$k_{sat} = k_s^{1-\phi} k_{CO_2}^{\phi s_{CO_2}} k_{H_2O}^{\phi(1-s_{CO_2})} \quad (1.4)$$

$f$  is a fitting parameter and the recommended value of 0.25 is used.  $k_{dry}$  is the dry thermal conductivity for natural soils and for terrestrial crushed rock, the following relation which is only a function of porosity can be used [Peters-Lidard et al., 1998],

$$k_{dry} = 0.039\phi^{-2.2} \quad (1.5)$$

$\phi$  is the soil porosity and  $k_s$  is the mineral grain conductivity and can be obtained from Peters-Lidard et al. [1998],

$$k_s = k_{qtz}^q k_0^{1-q} \quad (1.6)$$

$q$  is the quartz content of the dry soil.  $k_{qtz}=7.7 \text{ W m}^{-1} \text{ K}^{-1}$  is the thermal conductivity of quartz and for  $q > 0.2$ ,  $k_0=2.0 \text{ W m}^{-1} \text{ K}^{-1}$  otherwise  $k_0=3.0 \text{ W m}^{-1} \text{ K}^{-1}$ . Quartz has a very high thermal conductivity and it is a significant factor in determining the thermal conductivity of soils. In general, Basalt, which is reported to be the main component of the Martian regolith has a low quartz content. The thermal conductivity values mentioned above are calculated at ambient conditions and since thermal conductivity is inversely proportional to temperature, further correction for other temperatures should be made [Clauser and Huenges, 1995]. Due to the high uncertainty associated with other north pole regolith

properties, the temperature correction is neglected here. Assuming 50% porosity, a volume fraction of  $s_{CO_2}=0.9$  for the  $CO_2$  content in the pores and  $q=0.1$ , the effective thermal conductivity would be equal to  $k_{eff}=0.218 \text{ W m}^{-1} \text{ K}^{-1}$  at Earth ambient conditions.

There have been detailed studies on evaluating thermal conductivity at Mars like conditions [Presley and Christensen, 1997a,b,c]. They have suggested an empirical correlation which determines thermal conductivity based on pressure and the material particle size over a range of 1 to 100 torr,

$$k = C_1 P^{0.6} d^{-0.11 \log(P/C_2)} \quad (1.7)$$

$k$  has the units of  $\text{W m}^{-1} \text{ K}^{-1}$ ,  $P$  is in torr and  $d$  is the particle size in  $\mu\text{m}$ . For these units,  $C_1 \simeq 0.0015$  and  $C_2 \simeq 8.1 \times 10^4$  torr. For the JSC Mars-1 soil, which is used in many experiments to represent the Martian regolith, the particle sizes vary between  $1 \mu\text{m}$  to  $1 \text{ mm}$ . Thermal conductivity for this material at  $800 \text{ Pa}$  ( $\simeq 6$  torr) is therefore in the range of  $0.004$  to  $0.101 \text{ W m}^{-1} \text{ K}^{-1}$ . Some researchers have used this range of thermal conductivities for the regolith [Grott et al., 2007], although Mellon et al. [2004], Clifford [1993] have reported that a much higher thermal conductivity value ( $2.5 \text{ W m}^{-1} \text{ K}^{-1}$ ) due to the ice component of the ice-cemented regolith can exist<sup>6</sup>.

In another study, the thermal conductivity for ice cemented soil at  $223 \text{ K}$  is suggested to be approximately  $2.0 \pm 1.0 \text{ W m}^{-1} \text{ K}^{-1}$  [Clifford, 1993]. Therefore, thermal conductivity at the north pole regolith can approximately vary between  $0.01$  to  $2.5 \text{ W m}^{-1} \text{ K}^{-1}$  depending on particle size, pressure, temperature, porosity, dry solid material,  $CO_2$  and  $H_2O$  ice presence,  $CO_2$  gas saturation etc. The minimum value of this range is the thermal conductivity of pure  $CO_2$  gas at the ambient pressure and temperature. Painter and Grimm [2007] recommended using a permeability of  $K=3.0 \times 10^{-13} \text{ m}^2$  and a porosity of  $\phi = 0.5$  to calculate thermal conductivity values on Mars.

---

<sup>6</sup>As indicated above, water ice has a high thermal conductivity.

## 1.4 The Martian Atmosphere

The Martian atmosphere is dusty and is composed mainly of CO<sub>2</sub> (95%) [Johnson, 1965, Leighton and Murray, 1966, Leovy, 2001] with very little near surface water vapour, approximately 210 ppm on average (Less than 0.05% [Leovy, 2001]). Water vapour near the surface in the atmosphere, at the north pole on Mars, is more abundant than other locations and ice-fogs are known to exist in that region [Savijarvi, 1995]. In many studies, vapour was considered to be homogeneously distributed in the atmosphere and this simplification is also used in the present study.

Generally on the planet, the atmospheric pressure at the surface is approximately 600 Pa and the temperature on the regolith surface varies between 133 K to 300 K with an average of approximately 210 K. Temperatures of up to 280 K for a high water concentration regolith on the north pole were expected for the Phoenix landing site during summer [Kossacki et al., 2003]. Most of the northern regions on Mars consists of low elevation plains where atmospheric pressure is estimated to be in the range of 600 Pa to 1000 Pa. Using the hydrostatic pressure relation,  $\Delta P = \rho g \Delta z$ , and calculating  $\rho$  from the ideal gas law, a 100 Pa pressure difference at the surface corresponds to approximately 2 km in elevation difference. On Mars, the surface pressure range is very close to the triple point of water, which is 611.73 Pa at 273.16 K. Therefore the boiling point of water on Mars is very close to its melting point, thus at most conditions water sublimates and is transported as vapour.

Many near surface atmospheric flows such as local turbulent winds, dust devils and thermal plumes appear on Mars. Convective plumes, due to thermal buoyancy, have been observed at the Pathfinder site, with high intensities capable of lifting dust particles. Measurements from that site showed convective vortex activities that lasted tens of minutes, with the most intense ones lasting for tens of seconds [Murphy and Nelli, 2002]. In their study, Murphy and Nelli [2002] noted that from the IMP<sup>7</sup>, these convective vortices could get as large as 14 to 79 m in diameter and 46 to 350 m high. From the Viking orbiter images, vertical plumes with average surface diameter of 100 m and up to 2 km high were evident.

Since natural convection motion in the atmosphere is thermally driven, knowing the temperature at various atmospheric points, especially at the near surface (lowest 100 m) region

---

<sup>7</sup>Imager for Mars Pathfinder

is important. The Mini-TES instrument on-board Spirit and Opportunity can measure the temperature profile up to 2 km in the planetary boundary layer (PBL)[Smith et al., 2004]. PBL is defined as “the portion of the atmosphere that directly interacts with the surface, responding to forces such as frictional drag and surface heating” [Stull, 1988]. Natural convective flows are formed in the lower part of this layer. Having a thorough temperature measurement in the PBL is important to resolve the turbulent convective heat transport. Smith et al. [2004] noted that these convective and turbulent motions have a significant spatio-temporal affect on the heat, momentum and molecular transport (e.g. water vapour) from the regolith to the atmosphere. Viking and Pathfinder landers provided velocity and temperature measurements up to 2 m from the surface and the Mini-TES provided temperature readings from 20 m to 2 km above the surface [Smith et al., 2004] but none of these data are from the north pole region of Mars. In the observations from Smith et al. [2004], the typical atmospheric temperature is reported to be 220 K. The temperature in the atmosphere follows that of the surface with a several hour lag. For example at 1 m above the surface, maximum temperatures are reached approximately three hours after the surface [Smith et al., 2004]. They reported turbulent convective motions from the Mini-TES and rapid (15 to 30 s timescale), large temperature oscillations. The majority of the convective motion is observed in the superadiabatic layer within the PBL, which is the lower 200 m of the atmosphere.

With information on the temperatures in the atmosphere and the fact that most of the Martian air is composed of CO<sub>2</sub>, the required thermodynamical and transport properties of the atmosphere can be determined for the numerical model. Due to the very low temperatures and pressures in the atmosphere, it is reasonable to assume an ideal gas CO<sub>2</sub> atmosphere to determine some of the properties. The required properties are density, specific heat capacity, dynamic molecular viscosity, thermal expansivity and thermal conductivity. Density can be obtained with an ideal gas assumption,

$$\rho = \frac{MP}{\bar{R}T} \quad (1.8)$$

where  $M$  is the molar mass and  $\bar{R} = 8.3144 \text{ J mol}^{-1} \text{ K}^{-1}$  is the universal gas constant. At  $P = 800 \text{ Pa}$ ,  $T = 240 \text{ K}$  and knowing that for CO<sub>2</sub>,  $M_{CO_2} = 44.01 \text{ kg kmol}^{-1}$ , density of CO<sub>2</sub> is  $\rho_{CO_2} = 0.01764 \text{ kg m}^{-3}$ . This value is close to early atmospheric observations by the

Mariner IV, which reported a near surface density of  $0.015 \text{ kg m}^{-3}$ , although for a slightly lower temperature [Johnson, 1965].

From Yaws [1999a], specific heat capacity of  $\text{CO}_2$  at constant pressure can be calculated,

$$C_P = A + BT + CT^2 + DT^3 + ET^4 \quad (1.9)$$

The unit of  $C_P$  is  $\text{J mol}^{-1} \text{K}^{-1}$  and it is only a function of temperature. The coefficients of the equation are  $A = 27.437$ ,  $B = 4.2315 \times 10^{-2}$ ,  $C = -1.9555 \times 10^{-5}$ ,  $D = 3.9968 \times 10^{-9}$  and  $E = -2.9872 \times 10^{-13}$ . For  $\text{CO}_2$  at 240 K,  $C_P = 829.82 \text{ J kg}^{-1} \text{K}^{-1}$ . This value is close to  $860 \text{ J kg}^{-1} \text{K}^{-1}$ , which is the near surface atmospheric specific heat at constant pressure reported by Leovy [2001]. Also from Yaws [1999c], dynamic molecular viscosity of  $\text{CO}_2$  at constant low pressure can be obtained from,

$$\mu = A + BT + CT^2 \quad (1.10)$$

The unit of  $\mu$ , which is only a function of temperature, is  $\mu\text{P}$  (1 P=10 Pa s). The coefficients are  $A = 11.336$ ,  $B = 4.9918 \times 10^{-1}$  and  $C = -1.0876 \times 10^{-4}$ . Therefore for  $\text{CO}_2$  at 240 K,  $\mu_{\text{CO}_2} = 124.875 \times 10^{-7} \text{ Pa s}$ .

Thermal expansivity at constant pressure is defined as,

$$\beta = \frac{1}{V} \left( \frac{\partial V}{\partial T} \right) \quad (1.11)$$

for an ideal gas,

$$PV = nRT \implies \frac{\partial V}{\partial T} = \frac{nR}{P} \quad (1.12)$$

thus,

$$\beta = \frac{1}{T} \quad (1.13)$$

at 240 K,  $\beta = 0.004166 \text{ K}^{-1}$ .

From Yaws [1999b], thermal conductivity of CO<sub>2</sub> at constant pressure can be determined,

$$k = A + BT + CT^2 \quad (1.14)$$

The unit of  $k$  is  $\text{W m}^{-1} \text{K}^{-1}$  and is only a function of temperature. Coefficients are  $A = -0.01183$ ,  $B = 1.0174 \times 10^{-4}$  and  $C = -2.2242 \times 10^{-8}$ . for CO<sub>2</sub> at 240 K,  $k_{\text{CO}_2} = 0.01131 \text{ W m}^{-1} \text{K}^{-1}$ .

## 1.5 Surface Net Solar Irradiation at the Atmosphere-Regolith Interface

The temperature of the north polar ice cap plays a major role in determining the water sublimation flux from the regolith and atmospheric water vapour content [Richardson et al., 2002, Richardson and Wilson, 2002], and therefore should be carefully implemented in any water vapour transport model on Mars.

The surface to atmospheric temperature difference is the driving motor of the near surface and planetary natural convection motion. Surface temperatures can be determined from different General Circulation Models (GCMs) or from measurements obtained by the Mars Global Surveyor or Mars Express. For the natural convection model in this study, surface temperature cannot be prescribed directly<sup>8</sup>, therefore heat flux to the surface was estimated and used instead, which represents the net heat load from the sun. Surface temperature and hence incident heat flux to the surface can be estimated by simple surface radiation models. Smith et al. [2004] noted that surface temperature is greatly dependent on the solar irradiation (with a maximum at noon) and the atmospheric temperatures depend on both radiation and sensible heat flux.

Surface temperature on Mars depends on the irradiation from the Sun and the atmosphere, radiation from the soil to the sky, heat transfer in the regolith and in the near surface atmosphere. In this study, the surface radiative heat load is calculated as the net value of heat gain due to incident solar irradiation ( $G_s$ ) and heat loss due to surface radiation to the atmosphere ( $I_{rad}$ ). The surface long-wave radiation effects are only included as the latter term.

$$q'' = G_s - I_{rad} \quad (1.15)$$

The incident solar radiation from the Sun to the Martian atmosphere is itself, in general, affected by parameters such as CO<sub>2</sub> density, CO<sub>2</sub> frost, dust, water vapour and ice particles.

---

<sup>8</sup>This is due to the fact that the regolith and the atmosphere use a fluid-porous interface at their connecting surfaces, which has a conservative heat flux implied to it. This will be further discussed in the numerical modelling chapter.

These obstructions to the path of the solar radiation reduce its intensity, creating an optical depth through the atmosphere. Optical depth,  $\tau_o$ , is an indicator of transparency and is defined as a fraction of radiation that is lost from an original beam. If  $I_a$  and  $I_s$  are the direct solar irradiation at the top of the atmosphere and on the surface respectively, then Beer's law implies that,

$$\frac{I_s}{I_a} = e^{-m_a \tau_o} \quad (1.16)$$

Where  $m_a$  is the air mass adjusting factor dependent on the zenith angle of the incident solar radiation [Appelbaum et al., 1993].

In order to calculate the direct solar irradiation at the Martian north pole surface, the solar irradiation at the top of the atmosphere must be calculated first,

$$I_a = 590 \frac{[1 + e_M \times \cos(L_s - 248^\circ)]^2}{(1 - e_M^2)^2} \quad (1.17)$$

Where  $e_M$  is Mars' orbit eccentricity and is  $e_M = 0.093377$ . In this relation,  $590 \text{ W m}^{-2}$  is the Solar constant or the mean beam irradiation from the sun and  $L_s$  is the aerocentric longitude at the solar noon (calculated in the appendix of [Badescu, 1998]). Thus the direct solar irradiation to a horizontal plane on the Martian surface can be calculated as,

$$I_s = I_a \exp\left(-\frac{\tau_o}{\cos\theta_z}\right) \cos\theta_z \quad (1.18)$$

where  $\theta_z$  is the zenith angle of the Sun. The maximum incident  $I_s$  can also be determined roughly by [Hecht, 2002],

$$I_s = (1 - a) 590 \exp\left(-\frac{\tau_o}{\cos\theta_z}\right) \quad (1.19)$$

Where  $a$  is the albedo. Furthermore, the global solar irradiation on a horizontal surface,  $G_s$ , which is the sum of the direct solar irradiation (irradiation directly from the sun on a horizontal surface) and the diffuse irradiation is determined by [Appelbaum et al., 1993],

$$G_s = I_a \cos\theta_z \frac{f(\theta_z, \tau_o, a)}{1 - a} \quad (1.20)$$

$f(\theta_z, \tau_o, a)$  can be obtained from the same reference. Diffuse irradiation originates from atmospheric scattering.



It should be noted that the above relations assume radiation from a high emissivity surface that is nearly flat and the solar insolation is absorbed at a thin layer at the regolith surface. In order to properly calculate the surface irradiation, optical information about the regolith and the atmosphere is needed. Albedo and optical depth for a clear sky are typically assumed 0.25 and 0.1 respectively. For the north pole surface, Fisher [2007] has assumed 0.25 albedo and 0.95 emissivity. Using the same value for emissivity (0.95), Hecht [2002] claimed that on Mars,  $a$  is typically between 0.1 to 0.35 and  $\tau_o$  is between 0.1 to 1.0. In their paper, Appelbaum et al. [1993] have provided an extensive table of albedo for the entire range of latitudes and longitudes, obtained from Pollack et al. [1990]. From this table for the northern plains, for latitudes between  $65^\circ$  and  $90^\circ$ , the surface albedo is  $0.2 \lesssim a \lesssim 0.4$ . More specifically since the Phoenix Mars Lander is planned to land at approximately  $68^\circ\text{N}$  and  $234^\circ\text{E}$ , the corresponding albedo for this region is approximately 0.23. During the Phoenix's primary mission, the areocentric longitude of the Sun starts at  $L_s=77^\circ$  and ends 90 sols<sup>9</sup> later at  $L_s=118^\circ$ . From Eqn. 1.17, for this range of  $L_s$ ,  $I_a$  is between 495 to 530  $\text{W m}^{-2}$ . The solar zenith angle can be calculated by,

$$\cos(\theta_z) = \sin(\phi_l)\sin(\delta) + \cos(\phi_l)\cos(\delta)\cos(\omega_h) \quad (1.21)$$

where  $\phi_l$  is the latitude and  $\omega_h$  is the hour angle measured from noon, therefore at noon,  $\omega_h=0$ .  $\delta$  is the declination angle defined by,

$$\sin(\delta) = \sin(\delta_0)\sin(L_s) \quad (1.22)$$

where  $\delta_0=24.936^\circ$  is the Mars obliquity of rotation axis. Using the above equations and considering the  $L_s$  range for Phoenix and that maximum temperature at the surface are observed at noon [Smith et al., 2004], the solar zenith angle is between  $44.05^\circ$  and  $46.45^\circ$ . Since the change in the solar zenith angle is not significant for the application of this study, a constant value of  $45^\circ$  is selected for it during the Phoenix Lander mission.

With the above information and by determining  $f(\theta_z, \tau_o, a)$ , the noon-time global solar irradiation at a horizontal surface at the Phoenix landing site can now be obtained. For three albedo values, three optical depth values and the starting and ending  $L_s$  for the primary mission of Phoenix,  $G_s$  is calculated and provided in Table. 1.1,

---

<sup>9</sup>A Martian sol is a Martian day, equal to 24.66 Earth hours.

Optical depth ( $\tau$ )	Albedo, $a$					
	0.1		0.23		0.4	
	$L_s$		$L_s$		$L_s$	
	77°	118°	77°	118°	77°	118°
0.1	339	363	340	364	342	366
0.5	297	318	301	322	307	328
1.0	252	270	258	276	266	285

Table 1.1:  $G_s$ ( $\text{W m}^{-2}$ ) for different albedo and optical depths at the starting and ending  $L_s$  of the Phoenix mission. As mentioned previously, these values for  $\tau_o$  and  $a$  (especially  $a=0.23$ ) have been used in literature to represent the values at the Lander's site.

As mentioned previously, the heat load at the surface ( $q''$ ) on Mars is the balance of the direct global solar irradiation and the net surface to sky (long-wave) radiation, which in a simple form can be calculated as,

$$I_{rad} = \varepsilon\sigma (T_{sur}^4 - T_{sky}^4) \quad (1.23)$$

where  $\varepsilon$  is the emissivity and  $\sigma = 5.7 \times 10^{-8} \text{ W m}^{-2} \text{ K}^{-4}$  is the Stefan-Boltzmann constant and the  $T_{sky}$  is assumed to be 100 K. For example for  $\varepsilon=0.95$ ,  $T_{sky}=100$  K ([Morey and Gorman, 1976]) and  $T_{sur}=250$  K,  $I_{rad}=206 \text{ W m}^{-2}$ . This value can significantly decrease when the sky is not clear (higher  $T_{sky}$ ) and a lower emissivity. Also, the surface radiation to the sky obtained from the above relation assumes radiation to a  $2\pi$  solid angle of the sky. Depending on the surface geometry the apparent (real) emissivity can be as low as half the original value [Hecht, 2002]. Nevertheless, since the regolith surface radiation to the sky is significant, a value of at least  $50 \text{ W m}^{-2}$  lower than that of table 1.1 should be used to obtain  $q''$ .

# Chapter 2

## Theory

### 2.1 Modelling Atmospheric Flows on Mars

The atmospheric flows modelled in this study are near surface winds and natural convection. These two surface flows often appear together. Surface winds are in this case, part of a surface atmospheric flow within the planetary boundary layer, created by natural convection. Thus studying wind and natural convection in a local domain provides a better near surface flow simulation at a landing site.

#### 2.1.1 Winds

Local, near surface winds on Mars, can be mathematically modelled with a mass conservation and the Navier-Stokes equation for a Newtonian, incompressible atmospheric fluid. Since the near surface wind velocities on Mars are low, the incompressible fluid assumption is valid. To prove this, if the Mach number ( $M$ ) is less than 0.3, the gas flow can be assumed incompressible.  $M$  is defined as,

$$M \equiv \frac{V}{c} \tag{2.1}$$

where  $V$  is the gas velocity and  $c$  is the local speed of sound. For an ideal gas,  $c$  can be calculated with,

$$c_{ideal} = \sqrt{\frac{\gamma \bar{R} T}{M}} \quad (2.2)$$

where  $\gamma$  is the adiabatic index of the gas and  $\bar{R}$  is the universal gas constant. Assuming an ideal gas, CO<sub>2</sub> atmosphere and knowing that for CO<sub>2</sub>,  $\gamma=1.29$  [Zharkova et al., 1976] and  $M_{CO_2}=44.01 \text{ g mol}^{-1}$  then at  $T=253 \text{ K}$ ,  $c_{CO_2}=248.3 \text{ m s}^{-1}$ .

So, for a  $50 \text{ m s}^{-1}$  wind,  $M=0.2$  which is less than 0.3.

The general mass conservation equation can be written as,

$$\frac{\partial \rho}{\partial t} + \partial_i (\rho u_i) = 0 \quad (2.3)$$

and in vector notation,

$$\frac{\partial \rho}{\partial t} + \nabla \cdot (\rho \vec{U}) = 0 \quad (2.4)$$

which for an incompressible flow becomes,

$$\nabla \cdot \vec{U} = 0 \quad (2.5)$$

As for the transport of momentum, based on the wind velocity and the anticipated turbulence levels near the surface, flows can be modelled as laminar or by employing turbulence models.

## Laminar Winds

The full Navier-Stokes equation can be written as,

$$\rho \frac{Dv_i}{Dt} = \partial_j \sigma_{ij} + S_i \quad (2.6)$$

where  $\sigma_{ij}$  is the stress tensor and  $S_i$  is the momentum source and includes body forces ( $B_i$ ).

In vector notation, the Navier-Stokes equation can be expanded as,

$$\rho \left[ \frac{\partial \vec{U}}{\partial t} + \nabla \cdot (\vec{U} \otimes \vec{U}) \right] = -\nabla P + \nabla \cdot \Psi + \vec{S}_0 \quad (2.7)$$

( $\otimes$  is the Diadic operator (tensor product) of two vectors.)

where  $\Psi$  is the viscous stress tensor, neglecting the dilational viscosity.

$$\Psi = \mu \left[ (\nabla \vec{U}) + (\nabla \vec{U})^T - \frac{2}{3} \delta \nabla \cdot \vec{U} \right] \quad (2.8)$$

For incompressible flow,

$$\rho \left[ \frac{\partial \vec{U}}{\partial t} + (\vec{U} \cdot \nabla) \vec{U} \right] = -\nabla P + \mu \nabla^2 \vec{U} + \vec{S}_0 \quad (2.9)$$

where in the case of near surface winds, the only source associated with  $\vec{S}_0$  is Mars' gravity force, therefore,

$$\rho \left[ \frac{\partial \vec{U}}{\partial t} + (\vec{U} \cdot \nabla) \vec{U} \right] = -\nabla P + \mu \nabla^2 \vec{U} + \rho \overrightarrow{g_{Mars}} \quad (2.10)$$

## Turbulent Winds

Turbulence in the near surface atmosphere can be numerically simulated (approximately) with many mathematical models. In order to model turbulent winds in this study, the k- $\epsilon$  model, which is an eddy viscosity turbulence model, is applied. This model is used because the geometry of the problem is fairly simple and the flow does not involve complexities which the model cannot resolve, such as when stress-strain or the orientation of the turbulence structure in the flow are important. Furthermore, the k- $\epsilon$  model is widely used in industry and in studies where precise resolving of turbulence is not required, which is also the case in this study. Another advantage of the eddy viscosity models, including the k- $\epsilon$  model, is that generally much lower computational resources are required compared to the Direct Numerical Simulation (DNS), Large Eddy Simulation (LES) and Reynolds Stress Model (RSM) models. The k- $\epsilon$  model is also numerically robust and has shown very good agreements with experimental results for 2-D flows with attached boundary layers and

many internal flows. For the k- $\epsilon$  model, the fluid velocity, which appears in the transport equations, is:

$$\vec{U} = \vec{U}_m + \vec{u}' \quad (2.11)$$

where  $\vec{U}_m$  is the time averaged component and  $\vec{u}'$  is the fluctuating component of the velocity, respectively. After averaging the momentum equations (Reynolds Averaged Navier-Stokes, RANS), they become,

$$\rho \left[ \frac{\partial \vec{U}_m}{\partial t} + \nabla \cdot (\vec{U}_m \otimes \vec{U}_m) \right] = -\nabla P' + \nabla \cdot \left( \mu_{eff} \left( \nabla \vec{U}_m + (\nabla \vec{U}_m)^T \right) \right) + \vec{S}_0 \quad (2.12)$$

where

$$\mu_{eff} = \mu + \mu_t \quad (2.13)$$

$\mu_t$  is the turbulent viscosity, which in the k- $\epsilon$  model is defined as,

$$\mu_t = \frac{C_\mu \rho k^2}{\epsilon} \quad (2.14)$$

$C_\mu$  is a constant equal to 0.09 and  $P'$  is the modified pressure, which for incompressible flows is defined as,

$$P' = P + \frac{2\rho k}{3} \quad (2.15)$$

$k$  is the turbulence kinetic energy and  $\epsilon$  is the turbulence kinetic energy dissipation rate, which are solved for with two additional transport equations,

$$\frac{\partial \rho k}{\partial t} + \nabla \cdot (\rho \vec{U} k) = \nabla \cdot \left( \left( \mu + \frac{\mu_t}{\sigma_k} \right) \nabla k \right) + P_k - \rho \epsilon \quad (2.16)$$

$$\frac{\partial \rho \epsilon}{\partial t} + \nabla \cdot (\rho \vec{U} \epsilon) = \nabla \cdot \left( \left( \mu + \frac{\mu_t}{\sigma_\epsilon} \right) \nabla \epsilon \right) + \frac{\epsilon}{k} (C_{\epsilon 1} P_k - C_{\epsilon 2} \rho \epsilon) \quad (2.17)$$

where  $C_{\epsilon 1}$ ,  $C_{\epsilon 2}$ ,  $\sigma_k$  and  $\sigma_\epsilon$  are constants equal to 1.44, 1.92, 1.0 and 1.3, respectively [Wilcox, 1993].  $P_k$  is the turbulence production term and for an incompressible flow can be written as,

$$P_k = \mu_t \nabla \vec{U} \cdot (\nabla \vec{U} + \nabla \vec{U}^T) - P_{kb} \quad (2.18)$$

and  $P_{kb}$  is the buoyancy production term, described in 2.3.3.

## 2.1.2 Natural Convection

Natural convection<sup>1</sup>, along with forced convection is a form of convective transport of heat, mass or any other generic transport entity. Natural convection is caused by density gradients in a fluid. That is, in the presence of a body force and density gradients in a fluid, convective motion may be created due to the buoyancy forces. Density gradients can be created by temperature and/or concentration gradients in a fluid. As an example for such motion, the fluid motion between two horizontal plates with different temperatures can be mentioned. If the bottom plate is hot and the top plate is cold, the heat at the bottom warms up the lower fluid, thus decreasing its local density. In presence of a gravitational body force that is downwards, the lower density fluid at the bottom tends to “move up” due to buoyancy forces. The upper cold fluid with higher density now replaces the warmer bottom fluid due to its weight being heavier, thus creating a circulation pattern in the configuration. It should be mentioned that the temperature difference should exceed a critical value, so that the buoyancy forces overcome the opposing viscous forces, otherwise no motion will be created. On the other hand, if the top plate is hot and the bottom plate is cold, the heavier cold fluid remains at the bottom and the warmer fluid remains at the upper levels creating a stable, quiescent, thermally stratified configuration.

---

<sup>1</sup>Sometimes called free convection as well, although this latter term is used more often for external buoyancy driven flows. Gebhart et al. [1988] suggests that the term buoyancy-induced flows better suits this phenomena.

In a thermodynamical perspective, the entire convective circulation can be interpreted as a heat engine. In this heat engine, the fluid is expanded by the heat reservoir and compressed by the cold reservoir creating the fluid circulation that is the work of the theoretical engine [Bejan, 1995].

The natural convective motion may have a structured form, for example the parallel plates configuration with convective rolls in between called the Rayleigh-Benard convection, or a completely chaotic structure, for example in the case of a hot plate in a cold fluid, that creates thermal plumes or buoyant jets. Nonetheless, in all cases, a motion is created that can transport heat and mass in a fluid.

Natural convection, as a transport mechanism, is very interesting due to its frequent occurrence in nature and industry. From the meso-scale and global scale convection in the atmosphere, oceans and the mantle of a planet to micro heat pipes in electronic devices, natural convection can exist in any fluid medium. In industry, the natural convective heat transfer options are sought for in many applications due to their relatively lower costs compared to forced convective motion.

Mathematically, in the case of pure natural convection, the buoyancy force arises due to the difference in the hydrostatic pressure gradient ( $\nabla p$ ), which is proportional to the local density<sup>2</sup> in a fluid ( $\nabla p = -\rho \vec{g}$ ), that is,  $\vec{B} = -\vec{g} (\rho - \rho_0)$ , where  $\rho_0$  is a reference density in the bulk fluid. Therefore, the difference between buoyancy driven flows and other flow types is that the term  $\vec{g} (\rho - \rho_0)$  is the dominant driving force of the flow.

In the case of an ideal gas, using  $\rho = \frac{P_0}{RT}$  and  $\rho_0 = \frac{P_0}{RT_0}$ ,

$$\frac{\rho_0 - \rho}{\rho} = \frac{T - T_0}{T_0} \implies \rho = \rho_0 - \rho \left( \frac{T}{T_0} - 1 \right) \quad (2.19)$$

$$\text{and if } \left( \frac{T - T_0}{T_0} \right) \ll 1 \quad (2.20)$$

using Eqn.2.19, it could be assumed that  $\rho \simeq \rho_0$

$$\rho \simeq \rho_0 \left[ 1 - \frac{1}{T_0} (T - T_0) \right] \quad (2.21)$$

---

<sup>2</sup>Generally speaking, proportional to the body force.



It was shown previously that for an ideal gas, the thermal expansivity is  $\beta = \frac{1}{T}$ , therefore,

$$\rho \simeq \rho_0 [1 - \beta (T - T_0)] \quad (2.22)$$

This approximation for the buoyancy term in the transport equations is also known as the Boussinesq approximation, based on the assumption that  $\beta (T - T_0)$  is significantly smaller than unity.

Using the Boussinesq assumption in the Navier-Stokes equation for incompressible flow,

$$\rho \left[ \frac{\partial \vec{U}}{\partial t} + (\vec{U} \cdot \nabla) \vec{U} \right] = \mu \nabla^2 \vec{U} + \rho \beta (T - T_0) \vec{g} \quad (2.23)$$

Since thermal buoyancy driven flows involve the transport of heat, an extra transport equation for it should be solved along with the mass and momentum equations.

The heat equation is solved as the total energy equation. Neglecting the work due to external momentum and viscous stress, it can be written as,

$$\frac{\partial (\rho h_t)}{\partial t} - \frac{\partial P}{\partial t} + \nabla \cdot (\rho \vec{U} h_t) = \nabla \cdot (\alpha \nabla T) + S_e \quad (2.24)$$

where  $\alpha$  is the thermal diffusivity and  $h_t$  is the total specific enthalpy defined with relation to static specific enthalpy as,

$$h_t = h_s + \frac{1}{2} \vec{U}^2 \quad (2.25)$$

From scale or similarity analysis, two non-dimensional groups pertinent to a natural convection flow are obtained, which for the momentum equation is the Grashof (Gr) number and for the heat equation, are the Grashof (Gr) and the Prandtl (Pr) numbers. The Prandtl number can be interpreted as the ratio of the momentum diffusivity to thermal diffusivity<sup>3</sup>. The Grashof number can be interpreted as the ratio of the buoyancy forces to the viscous forces and is defined as,

---

<sup>3</sup>It can be also used as the rate of momentum transfer to the rate of heat transfer, the velocity boundary layer thickness to the thermal boundary layer thickness or the ratio of viscous forces to thermal diffusivity.

$$\text{Gr}_H = \frac{g\beta(T_s - T_0)H^3}{\nu^2} \quad (2.26)$$

Where  $H$  is the domain height scale and  $\nu$  is the kinematic viscosity. Since the  $\text{Gr}_H^{\frac{1}{2}}$  appears in the non-dimensional momentum equation, it can be interpreted as being equivalent to the Reynolds number in other non-buoyant flows.

In the heat equation, the Gr and the Pr number appear together. For convenience, the Rayleigh number is defined as  $\text{Ra}_H = \text{Gr}_H \cdot \text{Pr}$ , in other words, since  $\text{Pr} = C_p \mu / k$ ,

$$\text{Ra}_H = \frac{g\beta\rho^2 C_p (T_s - T_0) H^3}{k\mu} \quad (2.27)$$

where  $k$  is the thermal conductivity of the fluid. Due to the appearance of the Ra in the heat equation, it is expected that the Nusselt number (Nu) would somehow depend on it. From similarity analysis, it can be shown that for high Pr numbers ( $\text{Pr} \gg 1$ ),  $\text{Nu} \sim \text{Ra}_H^{\frac{1}{4}}$  and for low Pr numbers ( $\text{Pr} \ll 1$ ),  $\text{Nu} \sim (\text{Ra}_H \text{Pr})^{\frac{1}{4}}$  [Bejan, 1995]. In order to determine the heat transfer coefficient in applications, based on the dependence of Nu on Ra and Pr, there are numerous correlations suggested for various configurations and situations of thermal buoyancy driven flows.

## Natural Convection on Mars

On Mars, due to the rapid rise of temperature at the surface by solar irradiation, a significant temperature gradient between the surface and the atmosphere is developed, resulting in the appearance of thermal buoyancy forces in the near surface atmosphere. To study the natural convection mechanism in the near surface atmosphere, the fluid properties and the non-dimensional numbers pertinent to the case should be evaluated. The non-dimensional numbers can be calculated using the atmospheric fluid properties stated in section 1.5. For the near surface atmosphere at 240 K and 800 Pa,  $\text{Pr} = 0.92$ . This value is slightly lower than one, so the thermal boundary layer is expected to be slightly smaller than the velocity boundary layer.

## Turbulence Models for Buoyancy Driven Flows

If the convection flow regime on Mars is transitional or turbulent, a turbulent model may be used, however, it is not known which turbulence model would better resolve the convective motion. On the other hand, a laminar assumption may be sufficient to model this flow with no need for computationally expensive turbulence models. The suitability of the laminar assumption versus turbulence models for buoyancy driven flows are determined by comparing them with experimental data, discussed in 3.3.3.

Since the  $k$ - $\epsilon$  model is not suitable for buoyancy driven flows, other more sophisticated turbulence models may be required. One model, which has successfully been applied to some buoyancy driven flows, is the  $k$ - $\omega$  model. This model is an eddy viscosity turbulence model, which instead of solving an equation for the turbulence dissipation rate ( $\epsilon$ ), solves for the turbulence frequency ( $\omega$ ). The  $k$ - $\omega$  model allows a special near wall region treatment for low Reynolds number computations. Other advantages of this model are that it is more accurate than the  $k$ - $\epsilon$  model, it has a high degree of robustness and it is still computationally feasible. For the  $k$ - $\omega$  model the turbulence viscosity is determined as,

$$\mu_t = \frac{\rho k}{\omega} \quad (2.28)$$

and the  $k$  and  $\omega$  transport equations are,

$$\frac{\partial \rho k}{\partial t} + \nabla \cdot (\rho \vec{U} k) = \nabla \cdot \left( \left( \mu + \frac{\mu_t}{\sigma_k} \right) \nabla k \right) + P_k - \beta' \rho k \omega \quad (2.29)$$

$$\frac{\partial \rho \omega}{\partial t} + \nabla \cdot (\rho \vec{U} \omega) = \nabla \cdot \left( \left( \mu + \frac{\mu_t}{\sigma_\omega} \right) \nabla \omega \right) + \frac{\alpha \omega P_k}{k} - \beta \rho \omega^2 \quad (2.30)$$

The equation constants  $\beta'$ ,  $\beta$ ,  $\alpha$ ,  $\sigma_k$  and  $\sigma_\omega$  are 0.09, 0.075, 5/9, 2 and 2 respectively.

If the Boussinesq approximation is used, for both the  $k$ - $\omega$  and the  $k$ - $\epsilon$  models, the buoyancy production term ( $P_{kb}$ ) in the turbulence production term ( $P_k$ ) is,

$$P_{kb} = \frac{\mu_t \beta}{\sigma_\rho} \vec{g} \cdot \nabla T \quad (2.31)$$

and the constant  $\sigma_\rho$  is equal to 0.9. The implementation of this buoyancy production term is discussed in section 2.3.3.

## 2.2 Modelling Water Vapour Transport in the Martian Regolith

The Martian atmosphere is mainly composed of  $\text{CO}_2$ . Since the water vapour amount in the atmosphere and the regolith is very little, it can be modelled as a trace gas transport in a fluid with porous effects present in the regolith. For low regolith depths, a constant average pressure can be assumed and for the typical conditions at the northern plains on Mars, water exists in its solid or vapour state, although there have been recent suggestions that water can exist in its liquid form [Hecht, 2002]. Therefore, water vapour transport can be modelled as a trace gas transport in a  $\text{CO}_2$  abundant regolith.

In the regolith above the ice-table, it is reasonable to assume semi saturated pores, where water ice can be assumed to be in equilibrium with water vapour and hence only one equation for water transport is required [Painter and Grimm, 2007]. The extra transport equation for any additional species, such as water vapour, can be written in vector notation as,

$$\frac{\partial(\rho\varphi)}{\partial t} + \nabla \cdot (\rho \vec{U} \varphi) = \nabla \cdot (\rho D_\varphi \nabla \varphi) + S_\varphi \quad (2.32)$$

where  $\varphi$  is the conserved quantity per unit mass and  $\Phi = \rho\varphi$  is the conserved quantity per unit volume, which in the case of this study are the water vapour concentration and density, respectively.  $D_\varphi$  is the diffusivity of  $\varphi$  in the main fluid and  $S_\varphi$  is the volumetric source term. In this study, water vapour is the additional species that is transported in the main fluid, therefore assuming incompressibility, the additional transport equation for water vapour can be written as,

$$\rho \left[ \frac{\partial \omega_w}{\partial t} + \vec{U} \nabla \omega_w \right] = \nabla \cdot (\rho D_{wc} \nabla \omega_w) + S_w \quad (2.33)$$

where  $\omega_w = \rho_w/\rho$  is the mass fraction of water vapour and  $D_{wc}$  is its diffusivity in the main fluid, thus,

$$\frac{\partial \rho_w}{\partial t} + \nabla \cdot (\rho_w \vec{U}) = \nabla \cdot \left[ \rho D_{wc} \nabla \left( \frac{\rho_w}{\rho} \right) \right] + S_w \quad (2.34)$$

### 2.2.1 Porous Media

Porous media such as terrestrial soils, sand, foams, textile and bio-materials are solids with an internal network of very small pores (void spaces) for an arbitrary volume. Such materials cause obstruction (resistance) to the flow of fluids that are permeating them. Since modelling the transport phenomena in the entire, often complex pore structure and micro-channels of a porous medium is extremely difficult (if not impossible) and resource exhausting at a micro-scale, various macroscopic models have been developed to account for the obstruction effect of the porous media. The most simple, yet fundamental model is the empirical Darcy's law of flow in a porous medium. Darcy's law relates the fluid flux ( $V$ , [L T<sup>-1</sup>]) through a porous medium under a hydraulic pressure gradient as,

$$\vec{V} = \frac{-K\nabla P}{\mu} \quad (2.35)$$

where  $K$  [m<sup>2</sup>] is the permeability of the porous medium. Porous media have unique properties, and the obstruction effect in the porous medium models can be implemented by using them. Porosity, tortuosity and permeability are porous media properties that characterize a porous material.

Porosity ( $\phi$ , volume porosity) is the void fraction of a sample volume of a porous medium. It represents the volume fraction in a porous medium that is open to flow. Tortuosity ( $\tau$ ) can be defined as the ratio of the length of a porous sample to the actual path length that should be passed to reach the end of the sample in the pore structure. And finally permeability ( $K$ , [L<sup>2</sup>]) is a measure of the resistance of a porous medium to a fluid flow and can be defined as [Bear, 1972],

$$K = C d_p^2 \quad (2.36)$$

where  $C$  is a non-dimensional constant that depends on the porosity and microscopic geometry of the porous medium and  $d_p$  is the effective pore size. Permeability can also be obtained experimentally by using Darcy's law.

In this study, a simple porous medium model, sometimes known as the Directional Loss Model, is employed which is widely used in practical applications and which is easy to implement in numerical codes. In this model, proposed by Joseph et al. [1982], the transport equations are generalized with the Darcy's law and a special treatment is used for the source term in the momentum equation. In this case, for a Newtonian, incompressible flow,

$$\rho \left( \frac{\partial v_i}{\partial t} + v_j \partial_j v_i \right) = -\partial_i P + \mu \partial_j^2 v_i + B_i + R_i^p \quad (2.37)$$

where  $B_i$  is the body force and  $R_i^p$  is the porous momentum resistance to the flow defined as,

$$R_i^p = -C^{R1} v_i - C^{R2} |v_i| v_i \quad (2.38)$$

where  $C^{R1}$  is the linear resistance coefficient defined as,

$$C^{R1} = \frac{\mu}{K} \quad (2.39)$$

and  $C^{R2}$  is the quadratic resistance coefficient defined as,

$$C^{R2} = \rho K_{loss} \quad (2.40)$$

and  $K_{loss}$  is an empirical loss coefficient. The velocity used in Eqn. 2.37 ( $v_i$ ) is the averaged superficial velocity used in Darcy's law ( $V$ ) and is related to the true velocity by,

$$v_j = \Lambda_{kj} u_k \quad (2.41)$$

where  $\Lambda_{kj}$  is the area porosity tensor. In terms of the true velocity, Eqn. 2.37 becomes [Kaviany, 1995, Kleinstreuer, 2003],

$$\rho \left( \frac{\partial \phi u_i}{\partial t} + \partial_j \Lambda_{jk} u_k u_i \right) = -\phi \partial_i P + \mu \partial_j \Lambda_{jk} (\partial_k u_i + \partial_i u_k) + \phi B_i + \phi R_i^p \quad (2.42)$$

and the resistance coefficients become,

$$C^{R1} = \frac{\mu}{\phi K} \quad (2.43)$$

$$C^{R2} = \frac{\rho K_{loss}}{\phi^2} \quad (2.44)$$

If the volume porosity is constant and the area porosity is isotropic throughout the porous medium,  $\Lambda_{ij} = \phi \delta_{ij}$  [Dmitriev, 1995] and for very low velocities, the second term in Eqn. 2.38 can be neglected, resulting in,

$$\rho \phi \left( \frac{\partial u_i}{\partial t} + u_j \partial_j u_i \right) = -\phi \partial_i P + \mu \phi \partial_j^2 u_i + \phi B_i - \frac{\mu u_i}{K} \quad (2.45)$$

This equation is the momentum transport equation used in this study, which is valid in the regolith, and in a fluid,  $\phi=1$  and  $K=\infty$ . Similarly, for the heat and the water vapour transport equations in a porous medium,  $h_t$  and  $\rho_w$  replace the generic quantity  $\varphi$  in the generic transport equation in a porous medium respectively,

$$\rho \phi \left( \frac{\partial \varphi}{\partial t} + u_j \partial_j \varphi \right) = \phi \partial_j (\Gamma_\varphi \partial_j \varphi) + \phi S_\varphi \quad (2.46)$$

where  $\Gamma_\varphi$  is the diffusivity of  $\varphi$  and  $S_\varphi$  is the source term for the generic quantity which in porous medium is,

$$S_\varphi = \frac{\mu \varphi}{\phi K} + S_0 \quad (2.47)$$

and  $S_0$  are other source terms.

## 2.2.2 Water Vapour Diffusion in CO<sub>2</sub>

In general, mass diffusion can be calculated by (Landau 1987, chapter 57 and 58),

$$J_{Diff} = -\rho_0 \left( D_{12} \frac{\partial \left( \frac{\rho_1}{\rho_0} \right)}{\partial z} + \frac{D_T}{T} \frac{\partial T}{\partial z} + \frac{D_p}{P_0} \frac{\partial P_0}{\partial z} \right) \quad (2.48)$$



where  $D_T$  and  $D_p$  are the mass transfer thermal diffusion and pressure diffusion coefficients, respectively. In cases of constant pressure and temperature, the above formulation results in the simple Fickian diffusion formula. In our case, since the pressure is constant through the regolith domain, advection diffusion effects are negligible and are not considered. Since pressure gradients in the shallow regolith region above the ice table are very small, the pressure diffusion effect can be safely omitted. Although temperature gradients can be expected within the poorly conducting regolith layer, due to the limitations in the modelling software, the thermal diffusion effects are also neglected. It should be mentioned that adsorption could also be significant depending on the timescale of the process, but is neglected in this study.

Many theoretical relationships have been proposed to calculate the binary gas diffusion coefficient, which are mostly based on the Chapman-Enskog theory [Chapman and Cowling, 1970, Gilliland et al., 1974, Mason and Malinauskas, 1983, Reid et al., 1987, Holman, 1997]. There have been several experimental measurements of water vapour diffusion into pure gases such as CO<sub>2</sub>. From the international critical tables, Washburn [2003], citing the work of Guglielmo [1882], Winkelmann [1889] conducted at atmospheric pressures and a temperature range of 291 to 373 K, the following correlation is suggested:

$$D_{wc} = 0.1387 \left( \frac{T}{T_0} \right)^2 \left( \frac{P_0}{P} \right) \quad (2.49)$$

From the work of Marrero and Mason [1972] in the temperature range of 296 to 1649 K, the following correlation is suggested:

$$D_{wc} = 9.24 \times 10^{-5} T^{\frac{3}{2}} e^{\frac{-307.9}{T}} \left( \frac{P_0}{P} \right) \quad (2.50)$$

Wallace and Sagan [1979] recommended using the following correlation:

$$D_{wc} = 0.1654 \left( \frac{T}{T_0} \right)^{\frac{3}{2}} \left( \frac{P_0}{P} \right) \quad (2.51)$$

where the coefficient unit is cm<sup>2</sup> s<sup>-1</sup>,  $P_0=1013$  mbar and  $T_0 = 273.15$  K. When comparing to diffusion in Earth's atmosphere, the correlation from Marrero and Mason [1972] can be used, which is recommended in the temperature range of 282 to 373 K,

$$D_{wc} = 1.87 \times 10^{-6} T^{2.072} \left( \frac{P_0}{P} \right) \quad (2.52)$$

The binary diffusion coefficient of water into CO<sub>2</sub> can also be obtained from Washburn [2003],

$$D_{wc} = D_0 \left( \frac{T}{T_0} \right)^m \frac{P_0}{P} \quad (2.53)$$

where  $D_0 = 0.1387 \text{ cm}^2 \text{ s}^{-1}$ ,  $T_0 = 273 \text{ K}$ ,  $P_0 = 1 \text{ atm}$  and  $m = 2.0$ . For  $T = 230 \text{ K}$  and  $P = 700 \text{ Pa}$ , Eqn. 2.53 yields  $D_{wc} = 14.25 \times 10^{-4} \text{ m}^2 \text{ s}^{-1}$ .

### Water Vapour Diffusion in the Martian Atmosphere

In this study, for Mars, Eqn. 2.51 is used, because other relationships are recommended for a higher temperature range than typical values on Mars. Therefore at  $T = 240 \text{ K}$  and  $P = 800 \text{ Pa}$ ,  $D_{wc} = 17.2492 \text{ cm}^2 \text{ s}^{-1}$ .

It should be noted that the diffusion coefficient varies with concentration, but at low concentrations it can be assumed constant.

### 2.2.3 Water Vapour Diffusion in the Martian Regolith

One of the simplest forms of the diffusion coefficient correction in a porous medium is [Mason and Malinauskas, 1983],

$$D^p = \frac{\phi}{\tau} D_{12} \quad (2.54)$$

Hence,

$$J_{Diff} = -D^p \frac{\partial \rho_1}{\partial z} \quad (2.55)$$

where  $\rho_1$  is the partial density of species 1 in 2. Additionally, another correlation can be used for the porous medium effects on the diffusion coefficient,

$$D_p = D_{12} \frac{\phi^2}{\tau} \quad (2.56)$$

Using this relation, Zent et al. [1986] and Mellon and Jakosky [1993] assumed constant tortuosity, with the former authors assuming an approximate value of 5.

This formulation is valid when the diffusion is purely Fickian. However, diffusion in the Martian regolith will most likely be in the transition diffusion regime. This is when the pore size is in the order of the mean free path of the diffusive species. In this case, diffusion will have a mixed Fickian and Knudsen diffusion character [Mason and Malinauskas, 1983, Satterfield, 1981].

The Knudsen diffusion takes place when the mean free path of a gas is much greater than the pore length scale ( $\lambda \gg \lambda_p$ ). In this case, intermolecular collisions are negligible compared to the molecule-wall collisions. This type of diffusive flux depends on the molecular weight and the temperature of the gas and the pore length scale. On Mars, Hudson et al. [2007] calculated the mean free path of water vapour in CO<sub>2</sub> at 600 Pa and 200 K to be 9  $\mu\text{m}$  with the relations from Chapman and Cowling [1970].

In the Knudsen diffusion regime, the diffusive flux depends on mass concentration gradient of the diffusive species alone [Mason and Malinauskas, 1983],

$$J_1 = -D_K \frac{\partial \rho_1}{\partial z} \quad (2.57)$$

In this case, the Knudsen diffusion coefficient ( $D_K$ ) depends on the mean velocity of the molecule. At pressures where the diffusive regime is not completely Knudsen ( $\frac{r}{\lambda_1} \ll 1$ ) or Fickian diffusion, the effective diffusion coefficient is obtained from the Bosanquet relation.

In this case (simplest form), the effective diffusivity for a binary species transition diffusion can be defined as:

$$\frac{1}{D'} = \frac{1}{D_K} + \frac{1}{D_{wc}} \quad (2.58)$$

and applying the porous medium correction,

$$D_{eff} = \frac{\phi}{\tau} D' \quad (2.59)$$

and again, the Fick's law with  $D_{eff}$  can be used to obtain the net flux:

$$J_{Diff} = -D_{eff} \frac{\partial \rho_w}{\partial z} \quad (2.60)$$

where  $\rho_w$  is the density of water vapour and  $D_{eff}$  is the effective diffusion coefficient of water vapour in CO<sub>2</sub>.

Clifford [1993] estimated that Knudsen diffusion is dominant in the Martian regolith, which is an icy soil with pore sizes in the order of microns. They calculated the Knudsen diffusion coefficient using,

$$D_K = \frac{2}{3} r \left( \frac{8TR}{\pi M} \right)^{\frac{1}{2}} \quad (2.61)$$

$M$  is the species molecular weight (water here),  $T$  is temperature,  $r$  is pore radius and  $R$  is the universal gas constant. Fisher [2007] calculated  $r$  to be in the range of 1 to 10  $\mu\text{m}$  at the typical Mars north pole conditions. By using similar relationships, Fisher [2007] calculated a value of  $D_{eff}=2.6 \text{ cm}^2 \text{ s}^{-1}$  for 50% porosity, which he noted is typical for a fine grain regolith.

Since state of the art experimental studies have been conducted to evaluate the effective diffusivity of water vapour in  $\text{CO}_2$  and some porous properties of the regolith, theoretical calculation of these properties is not necessary for this study. In the following, a summary of typical values for the regolith porous medium properties used in different Mars related work are outlined. From these work, suitable values are selected for this study.

In a regolith transport study on Mars by Smoluchowski [1968], diffusion coefficients were calculated to be in the range of  $4 \times 10^{-4}$  to  $12 \text{ cm}^2 \text{ s}^{-1}$ . The lower value corresponds to a regolith with particle sizes smaller than 10  $\mu\text{m}$  and a porosity of 1 to 10% and the higher end represents a regolith with particle sizes in the range of 10 to 200  $\mu\text{m}$  and a porosity of 50 to 80%, respectively.

Values of 0.4 to  $13.6 \text{ cm}^2 \text{ s}^{-1}$  were suggested by Flasar and Goody [1976], which were calculated at 610 Pa and 210 K. Jakosky [1983] recommends using a value in the range of 1 to  $3 \text{ cm}^2 \text{ s}^{-1}$  for Mars, due to the reason that when he employed a value of  $1 \text{ cm}^2 \text{ s}^{-1}$  in his model, he found it compatible with seasonal water content change in the atmosphere at the  $25^\circ \text{ N}$  latitude.

For a porosity of 50% and a tortuosity value of 5, again at 610 Pa and 210 K, a gas diffusivity of  $13.2 \text{ cm}^2 \text{ s}^{-1}$  and regolith diffusivity of  $0.44 \text{ cm}^2 \text{ s}^{-1}$  is calculated by Fanale et al. [1986]. Assuming pore sizes from 1 to 10  $\mu\text{m}$ , they suggest values of 0.02 to  $0.22 \text{ cm}^2 \text{ s}^{-1}$  for the Knudsen diffusion coefficient. For the typical ambient values of 600 Pa and 200 K, assuming a pore size of 1 to 10  $\mu\text{m}$ , Mellon and Jakosky [1993] recommended using effective diffusion

coefficient values of 2 to 10  $\text{cm}^2\text{s}^{-1}$ .

Moreover in a series of rigorous experiments, Hudson et al. [2007] used a variety of materials that could resemble the Martian regolith, e.g. JSC Mars-1 compound, 40 to 70  $\mu\text{m}$  glass beads and 1 to 3  $\mu\text{m}$  powder. Effective diffusion coefficients ( $D_{eff}$ , which is the real coefficient including all the obstruction and Knudsen effects) and obstruction factors ( $\text{O.F.} = \frac{D_{eff}}{D_{wc}}$ , also defined in 3.1) were calculated for many cases of different pressure, temperature and column heights using these material. Values that were deemed suitable for the Martian north pole conditions were selected and are summarized in Table 2.1.

Regolith thickness, cm	P, Pa	$T_{Reg}$ , K	$D_{eff}$ , $\text{cm}^2 \text{s}^{-1}$	O.F.
2.10	598	263	$4.41 \pm 0.42$	$0.17 \pm 0.02$
4.95	594	263	$5.01 \pm 0.42$	$0.19 \pm 0.02$
9.79	588	263	$5.54 \pm 0.45$	$0.21 \pm 0.02$
2.08	592	253	$3.87 \pm 0.59$	$0.21 \pm 0.03$
5.02	572	253	$3.49 \pm 0.16$	$0.15 \pm 0.02$
4.92	1173	263	$2.58 \pm 0.21$	$0.19 \pm 0.02$

Table 2.1: Effective diffusion coefficients ( $D_{eff}$ ,  $\text{cm}^2 \text{s}^{-1}$ ) for samples of 40-70  $\mu\text{m}$  Glass Beads at different regolith depths, pressures and temperatures from experimental work of Hudson et al. [2007]

Relative humidity for all the experiments in Table 2.1 were in the range of 7 to 11 % except the experiment in line 4, which RH was 22.4%. The diffusion coefficient values in Table 2.1, except for the last case, are the corrected values from raw experimental data, i.e. they represent the diffusion coefficients in the regolith samples and do not include interfacial and non-porous diffusion effects. Since Hudson et al. [2007] noted that for the 40 to 70  $\mu\text{m}$  glass beads with thicknesses between 2 to 5 cm, the porous effect correction is negligible, for the last case, which is at a different pressure, we simply use the raw diffusion coefficient value available from their experiments.

## 2.3 Numerical Method

### 2.3.1 Numerics in Fluid Mechanics

Analytical solutions for the equations of fluid motion are very difficult to obtain except for cases with simple physics and geometries. Therefore, for most engineering applications, solutions are achieved either by approximations based on a combination of analytical, empirical and dimensional analysis procedures or by numerical methods. During recent years, solving fluid flow problems with numerical methods has become increasingly popular due to the mass production of cheap and powerful computers.

With such numerical methods in fluid mechanics, the differential equations that govern the fluid transport are reduced to many algebraic equations with discretization procedures in order to be solved with a computer. Discretization of a fluid domain means that it is divided into smaller domains where the equations are approximated at, i.e. approximate equations are solved at discretized pieces in the domain.

There are several discretization methods for differential equations such as the Finite Difference Method, the Finite Elements Method and the Finite Volume Method (FVM). The latter method is used in this study. In FVM, the domain is divided into finite control volumes. The integrated form of the transport equations (in vector notation, Eqn. 2.62) are then approximated at each control volume and solved for the center point of the domain.

$$\frac{\partial}{\partial t} \int_V \rho \varphi dV + \int_S \vec{n} \cdot (\rho \varphi \vec{u}) dS = \int_S \vec{n} \cdot (D_\varphi \nabla \varphi) dS + \int_V q_\varphi dV \quad (2.62)$$

In Eqn. 2.62,  $\varphi$  is an intensive transport quantity,  $D_\varphi$  is the diffusivity coefficient and  $S_\varphi$  is the source term. The advantages of this method are its being very accommodating to complex grids and geometries, being the most efficient method for heat and flow problems, having meaningful physical interpretation for the approximation terms and implicitly conserved quantities.

Numerical methods allow us to solve complex fluid equations that currently can not be solved by other means, however, a numerical solution is basically an approximation. There may be

many errors associated with numerical results, for example, originating from discretization errors, round off and approximation errors inherited in numerical calculations and errors resulting from unsuitable mathematical equations for the physical problem. Therefore, a numerical procedure should be set up as carefully as possible to avoid unknown errors. This is usually achieved by setting up proper mathematical equations for the problem, avoiding known causes of error in the numerical solver procedure, accompanying the numerical method with experiments and simpler analytical benchmarks and understanding the approximation level of the solution.

In the following, some general numerical solving procedures and their implementation for the problem in this study are discussed.

### 2.3.2 Solving with CFX

For the current study, CFX-11.0 is used as a numerical solver for the transport equations. CFX is a finite volume, second order solver and a product of the ANSYS company.

### 2.3.3 Winds and Natural Convection Transport Equations in CFX

The transport equations for the wind and natural convection simulations over the Martian regolith and the water vapour transport were outlined in the previous section. Here, certain implementations in the equations used by CFX are provided [ANSYS, 2008].

If the transport of an additional variable, which is water vapour density in this study, is turbulent, then the following transport equation is used,

$$\frac{\partial(\rho\varphi)}{\partial t} + \nabla \cdot (\rho \vec{U} \varphi) = \nabla \cdot \left[ \left( \rho D_\varphi + \frac{\mu_t}{Sc_t} \right) \nabla \varphi \right] + S_\varphi \quad (2.63)$$

where  $\mu_t$  is the turbulent eddy viscosity and  $Sc_t$  is the turbulent Schmidt number.

When the k- $\epsilon$  model is used for turbulent natural convection simulations with the Boussinesq

approximation, a buoyancy production term is used in the  $k$  and  $\epsilon$  equations, which are defined as,

$$P_{kb} = \frac{\mu_t \beta}{\sigma_\rho} \vec{g} \cdot \nabla T \quad (2.64)$$

and if  $P_{kb}$  is positive,

$$P_{\epsilon b} = C_3 \cdot \text{Max} \{0, P_{kb}\} \quad (2.65)$$

where  $\sigma_\rho$  and  $C_3$  are equal to 0.9 and 1 respectively. The buoyancy production term in the  $k$ - $\omega$  model can be defined similar to the  $k$ - $\epsilon$  model.

### 2.3.4 Meshing

As previously mentioned, the objective is to perform a 3-D analysis of local atmospheric winds and natural convection at a near surface local domain on Mars, which provides much insight into the local water vapour transport and how it could affect a lander.

For this purpose, a 3-D model domain should be discretized into finite control volumes for the numerical solver. Three dimensional domains were created using the ANSYS-Workbench, a 3-D modelling software and subsequently meshed with an unstructured tetrahedral mesh using the ANSYS CFX-Mesh programme. The unstructured mesh type allows for fast automatic meshing of the domain but it has the disadvantages of introducing larger artificial diffusion in the solution and requiring more computer resources to solve. These problems can be overcome by using powerful computers and ensuring the grid independence of the solution. Additionally, structured inflated layers were used at special locations to allow for some alignment with the boundary layer flow. In locations where the flow structure was important to the analysis, a higher mesh resolution was used. For example the atmosphere-regolith interface was a special location where inflated, structured mesh with a higher resolution (local refinement) was used. It is important to refine this region because it includes the velocity and water vapour concentration boundary layer, and it is where the



water vapour diffusion to the atmosphere and the near surface water amount is calculated for analysis.

In CFX, solution fields are stored at the mesh nodes, but many equations need to be numerically solved at different integration points in a control volume element. This is achieved by using the finite element shape functions which for a transport quantity  $\varphi$  require that,

$$\varphi = \sum_{i=1}^n N_i \varphi_i \quad (2.66)$$

where  $n$  is the number of nodes in an element,  $N_i$  is the shape function which has the constraint,

$$\sum_{i=1}^n N_i = 1 \quad \text{and at node } j, N_i = \begin{cases} 1 & : i = j \\ 0 & : i \neq j \end{cases} \quad (2.67)$$

and for a tetrahedra element,

$$\begin{aligned} N_1(s, t, u) &= 1 - s - t - u \\ N_2(s, t, u) &= s \\ N_3(s, t, u) &= t \\ N_4(s, t, u) &= u \end{aligned} \quad (2.68)$$

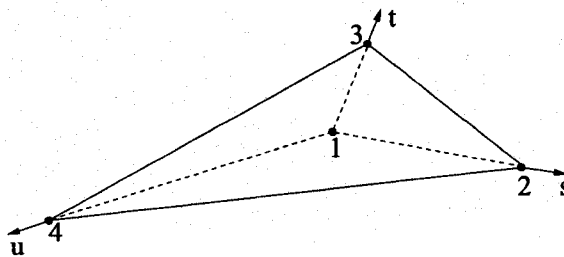


Figure 2.1: The tetrahedra element.

### 2.3.5 Discretization of the Transport Terms

The integrated form of the transport equations for a control volume in general are,

$$\frac{\partial}{\partial t} \int_V \rho dV + \int_s \rho U_j dn_j = 0 \quad (2.69)$$

$$\frac{\partial}{\partial t} \int_V \rho U_i dV + \int_s \rho U_j U_i dn_j = - \int_s P dn_j - \int_s \mu_{eff} \left( \frac{\partial U_i}{\partial x_j} + \frac{\partial U_j}{\partial x_i} \right) dn_j + \int_V S dV \quad (2.70)$$

$$\frac{\partial}{\partial t} \int_V \rho \varphi dV + \int_s \rho U_j \varphi dn_j = \int_s D_\varphi \frac{\partial \varphi}{\partial x_j} dn_j + \int_V S_\varphi dV \quad (2.71)$$

$dn_j$  is the unit normal surface vector being outward positive. When there is a surface integration, a flux through the surface is calculated and the volume integrals are source terms. In order to discretize the integral equations to algebraic equations, the surface integrals are calculated at the mid-point of the faces of a control volume element ( $ip$ ). The discretized form of the equations are,

$$V \left( \frac{\rho - \rho^o}{\Delta t} \right) + \sum_{ip} (\rho U_j \Delta n_j)_{ip} = 0 \quad (2.72)$$

$$V \left( \frac{\rho U_i - \rho^o U_i^o}{\Delta t} \right) + \sum_{ip} \dot{m}_{ip} (U_i)_{ip} = \sum_{ip} (P \Delta n_i)_{ip} + \sum_{ip} \left[ \mu_{eff} \left( \frac{\partial U_i}{\partial x_j} + \frac{\partial U_j}{\partial x_i} \right) dn_j \right]_{ip} + S V \quad (2.73)$$

$$V \left( \frac{\rho \varphi - \rho^o \varphi^o}{\Delta t} \right) + \sum_{ip} \dot{m}_{ip} (\varphi)_{ip} = \sum_{ip} \left( \mu_{eff} \frac{\partial \varphi}{\partial x_i} dn_j \right)_{ip} + S_\varphi V \quad (2.74)$$

Values with the superscript “ $o$ ” are from the previous time step in the time discretized terms and surface mass flux,  $\dot{m}_{ip}$ , is defined as  $\dot{m}_{ip} = (\rho U_j \Delta n_j)_{ip}$ .

For the transient terms in the discretized integral equations, the second order backward Euler scheme was used,

$$\frac{\partial}{\partial t} \int_V \rho \varphi dV \simeq \frac{V}{\Delta t} \left[ \frac{3}{2} (\rho \varphi) - 2 (\rho \varphi)^o + \frac{1}{2} (\rho \varphi)^{oo} \right] \quad (2.75)$$

This scheme is implicit and second order accurate in time which demonstrates a good degree of robustness.

The discretized diffusion terms, using the shape functions described in the previous section are defined as,

$$\left(\frac{\partial \varphi}{\partial x}\right)_{ip} = \sum_n \left(\frac{\partial N_n}{\partial x}\right)_{ip} \varphi_n \quad (2.76)$$

The discretized pressure gradient term is defined as,  $(P\Delta n_{ip})_{ip}$  where,

$$P_{ip} = \sum_n N_n(s_{ip}, t_{ip}, u_{ip}) P_n \quad (2.77)$$

The discretized advection term is defined as,

$$\varphi_{ip} = \varphi_{up} + \beta \nabla \varphi \cdot \Delta \vec{r} \quad (2.78)$$

where  $\varphi_{up}$  is the upwind node value of  $\varphi$  and  $\vec{r}$  is a vector from the upwind node to  $ip$ . In this study, the High Resolution scheme for the discretization of the advection term is used, which is a special CFX implementation [ANSYS, 2008]. In this scheme,  $\beta$  is locally computed to be close to 1 to avoid oscillations and it is defined from the method in [Barth and Jespersen, 1989]. The  $\nabla \varphi$  is the control volume gradient at the upwind node. The advantages of this scheme are that it is bounded, accurate, prevents local oscillations and becomes first order at discontinuities.

### 2.3.6 Solving the Algebraic Equations and Convergence

The discretized transport equations form a linear system of equations,

$$\sum_j a_i^j \varphi_i^j = b_i \quad (2.79)$$

where  $i$  and  $j$  denote the node number and the neighbor node respectively. This system of equations is then solved with the Algebraic Multigrid accelerated Incomplete Lower Upper factorization method [ANSYS, 2008].

The algebraic equations are solved iteratively to obtain a better solution of  $\varphi^{n+1}$  than  $\varphi^n$ , correcting it by  $\varphi'$  at each iteration,  $\varphi^{n+1} = \varphi^n + \varphi'$ .  $\varphi'$  is obtained from  $A\varphi' = r^n$  and  $r^n$  is the residual,  $r^n = b - A\varphi^n$ . When the normalized residual reaches a convergence target, the iterative calculations terminates.

### 2.3.7 Grid and Domain Independence

The numerical solutions obtained for the transport equations should not depend on the grid size and the domain size. The grid dependence is ensured by obtaining solutions at different grid levels and verifying that the difference is less than a desirable value.

To reach a closer solution to the exact differential equations solution, the discretization error of the code should be corrected. The discretization error, which is generated by the truncation error (the truncation error of the Taylor series), is defined as,

$$\epsilon_h^d = \Phi_e - \varphi_h \quad (2.80)$$

where  $\Phi_e$  and  $\varphi_h$  are the exact solution and the algebraic equations solution at grid level  $h$  respectively. For grids that are adequately fine, the truncation error can be expressed by the Taylor series' leading term,

$$\epsilon_h^d = \varphi_h + \alpha' h^p + H = \varphi_{\lambda h} + \alpha' (\lambda h)^p + H \quad (2.81)$$

where  $H$  is the higher order terms and  $\alpha'$  depends on the derivatives at a given point. The order of the scheme,  $p$ , then can be calculated by,

$$p = \frac{\log\left(\frac{\varphi_{\lambda h} - \varphi_{2\lambda h}}{\varphi_h - \varphi_{\lambda h}}\right)}{\log\lambda} \quad (2.82)$$

and  $\lambda$  is the expansion factor between two successive grids. If the order of the scheme obtained from the above equation is what is expected from the code scheme, then the following relation can be used to obtain the discretization error to obtain a closer approximation of the exact solution ( $\Phi_e$ ).

$$\epsilon_h^d \simeq \frac{\varphi_h - \varphi_{\lambda h}}{\lambda^p - 1} \quad (2.83)$$

This method is called the Richardson extrapolation and provides an accurate result when the convergence is monotonic [Ferziger and Peric, 1996].

Moreover, the size of the domain may influence the numerical solution. For example if a flow is along a channel, the length of the channel may affect the upstream values. In order to avoid the influence of the domain, several domain sizes must be checked for consistency.

## 2.4 The Special Sherwood Number

Since the complete physics of water transport on Mars involves numerous extensive subjects (e.g. multi-component mass transport, porous media, gas dynamics, diffusion and atmospheric physics), it is very complex to include all the necessary physics in a model and one may only be interested in a part of this large physical model and not want to deal with other complexities. To address this issue, one objective of this study is to determine a non-dimensional number that is normalized by a linearized mass concentration gradient in the regolith for different ambient conditions on the regolith surface. This non-dimensional value allows a researcher, who is not interested in the detailed study of the regolith, to determine the mass flux to the atmosphere by only knowing the water vapour mass concentration values at an arbitrary regolith depth and at a near surface location. This non-dimensional number is a special Sherwood number, which can be used to summarize the numerical simulation results for different parameter studies.

The water vapour concentration profile in the regolith, is in general, non-linear due to the effect of surface flows and other diffusion mechanisms. Therefore, it is convenient to linearize a general concentration gradient profile and determine an effective linear coefficient, which includes the non-linear effects, implicitly, so that one can easily calculate the total water flux by assuming a linear profile, i.e. by knowing only the mass concentration at two points. This coefficient is a special Sherwood number, that when multiplied by the linear vapour flux, yields the real flux to the atmosphere.

The Sherwood number, which is the ratio of the convective to diffusive mass transport is originally defined as:

$$\text{Sh} = \frac{k_m l_0}{D_{eff}} \quad (2.84)$$

where  $k_m$  is the mass transfer coefficient,  $D_{eff}$  is the effective diffusivity and  $l_0$  is a characteristic length. The special Sherwood number ( $\text{Sh}^*$ ) that is defined in this study is different from the traditional Sherwood number ( $\text{Sh}$ ) in a sense that in order to calculate the normalizing linear water gradient, an arbitrary point with known water concentration in the atmosphere is used, whereas for  $\text{Sh}$ , the linear gradient is calculated in the regolith, therefore,

$$\text{Sh}^* = \frac{D_{eff} \left( \frac{\partial \rho_w}{\partial z} \right)_{z_r}}{D_{eff} \frac{\overline{\rho_w^{ice}} - \overline{\rho_w^{z_s}}}{L}} \quad (2.85)$$

where  $\overline{\rho_w^{ice}}$  and  $\overline{\rho_w^{z_s}}$  are the average surface integral of water vapour density at the ice table (known water concentration) and at an arbitrary near surface height ( $z_s$ ), respectively.  $\left( \frac{\partial \rho_w}{\partial z} \right)_{z_r}$  is the average surface integral of water vapour concentration gradient at an arbitrary depth,  $z_r$ , very close to the surface in the regolith and  $L$  is the distance between  $\overline{\rho_w^{z_s}}$  and  $\overline{\rho_w^{ice}}$ . With the Sherwood number defined for a particular simulation case, the water vapour flux from the regolith can be readily calculated given water vapour mass concentrations at the two points, one inside the regolith at the top of the ice table and one at the near surface atmosphere, and the characteristic distance between these points ( $L$ ).

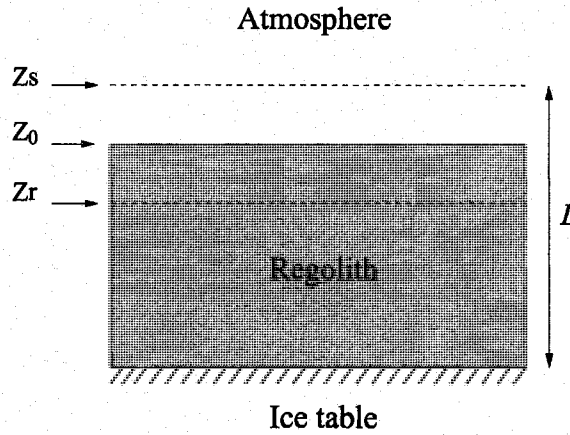


Figure 2.2: An illustration of the local locations of interest for calculating  $\text{Sh}^*$ .

# Chapter 3

## Numerical Simulations

### 3.1 Horizontal Winds

Horizontal winds regularly flow on Mars' surface with velocities as high as  $200 \text{ m s}^{-1}$  [Kieffer et al., 1992]. Winds are an important agency for particle and volatile substance transport on Mars. Water vapour and dust are shifted on the Martian surface at local and global scales by winds. Furthermore, winds can affect water vapour transport within the regolith and affect its diffusion rate to the atmosphere. Winds can enhance water vapour diffusion in the near surface regolith by sweeping away the near surface water concentration, thus imposing a larger concentration gradient that results in a higher vapour flux from an ice table to the surface.

In general, local winds can be part of a larger scale natural convection flow. At a small scale, much smaller than the natural convection cell, these winds may be indistinguishable from regular horizontal winds. Therefore, the overall air flow in a region may consist of a local thermal convective motion, superposed with local winds, which may themselves be part of a larger scale natural convection cell. In order to better understand the natural convection flow in a region, the flow of winds and their effect on water vapour transport are simulated and studied.

To simulate horizontal winds, a domain with both a porous region and a pure fluid region is created. This domain roughly represents a simplified local landing site. The shape of



the domain is a rectangular cube which is divided into two parts, a top part representing the atmosphere (fluid region) and a bottom part representing the regolith (porous region). The domain is 6 m long and 3 m wide. The top atmosphere part is 3 m high and the bottom regolith part is variable using values ranging from 0.05 to 0.2 m, in order to predict different possible scenarios at the Phoenix landing site. This cubic domain was discretized using unstructured tetrahedra mesh with a total of 372,654 nodes (Fig. 3.1). An area refinement was applied using inflated layers at the atmosphere-soil interface with a first layer thickness of  $1.8 \times 10^{-4}$  m (Fig. 3.2). The mesh size systematically increases from a high resolution at the interface, to coarser control volumes at the top of the atmosphere part. Such use of inflation at interfaces and of coarser size mesh at areas with less interest reduces the computation effort.

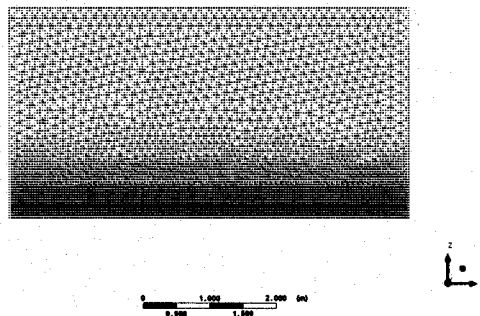


Figure 3.1: View of the unstructured tetrahedra mesh with local structured refinement used for the horizontal winds domain.

The effects of several different boundary conditions were tested on the simulation results. Convergence failure and non-physical results were outcomes of incorrect or unsuitable boundary conditions. In this chapter, the model with the best boundary conditions is described.

At the top boundary of the atmosphere domain and at the bottom boundary of the regolith domain, a free slip wall boundary with prescribed water vapour concentration was applied. If 100% relative humidity is assumed at the regolith bottom boundary, which is the ice-regolith interface, then the water amount at this boundary can be calculated. Since  $RH = P_{wv} / P_{sat}$ , then if  $RH = 100\%$ ,  $P_{wv} = P_{sat}$  and from the ideal gas law, water amount corresponding to a

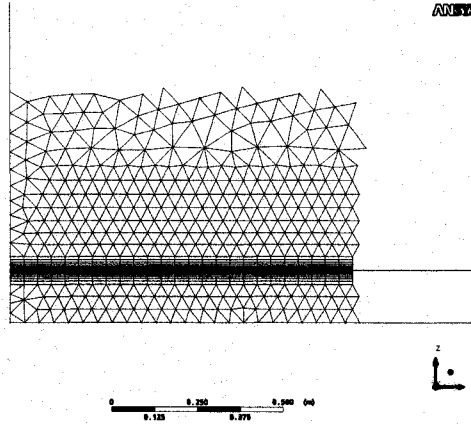


Figure 3.2: A detailed view of the local structured refinement at the atmosphere-regolith interface, used for the horizontal winds domain.

saturated environment can be calculated,

$$\rho_{wv} = \frac{P_{sat} M_w}{RT} \quad (3.1)$$

$P_{sat}$  is only a function of temperature and can be obtained from the saturation vapour pressure of ice proposed by [Marti and Mauersberger, 1993],

$$\log P_{sat} = \frac{A_1}{T} + B_1 \quad (3.2)$$

Where  $A_1 = -2663.5 \pm 0.8$ ,  $B_1 = 12.537 \pm 0.011$  and the unit of  $P_{sat}$  is Pa. Moreover, for temperatures below 170 K, water ice vapour pressure can be obtained from Mauersberger and Krankowsky [2003],

$$\log P_{sat} = \frac{A_2}{T} + B_2 \quad (3.3)$$

Where  $A_2 = -3059 \pm 26$ ,  $B_2 = 14.88 \pm 0.15$  and the unit of P is Pa.

In the simulations, a relative humidity of 100% was assumed at the soil bottom boundary and the corresponding vapour density was calculated at the domain temperature, thus

representing the saturation state at the top of the ice table.

At the top atmosphere boundary, an arbitrary value in the range of the boundary layer water concentration found by [Savijarvi, 1995] was prescribed. Since the reported water amount in the atmosphere in this study has the unit of precipitable water in microns (PR  $\mu\text{m}$ ), the conversion procedure to  $\text{kg m}^{-3}$  is described here. For the  $\text{CO}_2$  density in the atmosphere, an exponential profile is assumed, where  $\rho_{\text{CO}_2}^{\text{surf}}$  is the density of  $\text{CO}_2$  at the surface, thus,  $\rho_{\text{CO}_2} = \rho_{\text{CO}_2}^{\text{surf}} \exp(-z/H)$ . PR  $\mu\text{m}$  is defined as,

$$\text{PR} = \int_0^H \rho_w(z) dz \quad (3.4)$$

where  $\rho_w$  is the atmospheric water vapour content and if the water- $\text{CO}_2$  mixing ratio,  $r = \rho_w(z)/\rho_{\text{CO}_2}(z)$  is assumed constant in the atmosphere,

$$\text{PR} = r \int_0^H \rho_{\text{CO}_2}^{\text{surf}} \exp\left(\frac{-z}{H}\right) dz \quad (3.5)$$

therefore,

$$r = \frac{10^{-6} \text{PR}}{0.63 \rho_{\text{CO}_2}^{\text{surf}} H} \quad (3.6)$$

$\rho_{\text{CO}_2}$  and  $\rho_{\text{CO}_2}^{\text{surf}}$  can be determined with the ideal gas law, assuming that other constituents of the Martian atmosphere are negligible. For the atmospheric pressure of 600 Pa and surface temperature of 263 K,  $\rho_{\text{CO}_2}^{\text{surf}} = 0.012 \text{ kg m}^{-3}$  and similarly for the same pressure and  $T = 220 \text{ K}$  at a 3 m height above the surface,  $\rho_{\text{CO}_2}(3\text{m}) = 0.014 \text{ kg m}^{-3}$ . If the water amount in the atmosphere is selected to be 1 PR  $\mu\text{m}$  (a conservative minimum value), then  $\rho_w(3\text{m}) \simeq 6 \times 10^{-7} \text{ kg m}^{-3}$  which is the prescribed value for water amount at the top boundary of the numerical domain.

The inlet boundary is prescribed with velocity and water concentration. The values for average velocity were obtained from a 1-D Martian Planetary Boundary Layer dynamics model with E-1 turbulence closure scheme [Taylor et al., 2007] for the geostrophic winds  $\bar{U}_g$

=5, 10, 20, 35 m s<sup>-1</sup>. This inlet profile data for our numerical model will be referred to as the original wind profiles.

Within the height of 3 m above the surface, profile data were available at only seven data points for velocity and turbulence kinetic energy. To produce a smooth and fine resolution profile at the inlet boundary, 60 extra points were interpolated using the Akima polynomial procedure [Akima, 1970] (Fig. 3.3). Compared to interpolation with Splines or a 2nd order polynomial, the Akima interpolation scheme shows a relatively better fit for the seven data points of the profiles (Figs. 3.4 and 3.5). These additional data points are required by the code for a clean boundary condition profile. Additionally, the code applies linear interpolation between the 60 Akima interpolated data points if required.

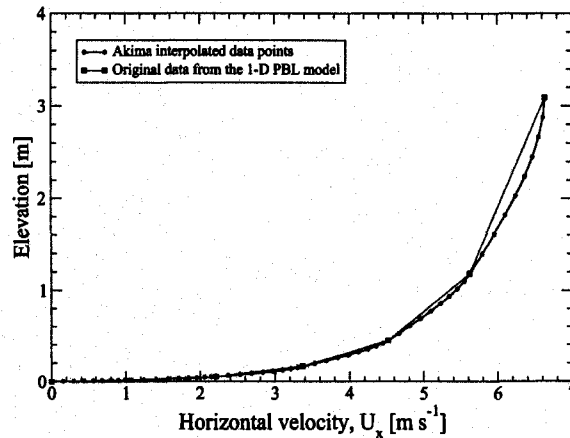


Figure 3.3: Example of an interpolated velocity profile at the domain inlet boundary with the Akima interpolation scheme. (case of 10 m s<sup>-1</sup> free stream velocity).

In addition to the wind profiles mentioned above, three other wind profiles with the free stream velocities of 0.5, 1 and 2 m s<sup>-1</sup> were created to obtain results at low wind speeds. In order to obtain these profiles, the horizontal component ( $U_x$ ) of the original wind profiles at 2 m above the surface were plotted (Fig. 3.6). Since the velocity increase at 2 m is approximately linear with  $\bar{U}_g$ , it was assumed that other profiles can be obtained by a constant multiplication factor (Fig. 3.7). For this purpose, the original, Akima interpolated velocity of  $\bar{U}_g = 5$  m s<sup>-1</sup> profile was selected and all the profile values were multiplied by 1/10, 1/5 and 2/5 to obtain the 0.5, 1 and 2 m s<sup>-1</sup> velocity profiles, respectively. The complete set of wind profiles are shown in Fig. 3.8.

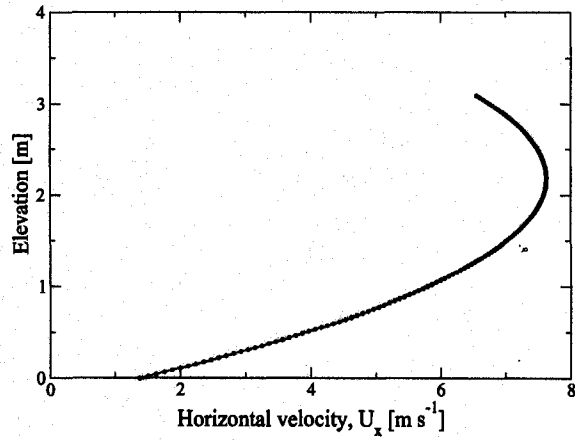


Figure 3.4: Example of an interpolated velocity profile at the domain inlet boundary with a 2nd order polynomial (case of  $10 \text{ m s}^{-1}$  free stream velocity).

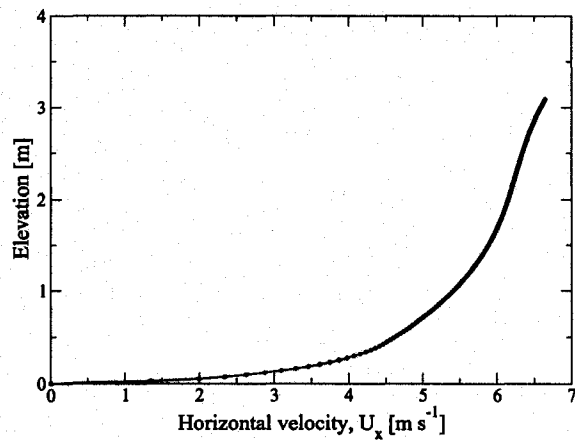


Figure 3.5: Example of an interpolated velocity profile at the domain inlet boundary with the Spline interpolation scheme (case of  $10 \text{ m s}^{-1}$  free stream velocity).

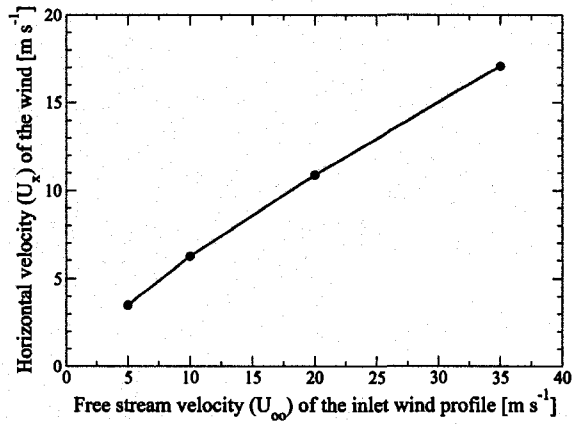


Figure 3.6: Horizontal velocity ( $U_x$ ) at 2 m above the surface versus the free stream velocity of the original inlet wind profiles.

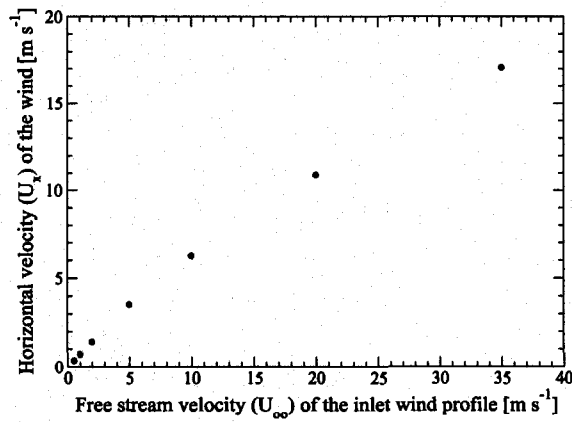


Figure 3.7: Horizontal velocity ( $U_x$ ) at 2 m above the surface versus the free stream velocity of the inlet wind profiles.

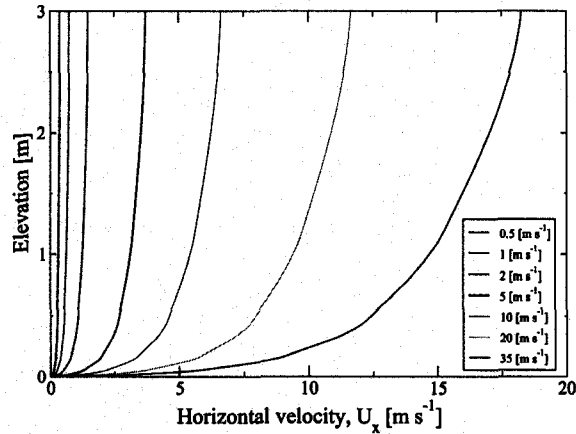


Figure 3.8: Horizontal velocity ( $U_x$ ) profiles for 0.5, 1, 2, 5, 10, 20, 35  $\text{m s}^{-1}$  winds.

At the outlet, the side of the atmosphere domain where flow is exiting, an outlet boundary condition was applied with a zero relative average static pressure condition. At the atmosphere-regolith interface, conservative flux for all transport variables was applied and a symmetry boundary condition was prescribed for the sides.

Two surfaces that required attention, were the regolith faces perpendicular to the wind direction, just below the inlet and outlet atmosphere boundaries described above. Convergence issues arise when these surfaces are treated as “openings”, a numerical boundary type that allows both inflow and outflow. If these surfaces are treated as symmetry or wall type of boundary, they produce non-physical near wall values, resulting in the erroneous accumulation of water vapour at the surface facing the wind. To solve this problem, a periodic translational boundary pair was implemented at these surfaces, i.e quantities exiting surface B will enter surface A. This boundary type better represents flow in the soil due to horizontal winds on the surface (Fig. 3.9).

Using the assumptions, several scenarios of water vapour transport subject to horizontal winds were simulated. Simulations were performed with different free stream wind velocities, regolith depths, pressures and temperatures.

The selected soil depths are in the range expected to be encountered at Phoenix’s landing site. From the TES (Thermal Emission Spectroscopy) readings on board the Mars Global Surveyor, ice is most probable to be found within a few centimeters under the surface

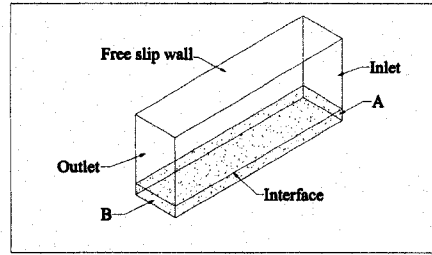


Figure 3.9: The local scale domain for the horizontal wind simulations.

[Bandfield et al., 2008] and many models assume ice under a shallow dry regolith layer [Feldman et al., 2007]. The regolith depths selected for the simulations are 5 cm, 7 cm, 10 cm, 15 cm and 20 cm.

All horizontal wind simulations are steady state and isothermal. The flow was assumed to be laminar partly because although the geostrophic wind profiles, which were used as the inlet boundary condition, were obtained from a 1-D turbulent planetary boundary layer model, it is possible that the atmospheric turbulence intensity is low at certain times of the day, especially at low average wind speeds, when the flow could be considered transitional. If the surface flow is in the transition regime or has low levels of turbulence, the Reynolds Averaged turbulence models, such as the  $k-\epsilon$  model, are known to overestimate the effects of turbulence. Since the use of more advanced turbulence models, such as Large Eddy Simulations, which could resolve the transitional regime, is beyond the scope of this work, an alternative approach would be to consider the pure laminar regime as a limiting case for possible flux values. As will be seen in the later sections, the laminar flow model better resolves the local natural convection flow on Mars. Thus another advantage of using the laminar model is that, for future studies, a better compatibility is achieved when natural convection is modelled together with horizontal winds.

Simulations were performed with the variables selected as:  $T \in \{253 \text{ K}, 263 \text{ K}\}$ ,  $P \in \{600 \text{ Pa}, 900 \text{ Pa}\}$ ,  $L \in \{5 \text{ cm}, 7 \text{ cm}, 10 \text{ cm}, 15 \text{ cm}, 20 \text{ cm}\}$  and  $\bar{U}_g \in \{0.5 \text{ m s}^{-1}, 1 \text{ m s}^{-1}, 2 \text{ m s}^{-1}, 5 \text{ m s}^{-1}, 10 \text{ m s}^{-1}, 20 \text{ m s}^{-1}, 35 \text{ m s}^{-1}\}$ , where  $T$  is the domain temperature,  $P$  is the domain pressure,  $L$  is the regolith depth and  $\bar{U}_g$  is the mean free stream geostrophic wind



velocity. This free stream velocity appears at elevations higher than the domain used in this study and the velocity values for  $\bar{U}_g$  are only for easy identification of the cases. The results are reported as a function of the horizontal velocity component of the wind, averaged on a  $1 \times 1$  m  $XY$  plane at the end of the domain at 3 m above surface (Fig. 3.10), which is named  $U_x^*$  and the flow is in the  $x$  direction. This velocity is the real velocity in the domain, which can be directly incorporated in other studies.

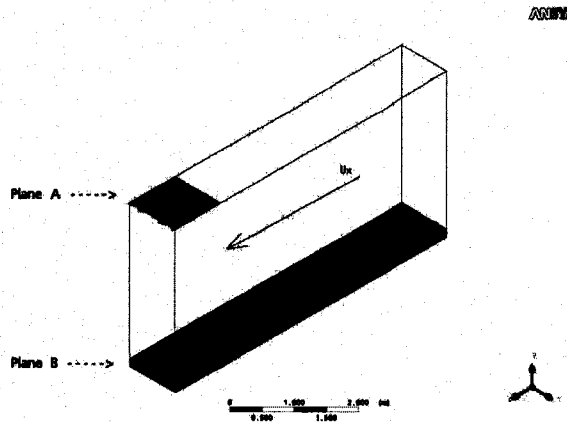


Figure 3.10: The location of planes where  $U_x^*$  (plane A) and water vapour concentration (plane B) are calculated at, in the horizontal winds domain.

For each simulation, the physical properties of the fluid and the regolith region were assumed to be constant. These properties are dependent on temperature, pressure and regolith depth and vary for different case simulations. The saturated ice table water amount is also prescribed according to the conditions for each case.

The atmospheric fluid properties at different temperatures and pressures were calculated as described in Chapter 1 and are summarized in Table 3.1.

The molecular diffusivity of water vapour in the atmosphere and the regolith porous properties were calculated by interpolating values obtained from Hudson et al. [2007] which are summarized in Table 3.2.

To include the effects of a porous medium, two parameters are set for the soil: effective porosity and permeability. The effective porosity ( $\phi_{eff}$ ) includes the porosity, tortuosity and Knudsen diffusion effects of the porous medium. This effective porosity is also known as the effective obstruction factor (O.F.). The values for effective porosities, which depend

on the domain temperature, pressure and regolith depth were also obtained from linear interpolations of experimental data from [Hudson et al., 2007] (Table 3.2). Permeability was set to  $10^{-12}$  m<sup>2</sup> for all simulation cases, close to the preferred values described in previous sections.

$T_{ref}$ , K	$P_{ref}$ , Pa	$\rho_{CO_2}$ , kg m <sup>-3</sup>	$C_P$ , J kg <sup>-1</sup> K <sup>-1</sup>	$\mu$ , Pa s	$\beta$ , K <sup>-1</sup>	$k$ , W m <sup>-1</sup> K <sup>-1</sup>
263	600	0.01207	847.183	$135.09 \times 10^{-7}$	0.00380	0.01339
253	600	0.01255	839.684	$130.67 \times 10^{-7}$	0.00395	0.01248
263	900	0.01811	847.183	$135.09 \times 10^{-7}$	0.00380	0.01339

Table 3.1: Transport properties of CO<sub>2</sub> air used in the numerical simulation.

Regolith depth, cm	P, Pa	$T_{Reg}$ , K	$D_{eff}$ , cm <sup>2</sup> s <sup>-1</sup>	O.F.
2	600	263	4.4	0.17
5	600	263	5	0.19
7	600	263	5.2	0.2
10	600	263	5.5	0.21
15	600	263	6	0.23
20	600	263	6.5	0.25
2	600	253	3.9	0.21
5	600	253	5.0	0.23
7	600	253	5.7	0.24
10	600	253	6.8	0.26
5	900	263	3.7	0.19

Table 3.2: Effective molecular diffusion coefficients ( $D_{eff}$ , cm<sup>2</sup> s<sup>-1</sup>) of water vapour in the regolith for samples of 40-70  $\mu$ m Glass Beads at different regolith depths, pressures and temperatures. Rounded, linearly interpolated or extrapolated from experimental work of Hudson et al. [2007].

At the regolith-ice interface, the ice vapour pressure and thus the boundary water amount was calculated using Eqn. 3.2 and Eqn. 3.1. For example at  $T=263$  K,  $P_{sat}=256.8$  Pa and  $\rho_{wv}^{ice}=2.11$  g m<sup>-3</sup> and at  $T=253$  K,  $P_{sat}=102.2$  Pa and  $\rho_{wv}^{ice}=0.87$  g m<sup>-3</sup>.

The base simulation case (case-1) is a domain with no wind, thus resulting in a pure diffusion of water vapour. This case enables verification of the diffusion process in the numerical model with a simple 1-D analytical model. It also allows a better observation of the effects of water transport when subject to horizontal winds.

The transport equations are solved with the High Resolution advection scheme with a convergence goal of reaching  $10E-5$  for the residual mean square (RMS) of the main transport quantities. Convergence was obtained with relative ease using the described boundary conditions. The results for this simulation are discussed using relevant illustrations.

From Fig. 3.11, the water vapour contours show a clear pure diffusion of vapour from the bottom of the regolith to the atmosphere. It is evident that diffusion through the porous part is obstructed due to a lower effective diffusivity of vapour through the regolith, which is quantitatively related to the obstruction factor (O.F.) value.

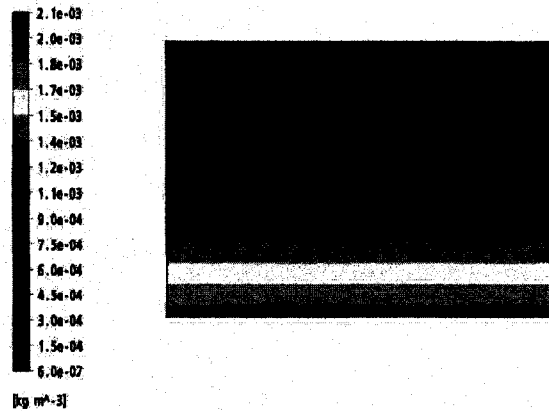


Figure 3.11: Water vapour contours in the domain. Case-1: no wind,  $T=263$  K,  $P=600$  Pa, 10 cm thick porous regolith. Elevation “0” is the regolith surface.

To better observe the obstruction effect of the porous regolith, a separate case (case-0) was simulated using a fluid domain instead of a porous domain for the regolith. This implies pure diffusion of water vapour in  $\text{CO}_2$  from the bottom of the “regolith”. It can be seen that vapour diffuses more freely in this domain of pure air (Fig. 3.12). For example on a horizontal plane, 5 mm above the regolith surface, the average water vapour concentration is  $1.8 \text{ g m}^{-3}$  for case-1 and  $2.0 \text{ g m}^{-3}$  for case-0.

For both cases, diffusion in the regolith is shown in Fig. 3.13 and Fig. 3.14. For the case-1, the water vapour amount on a line located at the middle of the domain and extending from the bottom of the regolith up to 1 m above the surface can be seen in Fig. 3.15. The values can be compared with a similar chart for case-0 (pure air “regolith”) in Fig. 3.16.

After simulating the base cases of pure diffusion, cases with different free-stream wind velocities were simulated assuming a laminar regime.

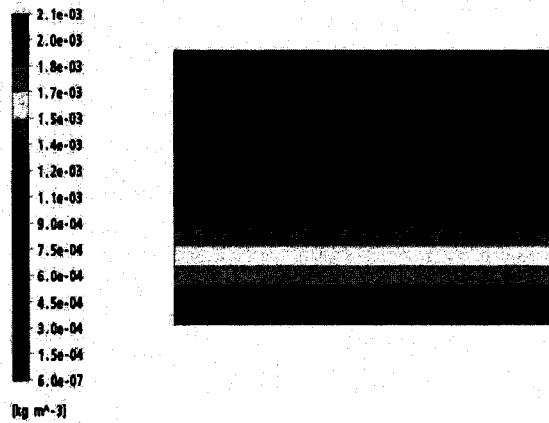


Figure 3.12: Water vapour contours in the domain. Case-0: no wind,  $T=263$  K,  $P=600$  Pa, 10 cm thick fluid “regolith”. Elevation “0” is the “regolith” surface.

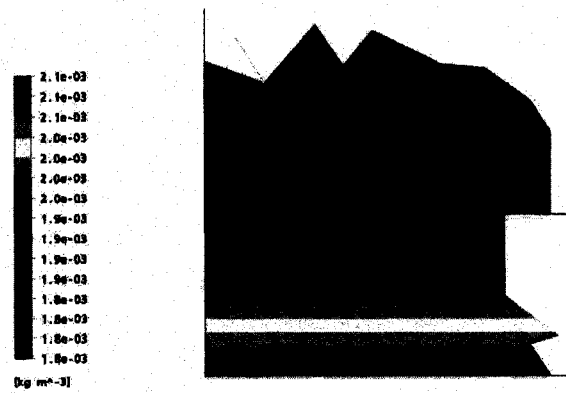


Figure 3.13: Detailed water vapour contours in the regolith. Case: no wind,  $T=263$  K,  $P=600$  Pa, 10 cm thick porous regolith.

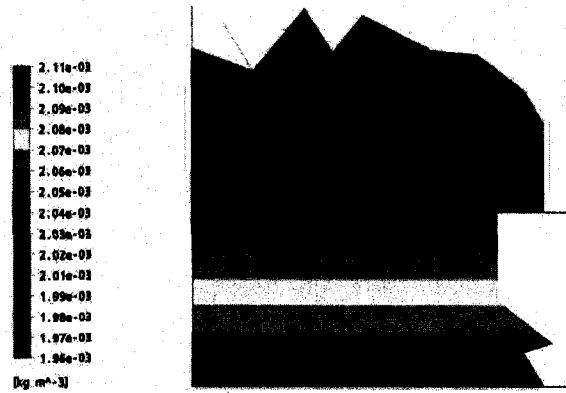


Figure 3.14: Detailed water vapour contours in the “regolith”. Case: no wind,  $T=263\text{ K}$ ,  $P=600\text{ Pa}$ , 10 cm thick fluid “regolith”.

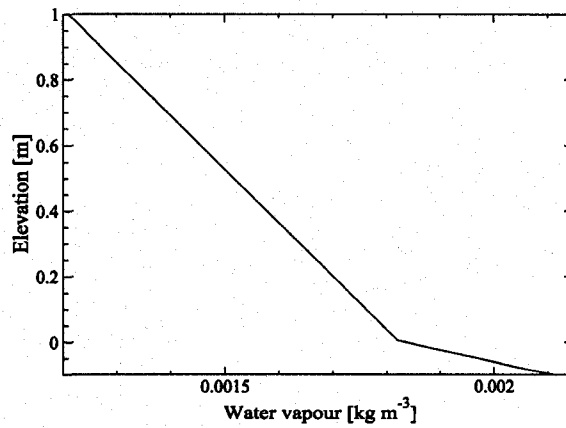


Figure 3.15: Water vapour amount along a line at the middle of the domain. Case: no wind,  $T=240\text{ K}$ ,  $P=800\text{ Pa}$ , 10 cm thick porous regolith.

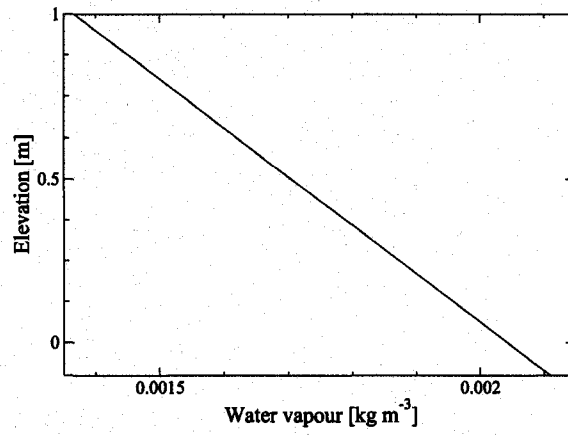


Figure 3.16: Water vapour amount along a line at the middle of the domain. Case: no wind,  $T=240$  K,  $P=800$  Pa, 10 cm thick fluid “regolith”.

### 3.1.1 Effect of Wind Velocity and Regolith Depth

Subject to laminar winds, the first simulation was at  $T=263$  K,  $P=600$  Pa with a regolith depth of 5 cm. The main fluid in the domain is constant property  $\text{CO}_2$  gas evaluated at the associated temperature and pressure.

As described in Table 3.1, for  $\text{CO}_2$  gas at 263 K and 600 Pa, the fluid properties were:

$\rho_{\text{CO}_2} = 0.012076 \text{ kg m}^{-3}$ ,  $C_P = 842.183 \text{ J kg}^{-1} \text{ K}^{-1}$ ,  $\mu_{\text{CO}_2} = 135.09 \times 10^{-7} \text{ Pa s}$ ,  $\beta = 0.0038 \text{ K}^{-1}$  and  $k_{\text{CO}_2} = 0.01339 \text{ W m}^{-1} \text{ K}^{-1}$ . The diffusivity was set to  $D_{wc}=2.6316 \times 10^{-3} \text{ m}^2 \text{ s}^{-1}$  and for the regolith, the effective porosity of 0.19 was selected.

From Fig. 3.17, which shows the velocity magnitude on a side view along the wind direction, it is evident that when the laminar model is used, the computed velocity profile is almost uniform along the  $x$ -axis and differs minimally from the inlet profile. Thus any effect on the water vapour flux due to the winds can be directly associated with the 1-D inlet PBL profile. Also from this figure, it is clear that velocity throughout the regolith is negligible except at locations very close to the surface.

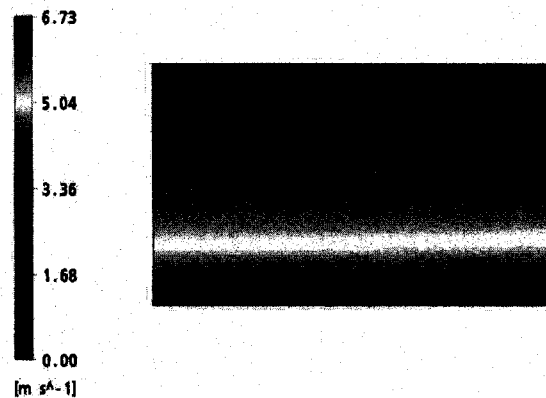


Figure 3.17: Velocity magnitude profile on a plane at the middle of the domain along the wind direction. Case:  $10 \text{ m s}^{-1}$  free stream wind,  $T=263$  K,  $P=600$  Pa, 5 cm thick regolith.

In Fig. 3.18, the water vapour contours are shown. Water vapour is clearly transported with the momentum, forming a concentration boundary layer above the surface.

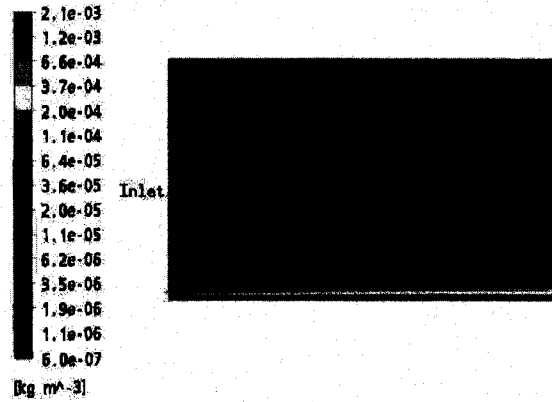


Figure 3.18: Water vapour logarithmic contours on a plane at the middle of the domain along the wind direction. Case: 10 m s<sup>-1</sup> free stream wind, T=263 K, P=800 Pa, 5 cm thick regolith.

For comparisons, the average surface integral<sup>1</sup> of water concentration ( $\overline{\rho_w^0}$ ) at a horizontal plane 5 mm above the surface was calculated. Interestingly, it was seen that this amount decreases when compared to the base case (case-1). The calculated values of water vapour at this plane are 1.93 g m<sup>-3</sup> for case-1 (pure diffusion) and 1.39 g m<sup>-3</sup> for the slowest wind case of 0.5 m s<sup>-1</sup>.

Recalling that the inlet air is relatively dry, water vapour near the surface decreases as the wind velocity increases due to a higher convective transport, which creates a higher water vapour gradient at the surface (Fig. 3.19).

Since the water vapour concentration near the surface and in the regolith is greatly affected by winds, the water vapour gradient and thus the water vapour net flux,  $\left(\frac{\partial \rho_w}{\partial z}\right)_{z_s}$ , in the regolith is also influenced. This is best verified by calculating the surface integral average of the water vapour gradient on a plane at 1 mm beneath the surface, due to the fact that the Control Volume approach and the discontinuity of material properties make the flux estimate at the interface less accurate. This amount increases when wind is present. For example, this vertical gradient, due to the enhanced convection mentioned above, increases

<sup>1</sup>Average surface integral is defined as :

$$\overline{\varphi} = \frac{1}{A_s} \int_{A_s} \varphi dA_s \quad (3.7)$$



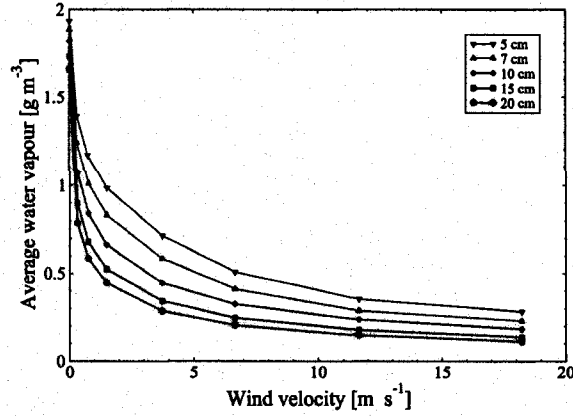


Figure 3.19: Average water vapour concentration versus laminar wind velocity and regolith depth. In the domain,  $T=263$  K and  $P=600$  Pa.

almost four times from  $3.53 \text{ g m}^{-4}$  to  $13.89 \text{ g m}^{-4}$  for the case of  $0.5 \text{ m s}^{-1}$  wind, when compared to case-1. The average net water flux can simply be calculated as,

$$\bar{J} = D_{eff} \left( \frac{\partial \rho_w}{\partial z} \right)_{z_s} \quad (3.8)$$

The water vapour flux values for all laminar wind cases can be seen in Fig. 3.20. Due to the increase in the regolith vapour density gradient, the flux increases when wind is present and when comparing the cases of the  $0.5 \text{ m s}^{-1}$  wind with no wind, there is an increase from  $1.77 \text{ mg m}^{-2} \text{ s}^{-1}$  to  $6.95 \text{ mg m}^{-2} \text{ s}^{-1}$ . Subject to laminar winds, the change of water vapour flux with wind speed is considerable. Especially at lower wind speeds, when the transition is occurring from pure diffusion (case-1) to a convection enhanced transport regime. At higher wind speeds, the effect of speed variation in the net flux tends to diminish (Fig. 3.19 and Fig. 3.20).

Moreover, at the same wind velocity, the flux changes considerably due to different regolith depths. That is, as the regolith above ice becomes thicker, both quantities of near surface water vapour and net vapour flux to the atmosphere decrease. This is mainly because the vapour flux is in large part controlled by the diffusion within the regolith, which is a function of the regolith depth. As the regolith thickness increases, the sensitivity of the flux to the change in wind velocity decreases.

The change in the regolith thickness does not have a linear effect on these quantities (Fig. 3.21), thus the simple Fick's law of diffusion is not valid when the water vapour transport is subject to surface flows.

These results clearly show the significant effects of horizontal winds and regolith depth on the near surface water concentration and water vapour flux from the regolith.

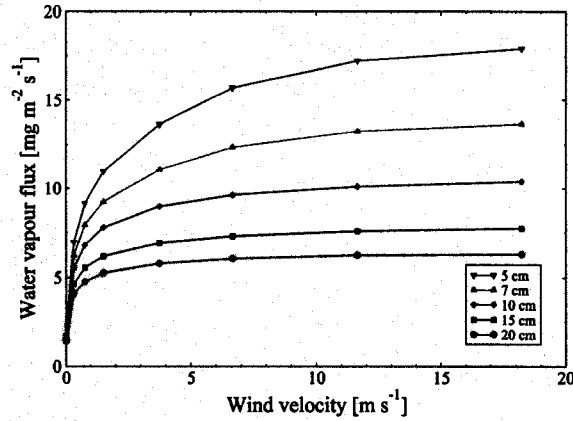


Figure 3.20: Average water vapour flux versus laminar wind velocity and regolith depth. In the domain,  $T=263$  K and  $P=600$  Pa.

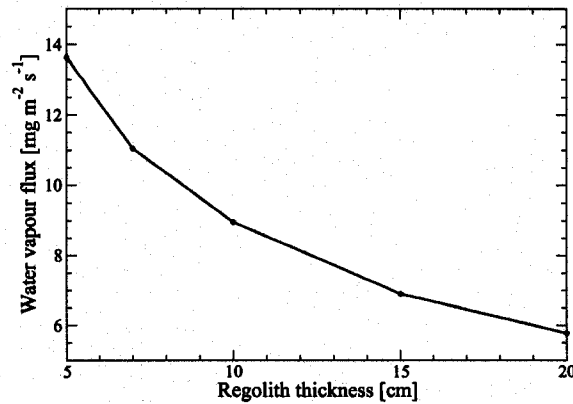


Figure 3.21: Average water vapour flux versus the regolith thickness. In the domain,  $T=263$  K,  $P=600$  Pa and the turbulent wind velocity is  $5$  m s<sup>-1</sup>.

### 3.1.2 Effect of Pressure

All previous cases were simulated at  $P=600$  Pa and  $T=263$  K. The effect of pressure was observed by increasing the domain pressure from 600 Pa to 900 Pa and the results were

studied similarly to previous cases. It should be noted that the effects of such increase in pressure was barely noticeable for the near surface average water concentration. This is due to the fact that change in pressure only slightly changes the air density, but other transport properties and the water vapour density source at the ice-table remain unaffected. However, an increase in pressure decreased the vapour net flux to the atmosphere (Figs. 3.22 and 3.23) significantly. This is mainly due to the fact that at a lower pressure (and thus lower density), the diffusivity of water in CO<sub>2</sub> is higher.

Moreover, when two cases with the same regolith thickness are subject to an identical wind velocity, the difference in the flux is larger at higher wind speeds.

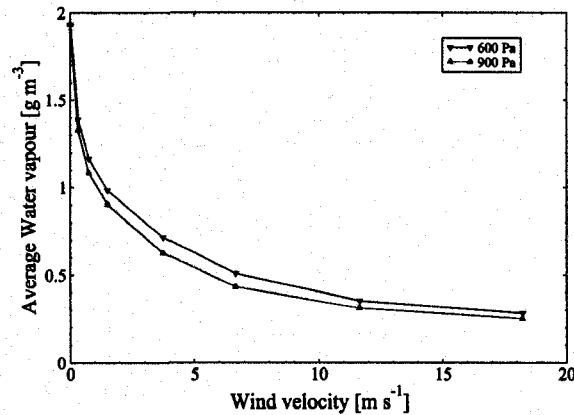


Figure 3.22: Average water vapour concentration versus laminar wind velocity and domain pressure. In the domain,  $T=263$  K and the regolith depth is 5 cm.

### 3.1.3 Effect of Temperature

Change in the domain temperature also has interesting effects on water vapour transport. As seen in Fig. 3.25, when the domain temperature is raised from  $T=253$  K to  $T=263$  K at  $P=600$  Pa, the average water vapour concentration above the surface increases to more than twice the amount (Fig. 3.25). The main reason for this increase is the increase in the water vapour source from the sub-regolith ice. When temperature increases, the water ice saturation pressure increases, which leads to a higher vapour concentration, for example  $\rho_{wv}^{ice}=2.11$  g m<sup>-3</sup> at  $T=263$  K and  $\rho_{wv}^{ice}=0.87$  g m<sup>-3</sup> at  $T=253$  K.

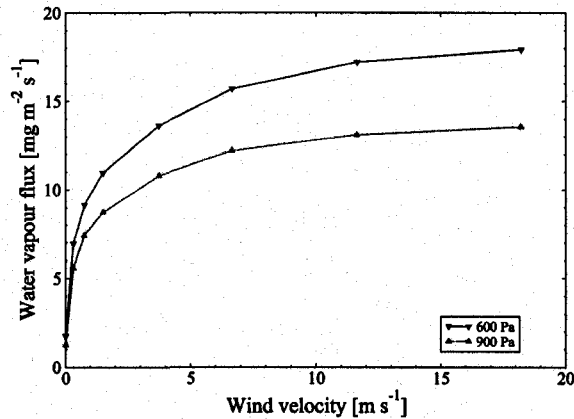


Figure 3.23: Average water vapour flux versus laminar wind velocity and domain pressure. In the domain,  $T=263$  K and the regolith depth is 5 cm.

Likewise, the average water vapour flux from the regolith increases significantly (almost three times) when temperature is increased (Fig. 3.27). The main parameter associated with an increase in the flux is the diffusivity, which generally increases with temperature. Both the water vapour density and the net flux still retain their trend as in other cases when subject to winds (Figs. 3.25 and 3.27) and the effect of different regolith depths is the same as when  $T=263$  K.

It should be noted that the real conditions on the Martian surface are not expected to be isothermal at any point in time. But the isothermal simulations conducted here are meant to quantify the effect of winds on the mass transport at a given temperature level, independent from the thermally driven transport processes.

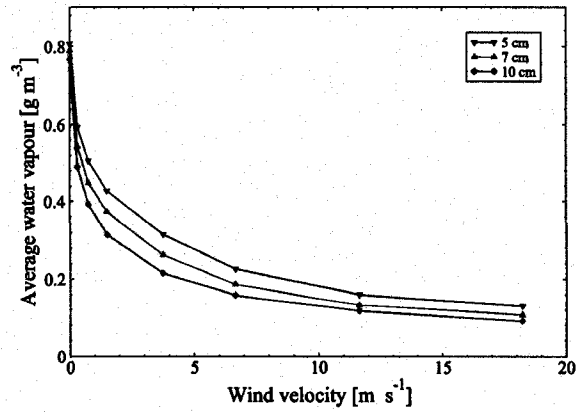


Figure 3.24: Average water vapour concentration versus laminar wind velocity and regolith depth. In the domain,  $T=253$  K and  $P=600$  Pa.

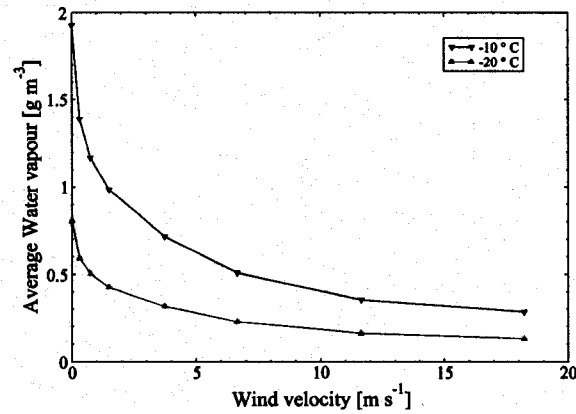


Figure 3.25: Average water vapour concentration versus laminar wind velocity and domain temperature. Regolith depth is 5 cm.

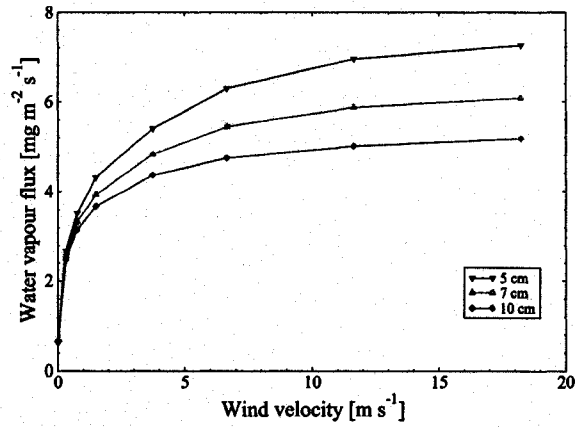


Figure 3.26: Average water vapour flux versus laminar wind velocity and regolith depth. In the domain,  $T=253$  K and  $P=600$  Pa.

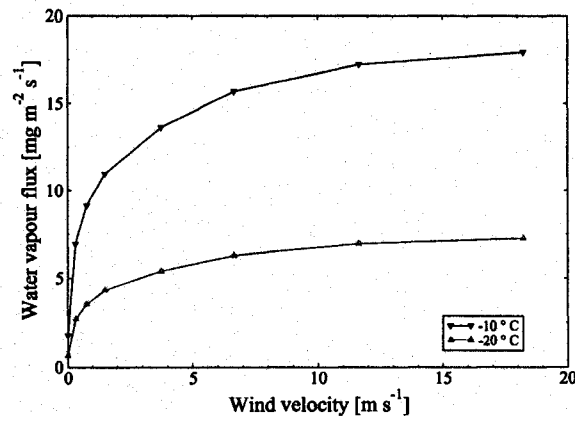


Figure 3.27: Average water vapour flux versus laminar wind velocity and domain temperature. Regolith depth is 5 cm.

### 3.1.4 Laminar Assumption versus the k- $\epsilon$ Turbulence Model

Since the wind profiles, which were used as the inlet boundary condition, were obtained from a 1-D turbulent planetary boundary layer model, a turbulence model may be used to capture the near surface turbulence effects. The k- $\epsilon$  model for turbulence is proven to overestimate the turbulence effects at transition regimes and at low turbulence levels, therefore it can be used as an upper limit for the estimation of the near surface turbulence.

For this purpose, a set of simulations described in the previous section were repeated with the k- $\epsilon$  model. As an extra boundary condition for this model, the turbulence intensity was prescribed at the inlet, which was also obtained from the 1-D Martian Planetary Boundary Layer dynamics model from Taylor et al. [2007].

Intensity is calculated using the velocity magnitude and turbulence kinetic energy at each point. Turbulence intensity,  $I_t$ , is a non-dimensional parameter that is defined as,

$$I_t = \frac{\overline{u'}}{\overline{U}} \quad (3.9)$$

where  $\overline{u'}$  is the root mean square of the turbulent velocity fluctuations,

$$\overline{u'} = \sqrt{\frac{(u_x'^2 + u_y'^2 + u_z'^2)}{3}} \quad (3.10)$$

and since turbulent kinetic energy (TKE) is defined as,

$$TKE = \sqrt{\frac{(u_x'^2 + u_y'^2 + u_z'^2)}{2}} \quad (3.11)$$

and  $\overline{U}_m$  is the Reynolds averaged mean velocity defined as,

$$\overline{U}_m = \sqrt{\frac{(U_{m_x}^2 + U_{m_y}^2 + U_{m_z}^2)}{3}} \quad (3.12)$$

then,

$$I_t = \frac{\sqrt{\frac{2}{3}TKE}}{\bar{U}_m} \quad (3.13)$$

As a result, the velocity magnitude in the domain can be seen from Fig. 3.28, which was a simulation case at  $T=263$  K,  $P=600$  Pa with a regolith depth of 5 cm and a  $20 \text{ m s}^{-1}$  free stream wind. With the turbulent model, the prescribed inlet velocity profile changes through the domain unlike the laminar model. Surprisingly, the horizontal velocity gradient at the regolith surface is lower than the laminar model, which is not expected from a turbulent flow. Also from Fig. 3.29, it is seen that the vapour flux for the turbulent model is lower than laminar model, which is again not expected from a turbulent regime. Similar to the heat transfer from a surface, mass transfer is also enhanced when subject to a turbulent flow. Therefore, after exhaustive testing of cases with and without the porous region, the reason for these results seems to be the inability of the CFX solver to resolve a turbulent flow over a porous domain.

Furthermore, from Fig. 3.30 and Fig. 3.31, it is evident that when a turbulent model is used in CFX, the values of water vapour density and flux do not change with the wind speed and there is no trend toward the pure diffusion case of  $0 \text{ m s}^{-1}$ . This is probably due to the errors of using this model for a laminar and transition regime. Since the results for the turbulence model are not accurate, they will not be further analyzed. Beside  $k-\epsilon$ , other turbulence models were tested but they did not converge for the case of flow over a porous medium.



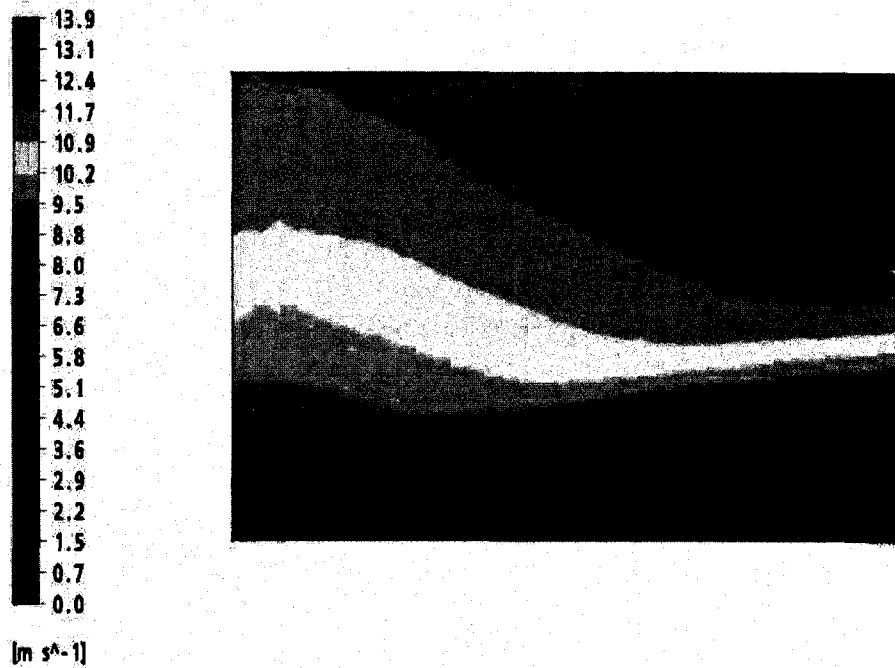


Figure 3.28: Velocity magnitude profile on a plane at the middle of the domain along the wind direction. Case:  $20 \text{ m s}^{-1}$  free stream wind,  $T=263 \text{ K}$ ,  $P=600 \text{ Pa}$ ,  $5 \text{ cm}$  thick regolith.

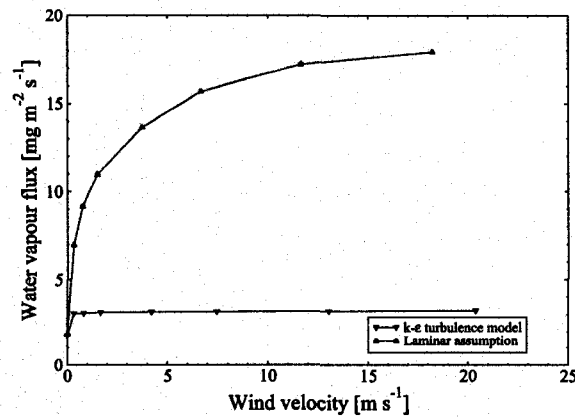


Figure 3.29: Average water vapour flux versus wind velocity. Comparison of the k- $\epsilon$  model with a laminar assumption.  $T=263 \text{ K}$  and  $P=600 \text{ Pa}$ .

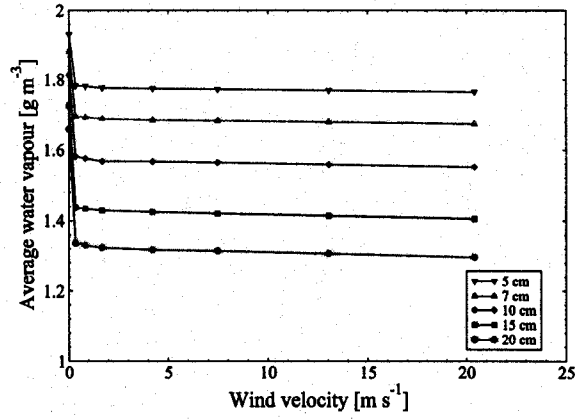


Figure 3.30: Average water vapour concentration versus turbulent wind velocity and regolith depth.  $T=263 \text{ K}$  and  $P=600 \text{ Pa}$ .

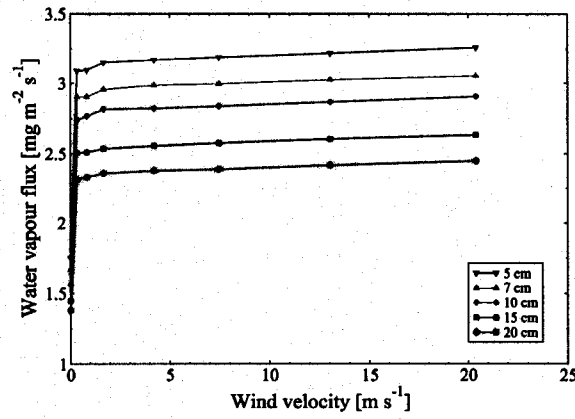


Figure 3.31: Average water vapour flux versus turbulent wind velocity and regolith depth.  $T=263 \text{ K}$  and  $P=600 \text{ Pa}$ .

### 3.1.5 The Special Sherwood Number for Horizontal Winds

As discussed in Chapter 2, the special mean Sherwood number ( $\overline{Sh}^*$ ) can be calculated by having the net vapour flux from the regolith, water vapour concentration at two arbitrary points and the distance between them. For this purpose, the mean water vapour gradient ( $\left(\frac{\partial \rho_w}{\partial z}\right)_{z_s}$ ) is calculated at a depth of 1 mm under the surface. The gradient has to be calculated on one side of the interface, because the change in properties between the porous region and the pure fluid region causes a discontinuity in the gradient. Mean water vapour values for the two arbitrary points were calculated at 5 mm above the surface ( $\overline{\rho_w^0}$ ) and at the regolith-ice interface (bottom boundary), where water concentration is assumed to be equal to its saturation value  $\overline{\rho_w^{ice}}$ . The distance between these two points is named L (L=regolith depth+5 mm), thus  $\overline{Sh}^*$  can be calculated for each case:

$$\overline{Sh}^* = \frac{D_{\text{eff}} \left(\frac{\partial \rho_w}{\partial z}\right)_{z_s}}{D_{\text{eff}} \frac{\overline{\rho_w^{ice}} - \overline{\rho_w^0}}{\Delta L}} \quad (3.14)$$

$\overline{Sh}^*$  also indicates the deviation of the real water vapour transport phenomena from a linear diffusion assumption. The values of  $\overline{Sh}^*$  are calculated for all the discussed cases with the laminar model, which can be seen in the following figures.

From Fig. 3.32, it is evident that for wind velocities higher than  $2 \text{ m s}^{-1}$ , an increase in wind speed does not significantly affect  $\overline{Sh}^*$ . However, the effect of regolith thickness is considerable, i.e. as thicknesses increases,  $\overline{Sh}^*$  increases too and it is by far the most relevant parameter for the determination of  $\overline{Sh}^*$ .

Referring to Fig. 3.33, at a lower pressure, the  $\overline{Sh}^*$  values were slightly higher for all wind speeds. At a lower temperature in the domain, the  $\overline{Sh}^*$  values decreased uniformly for the laminar model (Fig. 3.34).

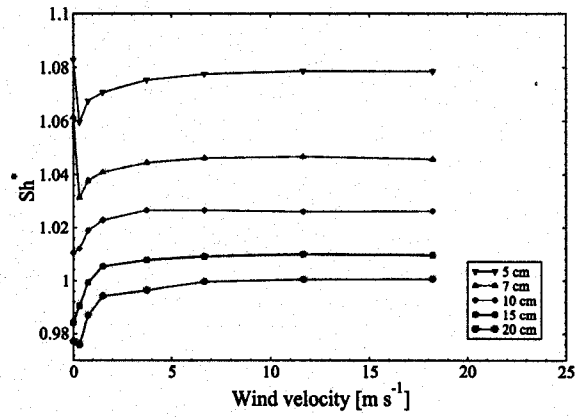


Figure 3.32: Special Sherwood number versus laminar wind velocity and regolith depth.  $T=263$  K and  $P=600$  Pa.

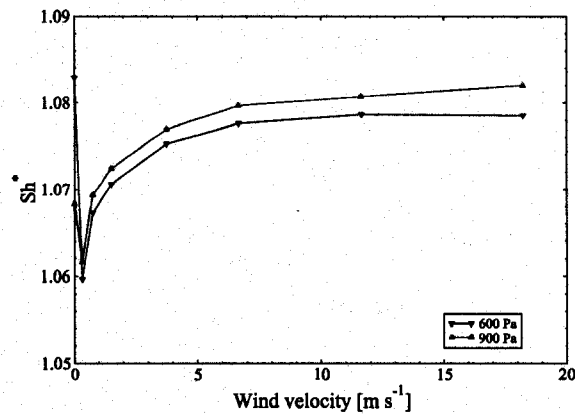


Figure 3.33: Special Sherwood number versus laminar wind velocity and domain pressure. In the domain,  $T=263$  K and the regolith depth is 5 cm.

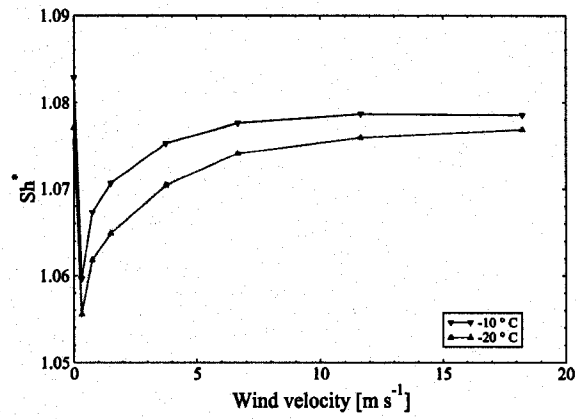


Figure 3.34: Special Sherwood number versus laminar wind velocity and domain temperature. In the domain,  $P=600$  Pa and the regolith depth is 5 cm.

### 3.1.6 Grid and Domain Independence Analysis

The grid independence of the numerical simulations, as discussed in Chapter 2, is verified by calculating an arbitrary variable (which has relevance in the analysis) at different grid levels and showing that the result does not change significantly with further grid refinement, or that the convergence is monotonic. For the wind simulations, the surface integral of water vapour density at a horizontal plane 5 mm above the surface was calculated at four grid levels ( $h_1$  to  $h_4$ ), with a constant arbitrary ratio of 1.2 for the cubic root of the total node number. The results are plotted in Fig. 3.35 and provided in Table. 3.3.

H	$h_1$	$h_2$	$h_3$	$h_4$
N	66519	112831	196706	335503
$N^{\frac{1}{3}}$	40.5	48.3	58	69.5
$\bar{\rho}_{wv}^{h_i}$	0.00642	0.00652	0.00655	0.00659

Table 3.3: Surface integral of water vapour density at a horizontal plane 5 mm above the surface, calculated at four grid levels.

Where N is the number of nodes,  $N^{\frac{1}{3}}$  is the grid level and  $\bar{\rho}_{wv}^{h_i}$  is the average surface integral of water vapour density at grid level  $i$ . Selecting the last three grid levels and according to the procedure in 2.3.7, the order of the scheme is estimated to be  $p=1.58$ . Since the numerical scheme is second order, if  $1.5 < p < 2.5$  (which confirms that the code is behaving as a second order), then the convergence is monotonic, and the Richardson extrapolation will yield an accurate approximation to the exact solution of the differential equations.

In order to confirm the domain independence of the wind simulations, one case of the wind simulations was simulated in a longer domain (in the  $x$  direction). This was performed because, although the velocity and density profiles in the domain seem developed at the end of the domain, where the analyzed quantities are extracted, a question may be raised on what would be the change in solution if a longer domain was used? This question was answered by using a domain twice as long, keeping all other dimensions and the meshing procedure the same. When the case of a  $5 \text{ m s}^{-1}$  turbulent wind at  $T=263 \text{ K}$  and  $P=600 \text{ Pa}$  was simulated in the new 12 m long domain, it was realized that there is only a 5% error compared to a 6 m long domain, which is acceptable, given the uncertainties in our model.

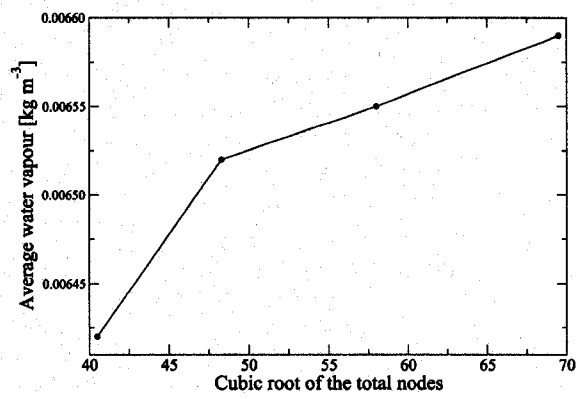


Figure 3.35: Surface integral values of water vapour at different grid levels.

## 3.2 Effect of Local Natural Convection on Water Vapour Transport

At the Phoenix landing site, a high net heat flux is received from the Sun at the surface, which could increase the surface temperature to more than 300 K. This significant temperature difference results in thermal buoyancy forces in the near surface atmosphere. These buoyant plumes continue to rise from the surface and grow, eventually forming mesoscale convective rolls in the lower near surface atmosphere. The effect of such mesoscale convective rolls in a local near surface region corresponds to horizontal winds with different velocities, which were discussed in the previous section. In this section, the initial evolution of local thermal plumes and the effect of local convective rolls and plumes on water vapour transport from the regolith are studied.

In order to evaluate the flow regime of the atmospheric flow at a local scale, the Rayleigh number for a local scale domain should be evaluated. On Mars ( $g_{Mars}=3.72 \text{ m s}^{-2}$ ) at the same temperature and pressure, assuming a 40 K temperature gradient between the surface and the atmosphere and a local scale characteristic length of 5 m,  $Gr \simeq 1.1 \times 10^5$  and  $Ra \simeq 1.4 \times 10^8$ . For buoyancy driven flows, as the Ra increases, the flow changes from a laminar to a fully turbulent regime. The transition Ra number, depends on the fluid properties and the geometry of the configuration but in general, given the same fluid properties and domain geometry, it decreases for a plate as its angle is changed from vertical to a horizontal position. In the case of a horizontal isothermal wall in water with  $Pr \simeq 6$ , the transition Rayleigh number is  $Ra \simeq 8.7 \times 10^8$  [Lloyd and Sparrow, 1970]. From experiments in the turbulent regime in the case of a hot plate with a cold fluid on top, their Nu correlation based on Ra is valid for  $Ra > 10^7$  [Lloyd and Moran, 1974]. For the local scale domain on Mars at the Phoenix lander site (used in this study for simulations), using the atmospheric properties explained before,  $Pr = 0.92$  and  $Ra \simeq 1.4 \times 10^8$  therefore the convective flow is in the transition regime.



## 3.3 Partial Theoretical Validation of the Numerical Model

### 3.3.1 One Dimensional Model Validation

One procedure to verify a three dimensional model that includes complex physics is to compare its results with a more simple model. In particular, one of the three dimensional transport equations, the heat equation, can be compared with a steady, one dimensional energy balance at the atmosphere-regolith interface. The physics of the one dimensional problem can be defined as:

Temperature at the surface rises due to solar irradiation heat flux, which can be calculated (described in Section 1.5). The surface heat flux is then conducted through the regolith and convected to the atmosphere, thus resulting in a constant surface temperature at steady state. Assuming that the bulk atmosphere temperature is 220 K, the water ice table temperature beneath a 0.1 m layer of regolith is 230 K and a  $175 \text{ W m}^{-2}$  irradiation to the surface ( $q_{sur}$ ), the surface temperature ( $T_s$ ) can be calculated using constant atmosphere and regolith properties (from the previous sections). At 240 K and 800 Pa,  $\rho_{atm}=0.01764 \text{ kg m}^{-3}$ ,  $\mu_{atm}=1.2487 \times 10^{-5} \text{ Pa s}$ ,  $k_{atm}=0.01183 \text{ W m}^{-1} \text{ K}^{-1}$ ,  $C_p^{atm}=829.82 \text{ J kg}^{-1} \text{ K}^{-1}$ ,  $\beta=0.004166 \text{ K}^{-1}$  is the thermal expansivity of the air and  $k_{reg}=0.2 \text{ W m}^{-1} \text{ K}^{-1}$ .

The convective 1-D rate of heat transfer from a surface to a fluid can be written as,

$$\dot{q}'' = h(T_{sur} - T_{\infty}) \quad (3.15)$$

where  $T_{\infty}$  is the fluid bulk temperature and the non-dimensional Nusselt number is defined as,

$$\text{Nu} = \frac{hL}{k} \quad (3.16)$$

$k$  is the thermal conductivity of the fluid and  $L$  is a characteristic length. Depending on the physics of the fluid flow and heat transfer, the Nusselt number can be a function of the Prandtl number and Grashof number (or only a function of the Rayleigh number) in the case of natural convection, or Prandtl number and Reynolds number in case of forced convection.

$$\text{Pr} = \frac{c_p \mu}{k} \quad (3.17)$$

The Prandtl number changes very little with pressure and it is mainly temperature dependent, so the Pr on Mars has a similar value to that of Earth at the same temperatures.

The net heat load at the regolith surface due to solar irradiation can be written as,

$$q_{sur} = q_{reg} + q_{atm} \quad (3.18)$$

$$q_{atm} = \bar{h}_{atm} (T_s - T_{atm}) \quad (3.19)$$

$$q_{reg} = \frac{k_{reg}}{L} (T_s - T_{ice}) \quad (3.20)$$

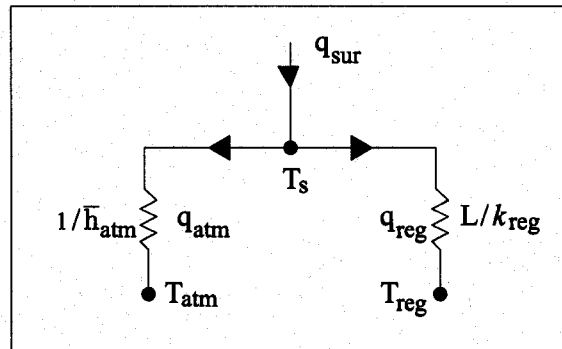


Figure 3.36: 1-D resistance diagram of a heat transfer model from the regolith surface to the atmosphere and the ice-table.

$\bar{h}_{atm}$  can be obtained from various  $\overline{\text{Nu}}_{atm}$  correlations for natural convection in the case of a cold fluid on top of a heated horizontal plate.

$$\overline{\text{Nu}}_{atm} = \frac{\bar{h}_{atm} H}{k_{atm}} \quad (3.21)$$

In the case of natural convection, correlations are mainly based on the Rayleigh number (Ra),

$$\text{Ra} = \frac{g \beta \Delta T H^3}{\nu \alpha} \quad (3.22)$$

At the Mars north pole conditions,  $g=3.69 \text{ m s}^{-2}$  is the Martian gravity,  $\Delta T = 40 \text{ K}$  is the estimated temperature difference driving the natural convection,  $H=5 \text{ m}$  is the characteristic length in the atmosphere in our domain scale,  $\nu=7.0788 \times 10^{-6} \text{ m}^2 \text{ s}^{-1}$  is the kinematic viscosity and  $\alpha=9.08 \times 10^{-4} \text{ m}^2 \text{ s}^{-1}$  is the thermal diffusivity (calculated from the mentioned constant properties). Using these values,  $Ra \simeq 1.34 \times 10^8$ . From Incropera et al. [2007], for  $10^7 \lesssim Ra \lesssim 10^{11}$ ,

$$\overline{Nu} = 0.15 Ra^{\frac{1}{3}} \quad (3.23)$$

therefore in this case,  $h_{atm}=0.18 \text{ W m}^{-2} \text{ K}^{-1}$ . It should be mentioned that in a more recent study, Leong et al. [1998] focused on natural convection in cubical cavities and suggested the following correlation for  $10^6 \lesssim Ra \lesssim 10^8$ ,

$$\overline{Nu} = 0.1194 Ra^{0.3021} \quad (3.24)$$

In this case,  $h_{atm}=0.08 \text{ W m}^{-2} \text{ K}^{-1}$ , resulting in a higher surface temperature by couple of degrees of Kelvin. With the surface heat transfer coefficient, the surface temperature can now be calculated,  $T_s=314 \text{ K}$ . From the  $175 \text{ W m}^{-2}$  radiant heat flux arriving at the surface,  $7.5 \text{ W m}^{-2}$  is transferred to the atmosphere and  $167.5 \text{ W m}^{-2}$  is transferred to the regolith, highlighting the importance of an accurate thermal conductivity selection for the regolith. The surface temperature obtained from this simple 1-D model can be compared with the 3-D simulation result<sup>2</sup> in Section 4.3.

### 3.3.2 An Informative Larger Scale Two Dimensional Simulation of the Atmosphere

In order to gain insight into the flow structure at the landing site, natural convection in the larger scale atmosphere was simulated, which was not bounded by local scales. The 2-D domain for this simulation is  $50 \times 50 \text{ m}$  above the surface and within the near surface atmospheric layer. Such larger scale simulation provided initial flow structure and velocity information, which assisted in modelling the local scale flow at the Lander's site. The domain was purely fluid and did not include the porous part. The surface temperature was set to  $300 \text{ K}$  and at  $50 \text{ m}$ , at the top of the domain, temperature was set to  $220 \text{ K}$ . The vertical sides of the domain are set to symmetry. Using a second order backward Euler

<sup>2</sup>The difference from the 3-D model is  $\sim 4\%$ .

transient scheme for time discretization and having at least one node at  $5 \mu\text{m}$  from the surface, transient natural convection was simulated in this domain using both a laminar regime assumption and several turbulence models. The laminar simulation converged and the results show the transient thermal plume generation. Among the turbulence models, only the  $k-\epsilon$  model converged. The Omega, SSG and BSL Reynolds Stress models failed to achieve convergence. When the BSL and  $k-\omega$  models were used, thermal plumes were not generated in the domain at all.

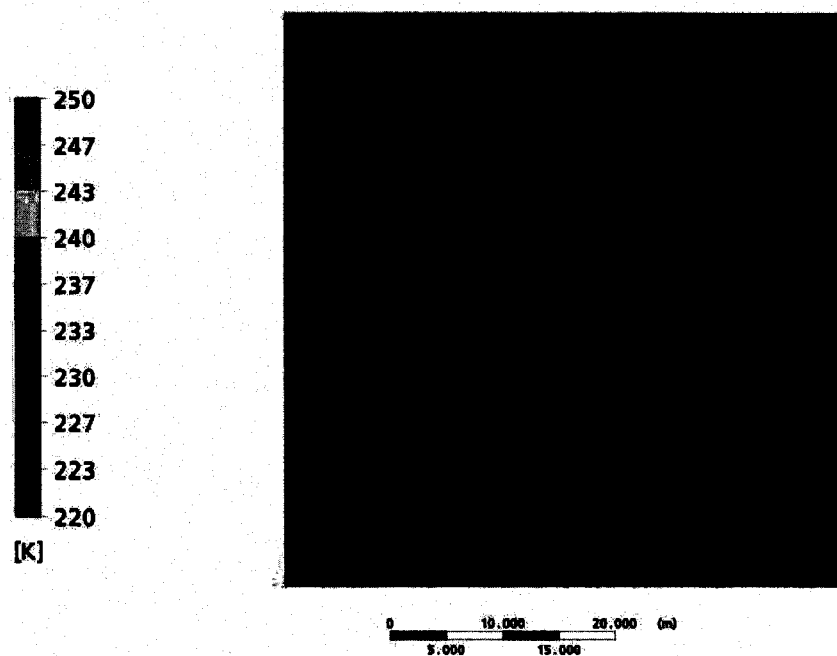


Figure 3.37: Thermal plumes rising in the near surface atmosphere after 60 s of solar irradiation.

For both the  $k-\epsilon$  and laminar simulations (laminar case shown in Fig. 3.37), it is evident that after a few minutes, the thermal plumes that were generated at the heated Martian surface evolved and progressively ascended above the surface, while transporting up the heat. It is also evident that the plumes extend considerably beyond the few meters scale of a local scale domain. This suggests that when modelling local natural convection above the surface, simulating a local domain is not sufficient to capture the complete physics of atmospheric natural convection. A local domain can be used to simulate the initial plume generation stages and the subsequent local scale convective rolls. Additionally, the larger

scale effects should be added to the analysis of a local scale natural convection by treating them as horizontal winds in a local domain. From Fig. 3.38 convective rolls can be seen that have velocities higher than  $1 \text{ m s}^{-1}$ , with their lower parts having the effect of a horizontal wind for a local spot.

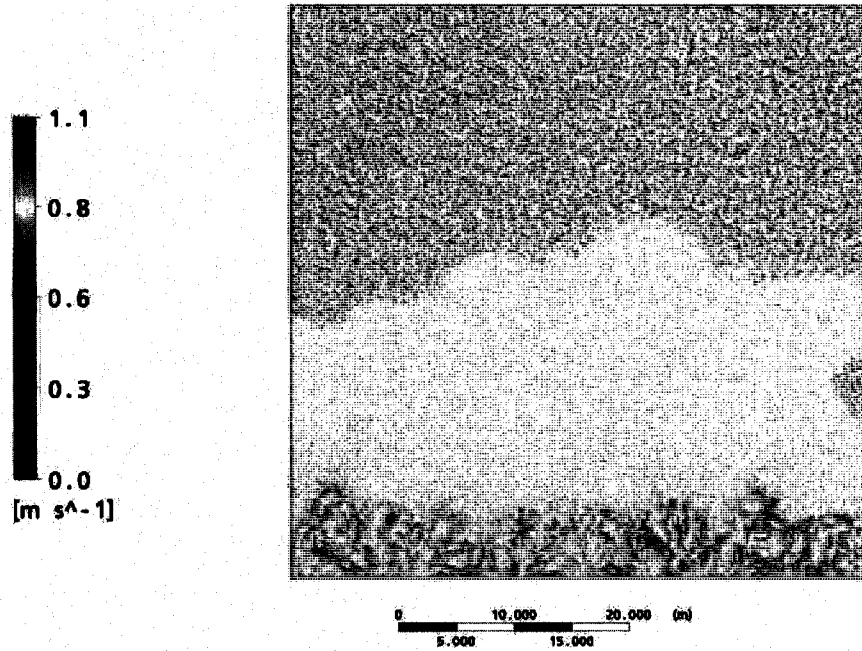


Figure 3.38: Velocity vectors in the near surface atmosphere after 170 s of solar irradiation.

### 3.3.3 Natural Convection Model Validation

Based on the Rayleigh number at the Lander's site, the flow regime is transitional. In this case, the numerical turbulence models may not correctly resolve the flow regime. Therefore, both a laminar assumption and several turbulence models were compared with benchmark experimental results from Ampofo and Karayiannis [2003] and Leong et al. [1998].

In the experiments of Ampofo and Karayiannis [2003], turbulent natural convection was studied in a rectangular cavity with a constant temperature hot and cold vertical walls at the sides (Fig. 3.39).

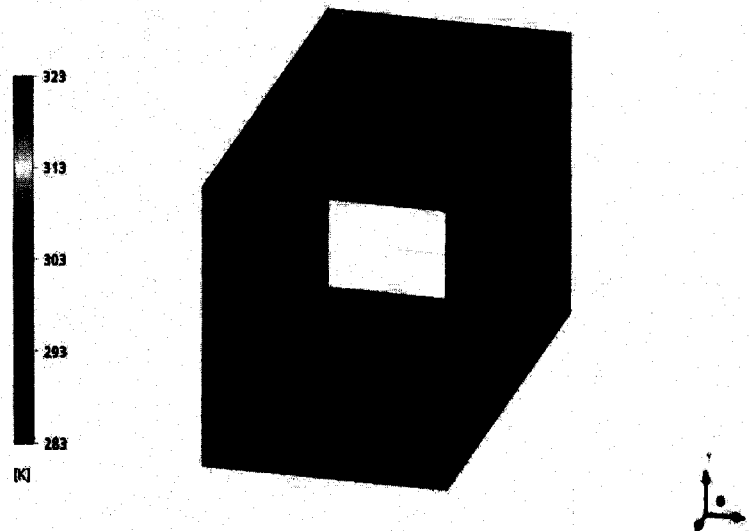


Figure 3.39: The numerical domain of the experimental configuration of Ampofo and Karayiannis [2003].

The cavity was 0.75 m high, 0.75 m wide and 1.5 m long. The hot and cold walls were controlled at  $50 \pm 0.15$  °C and  $10 \pm 0.15$  °C, respectively. The cavity was filled with air ( $Pr=0.71$ ), thus resulting in  $Ra=1.58 \times 10^9$  for the experimental configuration, which is close to the  $Ra$  expected at the landing site. This experiment was simulated using the same geometry, boundary conditions and domain fluid with several turbulence models. Additionally, the same type of experiment was simulated with two other conditions, one consisting of  $CO_2$  at  $P=1$  atm and  $T=273.15$  K with Earth's gravity and the other  $CO_2$  at  $P=800$  Pa and  $T=273.15$  K with Mars' gravity. For these simulations, the temperature

profile and the local Nusselt number along a horizontal line from the mid-height of the hot plate at the middle of the cavity's length to the mid-height of the cold plate were compared with the experimental results. For example when using the  $k-\omega$  turbulence model, the temperature profile across the cavity can be seen in Fig. 3.40. For this validation, the closest results to the experiments were obtained with the  $k-\omega$  turbulence model. Using a laminar assumption, simulation results were also close to the experiments with higher deviations at the walls. In fact, the laminar models performed best in comparison with the experimental profile of Nu (Fig. 3.41).

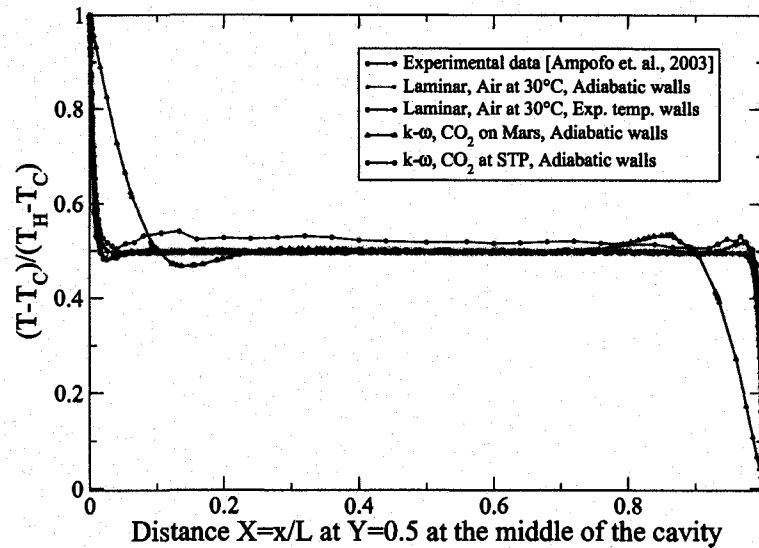


Figure 3.40: Comparison of temperature profiles along  $X=x/L$  at mid length and height across the cavity, between the hot and cold walls.

In the experiments of Leong et al. [1998], natural convection was studied in a cubic cavity. The cavity had equal length sides of 127 mm. Two opposite facing sides were maintained at constant temperatures of 307 K and 300 K. The experiments were performed with different orientations of the cube, allowing the temperature controlled plates to be horizontal, vertical and at  $45^\circ$  with the horizon. The experiments were carried out with different Ra numbers, which were controlled by altering the pressure of the experimental environment. The side plates between the two controlled temperature plates were prepared in a fashion to have a linear temperature profile from the warmer plate to the colder one. This experiment was simulated with the configuration being at  $Ra=1.01 \times 10^8$ , using both vertical and horizontal temperature controlled plates. For simulations with a laminar assumption and

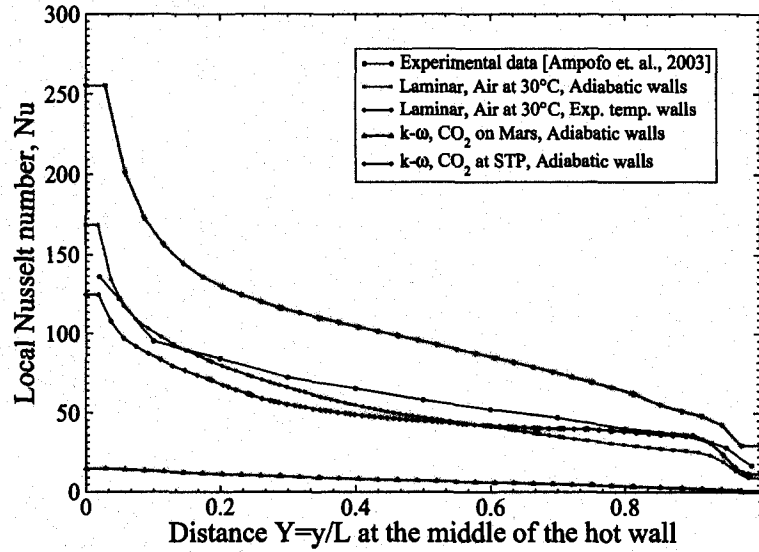


Figure 3.41: Comparison of the local Nusselt number along  $Y=y/L$  at the middle of the hot wall.

several turbulence models, the average Nusslet number ( $\overline{Nu}$ ) at the cold plate was calculated and compared to the correlations for  $\overline{Nu}$  provided by Leong et al. [1998]. For vertical temperature controlled plates,

$$\overline{Nu} = 0.08461Ra^{0.3125} \quad \text{for} \quad 10^4 \leq Ra \leq 10^8 \quad (3.25)$$

and for horizontal temperature controlled plates,

$$\overline{Nu} = 0.119Ra^{0.3021} \quad \text{for} \quad 10^5 \leq Ra \leq 10^8 \quad (3.26)$$

In Table. 3.4, the simulation results for the flow models are compared with the experimental data. When comparing the average  $\overline{Nu}$  on the cold wall for the simulations with the experiments, it is evident that, except for the  $k-\epsilon$  model, other turbulence models and also the laminar simulation showed reasonable agreement. It should be mentioned that the laminar model provided the closest result to the experiment data (5% difference).

From the benchmark experiments, it was observed that the  $k-\epsilon$  model does not predict the wall heat transfer and temperature profiles well enough. The laminar model agrees



Nu	k- $\epsilon$	k- $\omega$	$\omega$ -RSM	Laminar	Experiment
Horizontal wall	-	27.03	27.80	29.74	31.33
Vertical wall	1.77	23.79	23.53	-	26.89

Table 3.4: Comparison of the average Nusselt number at the cold wall for simulation flow models and the experimental result from Leong et al. [1998].

reasonably well with the experimental results. In all of these models, it is very important to have at least one node in the  $y^+ \lesssim 5$  region at the hot and cold walls.

### 3.3.4 Selection of a Proper Turbulence Model

The effects of natural convection on water vapour transport from the regolith to the atmosphere were studied in a domain with both a porous region and a pure fluid region. The shape of the domain is similar to the horizontal winds domain, a rectangular cube divided into two parts, a top part representing the atmosphere (fluid region) and a bottom part representing the regolith (porous region).

Initially, simulations were performed to determine whether turbulence models are needed and if so, which models would better resolve the flow field. For this purpose, a domain that is 6 m long and 3 m wide is used. The top atmosphere part is 3 m high and the bottom soil part is 10 cm deep. This cubic domain was discretized using unstructured mesh with a total of approximately 600,000 nodes. A local refinement was applied using inflated layers at the atmosphere-soil interface with a first layer thickness of 5  $\mu\text{m}$ . The fluid properties and the boundary conditions are similar to the horizontal winds model (Section 3.1).

The primary fluid in the domain is constant property  $\text{CO}_2$  gas with density, viscosity, thermal conductivity and specific heat capacity calculated with the local Martian temperature and pressures,  $T=240$  K and  $P_{ref}=800$  Pa, respectively. Natural convection effects are included by using the Boussinesq approximation.

Since the flow regime is transient, the model was simulated with several cases of different turbulence models and a pure laminar flow case for comparison. Turbulence models used in the simulation were the standard k- $\epsilon$ , the k- $\omega$ , the SSG-RSM, the BSL-RSM, the LRR-RSM and the  $\omega$ -RSM. For the domain, boundary conditions had to be considered carefully

to avoid non-physical results. At the top surface of the atmosphere and the bottom of the regolith, a free slip wall boundary with prescribed water vapour concentration is applied. A 100% relative humidity was assumed at the regolith bottom boundary, which corresponds to  $0.08523 \text{ g m}^{-3}$  at 230 K (ice table temperature), thus representing the saturation state at the top of the ice table. At the top domain boundary,  $\rho_{H_2O} \simeq 6 \times 10^{-7} \text{ kg m}^{-3}$  was prescribed.

A conservative flux interface boundary is used at the atmosphere-regolith interface with addition of a constant heat flux of  $250 \text{ W m}^{-2}$  in the regolith face boundary nodes. This heat flux simulates the heat source due to solar irradiation and is calculated especially for the Phoenix landing site during its mission, as explained in Chapter 1. The sides of the regolith region have a symmetry boundary condition. In the atmosphere region, boundary conditions at the vertical sides significantly influence the natural convection flow structure, hence it is more important to apply a boundary condition that better corresponds to the real physics. For this reason, both a length wise translational periodic boundary ( $X$  direction) and a symmetry condition for all the four sides can be used. The periodic boundary condition resembles an infinitely long domain, thus complete convective rolls in the middle and half rolls at the sides will be generated in the domain. If symmetry boundaries on the sides are used, the sides will have a wall effect which only allow for full convective roll generation in the domain. Consequently, these side walls affect and deform the convective rolls near to them.

Lastly, for the regolith, the effective volume porosity and the permeability is set to 0.3 and  $10^{-12} \text{ m}^2$  respectively, close to the preferable values described in previous sections.

The transient equations are solved with second order implicit scheme to reach a convergence goal of  $10^{-5}$  for the root mean square of the residuals.

Among the turbulence models, the SSG-RSM, the BSL-RSM, the LRR-RSM and the  $\omega$ -RSM failed to reach convergence. When the  $k$ - $\epsilon$  and the  $k$ - $\omega$  were used, plumes initially appeared in the domain, but did not develop into convective rolls. The velocity magnitude of the plumes decreased in time until ultimately, they were annihilated resulting in a quiescent domain. As in the horizontal wind cases, these problems seem to be associated with the inability of the CFX solver to resolve the natural convection motion on a porous domain

with the turbulence models.

However, the laminar model had a robust convergence and provided satisfactory results, which were expected from the benchmark cases. This simple model proved to be a good choice for simulating natural convection, when compared to the experimental results, discussed in the previous section. From the results, transient behavior of the velocity field, water vapour concentration and heat transport can be studied.

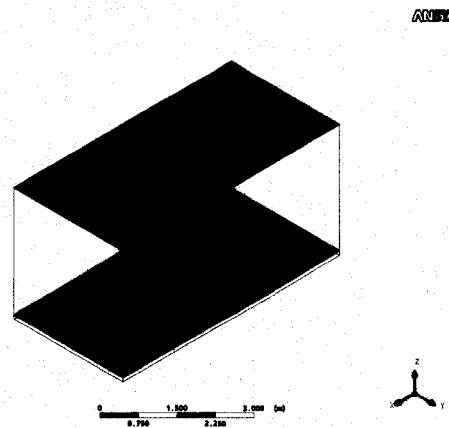


Figure 3.42: Numerical local domain for surface natural convection simulations.

From Fig. 3.43, it can be seen that after 12 s of solar irradiation on the surface, thermal plumes have ascended to a couple of meters high into the air. Temperature is transported with the convective motion of the fluid, which is evident from the velocity vectors in Fig. 3.44. This is compatible with Smith et al. [2004], where they reported a quick temperature rise near the surface and a rapid formation of a superadiabatic layer.

The velocity magnitude can reach up to a few meters per second at this time. Similarly, water vapour or any other trace volatile or light particle is transported with the fluid convection. In Fig. 3.45, the transport of water vapour concentration due to convection and diffusion can be observed. After 60 s, the initial thermal plumes have already developed into convective rolls in the domain. At this stage, the rolls are bound by the imposed boundary conditions, without which they would have continued to ascend higher into the atmosphere, creating mesoscale convective plumes. After 60 s, heat has been distributed more uniformly throughout the domain. Water vapour concentration has also mixed well in the domain,



Figure 3.43: Thermal plumes rising in the near surface atmosphere after 12 s of solar irradiation.

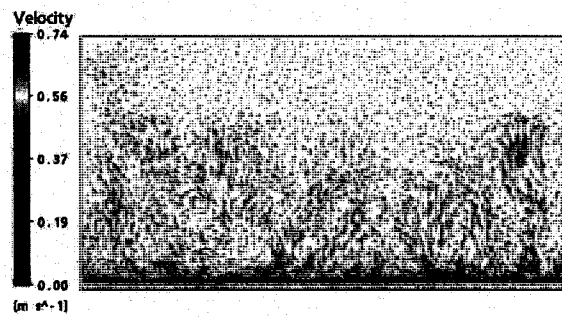


Figure 3.44: Velocity vectors in the near surface atmosphere after 12 s of solar irradiation.

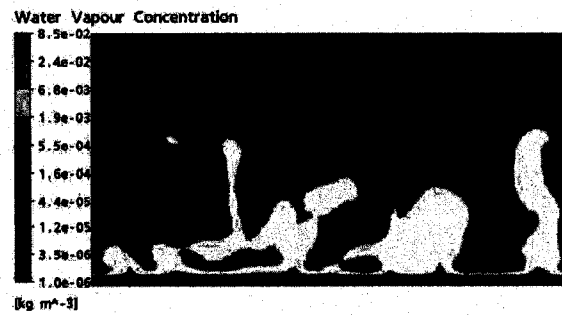


Figure 3.45: Water vapour concentration in the near surface atmosphere after 60 s of solar irradiation.

similar to the transport of heat. This significant mixing due to natural convection is better observed when compared to a case of temperature and water vapour transport due to pure diffusion (Fig. 3.46).



Figure 3.46: Logarithmic contours of water vapour concentration in the near surface atmosphere for the case of pure linear diffusion.

### 3.3.5 Case studies

To quantitatively study the effects of natural convection on water vapour transport from the regolith, average values of water vapour density at 5 mm above the surface, water flux at 1 mm beneath the surface and water vapour concentration in the atmospheric part of the domain were calculated for several cases with the regolith depth and solar irradiation to the surface (thus surface temperature) as variables. The results were then compared with a base case of an isothermal, pure diffusion for the same elapsed time.

In the previous section, it was mentioned that when the laminar assumption was used in the simulations, the local buoyancy flow was better resolved under Mars' transient convection flow regime. Thus for the parameter studies, only the laminar model was employed.

The regolith thickness varies between 5 cm and 10 cm and the heat load at the regolith surface is prescribed using the values  $10 \text{ W m}^{-2}$ ,  $35 \text{ W m}^{-2}$ ,  $75 \text{ W m}^{-2}$ . The effect of regolith depth and different surface temperatures are illustrated in Fig. 3.47 and Fig. 3.48.

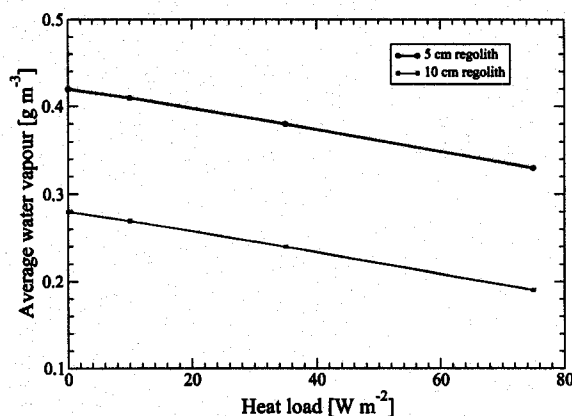


Figure 3.47: Average water vapour concentration on a plane at 5 mm above the surface versus heat source at the surface and the regolith depth.

Comparing to a case of pure diffusion without natural convection, after 15 s of a  $75 \text{ W m}^{-2}$  surface heat source, at 5 mm above the surface, average water vapour concentration decreased from  $0.56 \text{ g m}^{-3}$  to  $0.43 \text{ g m}^{-3}$  for a 5 cm thick regolith. At 1 mm beneath the surface, the average water vapour flux increased from  $5.5 \text{ mg m}^{-3} \text{ s}^{-1}$  to  $7.3 \text{ mg m}^{-3} \text{ s}^{-1}$ . In the atmospheric part of the domain, the volume average of water vapour concentration

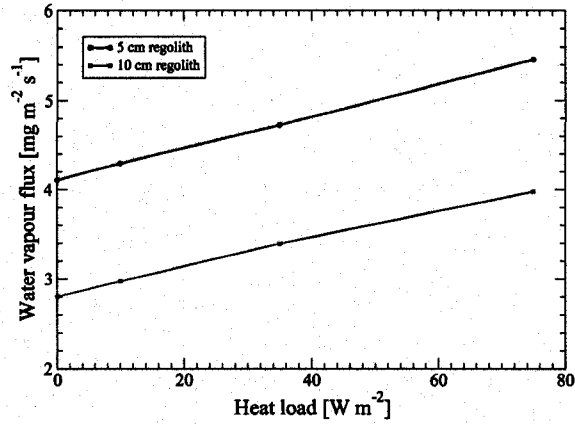


Figure 3.48: Average water vapour flux versus heat source at the surface and the regolith depth.

in the atmosphere domain increased from  $0.035 \text{ g m}^{-3}$  to  $0.037 \text{ g m}^{-3}$ . The surface water vapour concentration is rapidly transported with the plumes to the atmosphere.

### The $\overline{\text{Sh}}^*$ for natural convection

In a manner similar to the horizontal wind analysis, the special Sherwood number,  $\overline{\text{Sh}}^*$ , (defined in Chapter 2), for each case was calculated. These values are provided in the Table 3.5, where  $Q_s$  is the surface heat source with the units of  $\text{W m}^{-2}$ .

$Q_s$	$L_{reg}=5 \text{ cm}$	$L_{reg}=10 \text{ cm}$
0	1.00	0.96
10	1.02	1.00
35	1.07	1.08
75	1.10	1.19

Table 3.5: Special Sherwood numbers ( $\overline{\text{Sh}}^*$ ) for the natural convection cases.

### Grid Independence Analysis

Grid independence for the natural convection simulations was analyzed at three different grid levels. At the three grid levels ( $h_1$  to  $h_3$ ), with a node number ratio of 1.2 for the cubic root of the total node number, the average surface integral of water vapour density at a

horizontal plane 5 mm above the surface was calculated. The results are plotted in Fig. 3.49 and provided in Table 3.6. In this table,  $\bar{\rho}_{wv}^{h_i}$  is the average surface integral of water vapour density with the units  $\text{kg m}^{-3}$ . The difference of less than 2% between the two finest grids demonstrates that the results at the finest grid are acceptable.

H	$h_1$	$h_2$	$h_3$
N	229909	398672	683874
$N^{\frac{1}{3}}$	61	74	88
$\bar{\rho}_{wv}^{h_i}$	0.00034198	0.00033084	0.00032641

Table 3.6: Surface integral of water vapour density at a horizontal plane 5 mm above the surface, calculated at three grid levels.

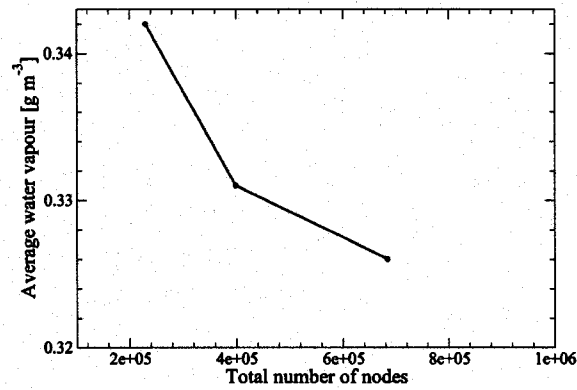


Figure 3.49: Average water vapour values at different grid levels.



## Chapter 4

# Experimental Validation

In order to partially validate the numerical simulations of local natural convection on Mars, an experiment setup was designed to create an artificial natural convection above a porous medium and to observe its effect on water vapour diffusion through a porous medium. Since this experiment was designed to ultimately accommodate the inclusion of a Phoenix Lander model, it had to be designed based on a lander scale, which is also the same scale as the numerical simulations discussed previously.

The experiment was carried out under Earth ambient conditions. With this approach, the experiment was then numerically simulated with the same mathematical models and the numerical solver that was used to simulate local flows on Mars. With such an experiment, it should be possible to test the numerical model's ability to simulate the transport phenomena of a trace gas in a porous medium under natural convection. However, considering the relatively large dimensions of the setup, it is extremely difficult to control and/or quantify all the influencing parameters. Therefore, due to the numerical challenges of comprehensively simulating such an experiment, a perfect match of experimental and numerical results was not expected. Rather, the objective was to create an environment of natural convection above a porous medium, to identify the difficulties and the affecting parameters for such an experiment and to observe and compare the experimental and numerical data of the bulk effects of natural convection on water vapour transport in a porous medium.

In the next sections, the experimental setup is described followed by the experimental results

and finally the comparison with numerical simulations.

## 4.1 The Experimental Setup

In order to create natural convection above a porous medium, the surface of the porous material should be heated to a higher temperature than the initial temperature above its surface. This will cause thermal buoyancy forces to form plumes and convective rolls.

Two common ways of generating heat on a surface are by infra-red radiation or by using an electrical current. For this setup, the former method was used. If a heated surface exists in a cooler environment, thermal buoyancy forces appear naturally, so as long as the porous medium surface temperature is higher than the air above it, natural convection is expected to be present. On the other hand, if there is a heat sink above the porous medium acting as a cold surface, the natural convection motion may be enhanced and for experimental and numerical simulation purposes, it may serve as a suitable boundary with known temperature. This is a desirable configuration for generating natural convection, because it creates a well defined Rayleigh-Benard convection between two hot and cold surfaces with known temperatures. Another benefit of using a cold surface on top is that since it acts as a constant heat sink, the convective motion can reach a steady state. Whereas, in case such a sink is absent, the air above the surface will eventually warm up and the thermal buoyancy forces will disappear. In the current study, both possibilities were investigated.

Furthermore, a porous material should be selected to represent the Martian regolith. For this purpose, two generic slabs of 5 cm thick, reticulated polyurethane foam [Foamex, 1999] were used.

A constant water vapour source should exist to represent the ice beneath the regolith and a region for natural convection. For this purpose, the experiment setup consists of two main sections, a reservoir tank and an enclosed region above the tank (Fig. 4.1). The tank contains water, which may be controlled to have a constant temperature with two porous foam layers above the water with no contact. The enclosed region of natural convection above the tank is designed to enhance recirculation and minimize the effects of external variables.

Data collected from the experiment were temperature and humidity using a network of systematically distributed sensors to capture the possible three dimensionality of the water vapour transport. By knowing the temperature and humidity data at any point, the water vapour density can be calculated. By measuring the water vapour density at various points in the porous medium, the effect of natural convection on water vapour transport can then be studied. To verify the estimates of total vapour flux and the mass balance in the experiment, the weight of water in the tank is measured with a large capacity digital scale, so that the total evaporated water from the tank can be measured.

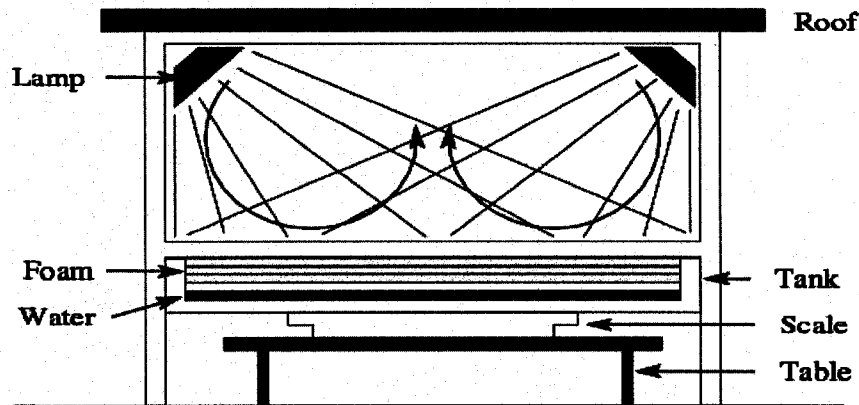


Figure 4.1: Diagram of the experiment setup

The entire experiment took place in a room with dimensions  $6 \times 3.5 \times 3.3$  m (L×W×H) with no ventilation. Temperature and relative humidity are also measured at various locations in the room as control points.

#### 4.1.1 The Water Tank

The purpose of the water tank was to provide a constant source of water vapour and to hold the foam layers, the sensor arrays and their support frames. The water tank contained a shallow layer of water at the bottom ( $\sim 2$  cm) with two 5 cm thick foam layers on top with a gap above the water surface to ensure that no liquid water reached the foam (Fig. 4.2). The tank body has the dimensions  $200 \times 105 \times 18.5$  cm (L×W×H), made of a light aluminum honey-comb structure. Three portable, aluminum frames were built to support the layers

of humidity and temperature sensors.

The water layer in the tank was designed to be maintained at a temperature,  $T$ , in the range of  $0 \leq T \leq 15 \text{ }^\circ\text{C}$ , via a coolant recirculation through 9.52 mm diameter copper tube coils at the bottom of the tank.

The tank was placed on a large capacity scale (Toledo<sup>TM</sup>), supported by a table. This scale has a resolution of 1 g for a maximum weight of 100 kg. This allows the scale to measure the change in water weight inside the tank, giving the total water evaporated, despite the total weight of the filled tank being approximately 40 kg.

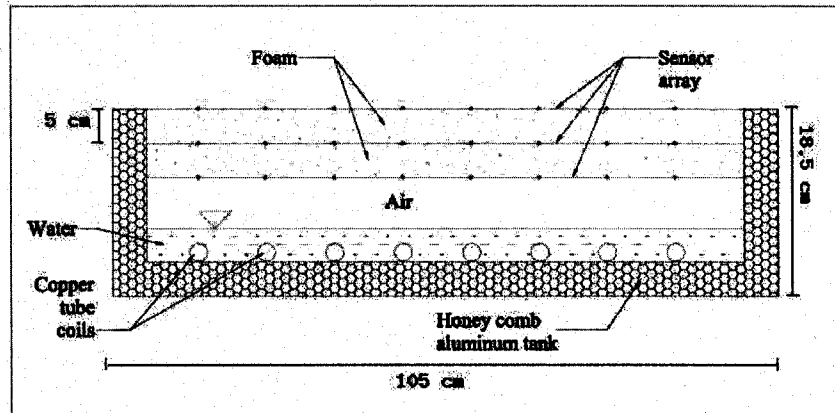


Figure 4.2: Diagram of the water tank

A system to level the tank was also installed in two directions on the tank sides. A properly leveled tank ensures uniform water evaporation at the bottom and prevents the risk of some locations drying out. Although the setup was not designed to be airtight, the gaps and openings were sealed with generic tape (not a perfect seal).

#### 4.1.2 The Natural Convection Enclosure

The purpose of the enclosure, around the tank, is to separate the experiment area from the outside environment in order to enhance recirculation and to reduce external disturbances.

The enclosure consists of an inner frame with acrylic windows (to separate the convective area from the outside), a pair of radiant heaters and a cool surface at the top.

### The Inner Frame

The inner frame was required to support 6 windows and a cooled roof, without conveying any force to the tank (for accurate weighing of water inside the tank) and to hold two infra-red heaters to evenly radiate on the foam surface. The windows are made of 3.18 mm clear acrylic sheet and are bolted to the inner frame from the outside.

The lamps were designed to raise the surface temperature to a maximum of 50°C. For that purpose, two 0.95 kW radiant heaters from Caloritech<sup>TM</sup> (model OKA299C6) with 60° angle reflectors were selected to radiate heat on the surface of the porous material. Positioned at the top corner ends of the inner frame, their reflector angles were adjusted so that the foam surface receives relatively uniform irradiation. From Fig. 4.3 it can be seen that the foam surface has less than 20% variation in incident irradiation. Convective rolls were expected to form between the cold roof and the warm surface of the foam.

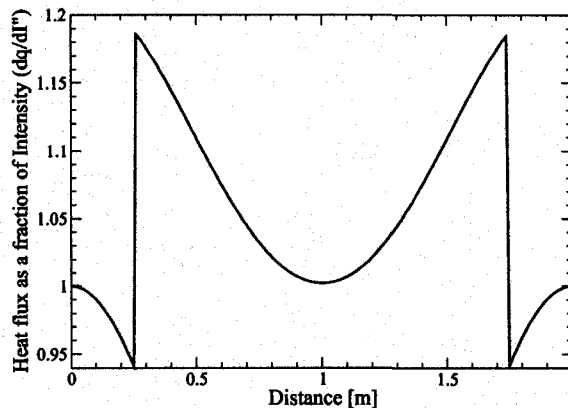


Figure 4.3: The heat flux calculated as a fraction of Intensity along the table length.

### The Roof

The roof serves the purpose of providing a cold surface above the inner frame to help convection and to condense and remove excess water vapour from the enclosure. In order

to create the cold surface, two sets of copper tube coils were attached to the top of an aluminum sheet as shown in Fig. 4.4.

To collect the water which condenses beneath the cooling roof and to prevent droplets from falling inside the enclosure, the roof surface should be slightly inclined from the middle of the surface towards the outside. The roof thus has an adjustable inclination ( $0 \leq \theta \leq 30^\circ$ ). This was done by connecting the two aluminum sheets (which compose the roof) with a piano hinge, and placing height adjustable bars at the far length ends of the roof.

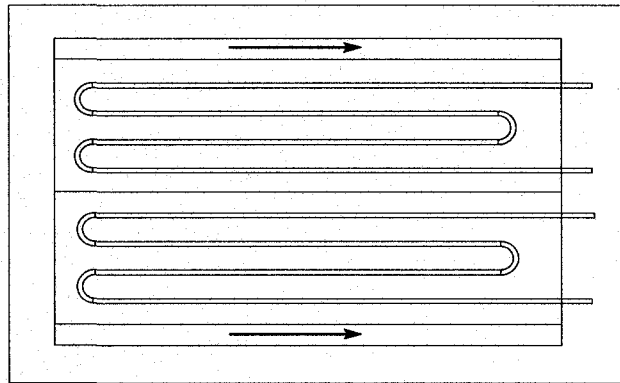


Figure 4.4: Diagram of roof showing placement of coils and direction of flow in the troughs.

The top of the roof is insulated with a  $\sim 5$  cm thick fiberglass sheet to prevent heat transfer from the room. A special epoxy treatment was used between the copper tubes and the Aluminum surface to increase thermal conductivity.

### 4.1.3 Measurements and Electronics

During the experiment, humidity and temperature was measured at three surfaces within the porous medium (foam). One hundred and twenty humidity and temperature sensors were placed on three layers (40 sensors per layer) in the tank, located at the top, bottom and the middle of the regolith surrogate (see schematic in Fig. 4.6).

The sensors are type SHT71 digital, capacitive relative humidity and temperature sensors

from Sensirion AG. According to SensirionAG [2008], the highest accuracy for the humidity measurements of the sensors is  $\pm 3$  %RH in the range of 20 to 80 %RH and for temperature measurement, it is  $\pm 0.5^\circ\text{C}$  at  $25^\circ\text{C}$  (accuracy decreases at other temperatures, e.g., it is  $\pm 1.5^\circ\text{C}$  at  $60^\circ\text{C}$ ). The humidity read out ( $SO_{RH}$ ) of the sensors are converted to %RH values using the following relation,

$$RH_{linear} = c_1 + c_2 SO_{RH} + c_3 SO_{RH} \quad (4.1)$$

where  $c_1$ ,  $c_2$  and  $c_3$  are equal to -4.0000, 0.0405 and  $-2.8 \times 10^{-6}$ . For temperatures different from  $25^\circ\text{C}$ , the following correction equation is used,

$$RH_{true} = (T - 25) (t_1 + t_2 SO_{RH}) + RH_{linear} \quad (4.2)$$

where  $t_1$  and  $t_2$  are 0.01 and  $8 \times 10^{-5}$  respectively [SensirionAG, 2008].

The sensors were connected to 4-wire, non-insulated, variable length (1-4 m) cables and directed outside the tank through several holes in the tank sides. The sensors were soldered to the cables and protected by insulation shrink fitting. The cables were then connected to a 128 port data logger with 128 male RJ-45 connectors. A DB-25 output from the collector box was connected to a parallel interface in the computer, where data was recorded (See diagram in Fig 4.5).

Since the humidity sensors cannot be immersed in water, several type T, gauge 26 thermocouples with an approximate length of 4 m were used to measure the water temperature in the tank and at various control points. These thermocouples were connected to an analog thermocouple input module (with a built-in cold junction) as an interface for the computer.

Finally, the weight measurements of the tank scale are recorded via a direct serial interface with a computer.

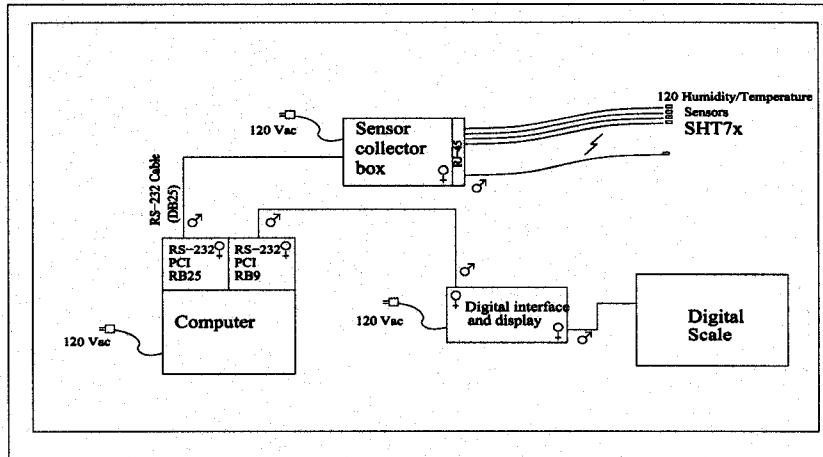


Figure 4.5: Diagram of the electronics layout.

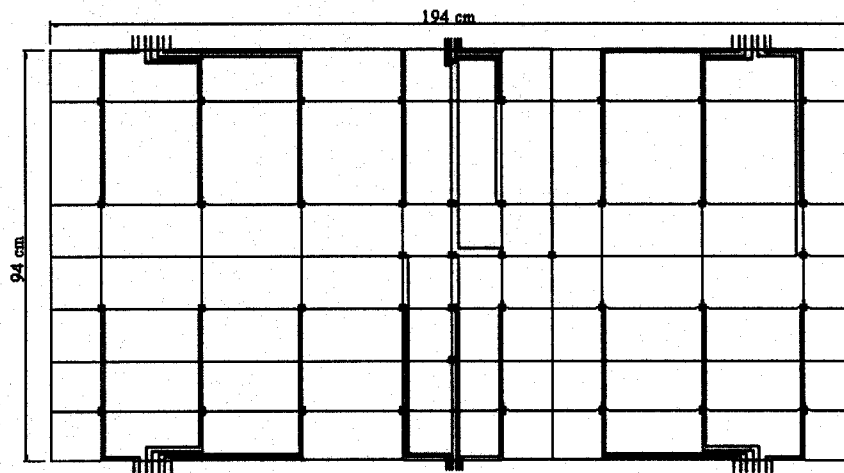


Figure 4.6: Diagram of the sensor cable path in the tank.



#### 4.1.4 Hydraulics

To provide a constant temperature heat sink as an upper boundary for the natural convection enclosure and to maintain the water vapour source at a constant temperature, a hydraulic system was designed to transfer a coolant liquid from a reservoir to copper tube coils in the tank and on the cooling roof. Tap water was used as the coolant.

The hydraulic system is composed of a pump, a reservoir, pipes and fittings. A pump was selected according to the hydraulic losses and the required flow rate needed to transfer water through the copper tube coils. A chest freezer, as the coolant reservoir, was used to deposit ice-water and to provide a constant source of near 0 ° C water. After the hydraulic system was installed, water recirculated at 3.78 L min<sup>-1</sup> in the tank and the roof tubes. Fig. 4.7 shows the experimental setup without the foam layers, revealing the network of sensors.

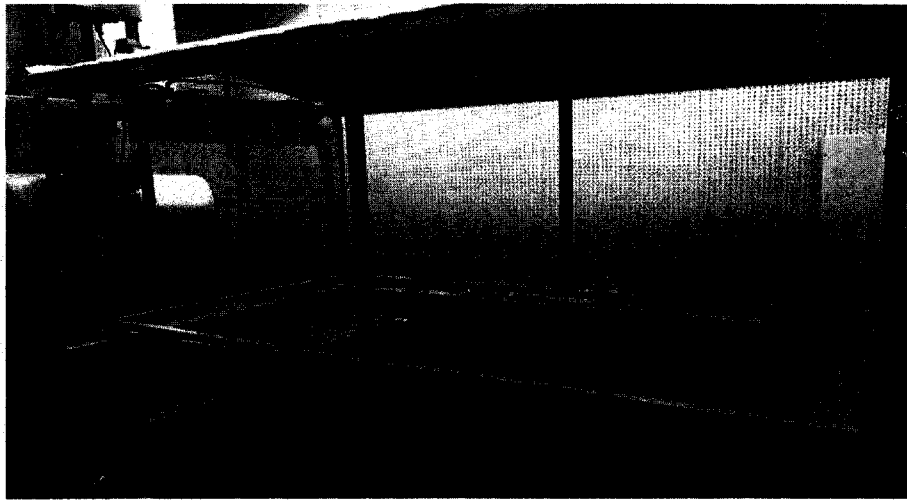


Figure 4.7: The experimental setup.

## 4.2 Calibration Procedure

### 4.2.1 Thermocouples

Six type T, gauge 26 thermocouples were prepared with two ends: one end as the double metal junction and the other was connected to six channels of a thermocouple module. The

module is a Super Logics 8010 analog thermocouple input module and it is connected to a computer using a serial interface. For this configuration, there was no need to use an external cold junction connection (CJC), because the module has a built in CJC correction. The module was first calibrated and then, a temperature offset was set for it (which is the difference between the actual temperature and thermocouple readings).

After the thermocouple module was calibrated, the thermocouples were calibrated with a heating/cooling water bath, the Rosemount calibration bath model 910AC, which provides a highly uniform and stable temperature within the range of -30 to 400 °C. The thermocouple junctions were immersed 5 to 7 cm in the bath along with a traceable digital thermometer. This thermometer is calibrated at four points (0, 25, 60, 100 °C) and is accurate to 0.005 °C. After the water bath reached a constant temperature, at equilibrium, measurements from the thermocouple were collected for approximately five minutes. During this time, the thermometer was observed for any temperature change. Data was collected for 8 temperatures in the water bath, ranging from 6 °C to 65 °C.

## **4.2.2 Humidity and Temperature Sensors**

The sensor type that was used to measure relative humidity and temperature is SHT71 from Sensiron. 138 sensors were calibrated for humidity and temperature measurements. The calibration process was separate for humidity and temperature.

### **Temperature Calibration**

The limitation for calibrating the temperature sensor component of the sensors was that they could not be immersed in a liquid. Therefore, a generic household chest freezer was used (Danby, model Premiere DCF555BL). The freezer could provide cold temperatures for calibration. When the chest freezer was working at full cooling capacity and was covered with an insulating lid, the temperature at the inside bottom of it reached down to -32 °C, depending on the room temperature and the insulating lid material. After the bottom of the freezer reached this temperature, it was possible to use it as a temperature point for calibration. For other temperature points, the freezer was turned off and the lid was removed

until the bottom of the freezer reached a desirable higher temperature. At this time, the lid was placed back and after an adequate time, the temperature inside the freezer stabilized. From this point, the temperature inside the freezer increased very slightly<sup>1</sup>. The sensors were then calibrated with the calibrated thermocouples at transient temperature points for three minutes. Each time, 32 sensors were attached to a thin aluminum sheet (47×3 cm). The sheet had holes drilled in it at equal intervals. Seven calibrated thermocouples were also attached to the sheet at equally spaced locations. At several different temperature points between - 32 °C and room temperature, sufficient (at least 30) samples were taken for all 138 sensors and thermocouples, simultaneously.

### Humidity Calibration

There are several ways to calibrate relative humidity. One easy and standard procedure is to use saturated salt solutions. A closed container, partly filled with saturated salt solutions (distilled water saturated) generates a stable relative humidity above the salt, which is not sensitive to temperature. The value of the relative humidity depends on the type of salt used. Since the relative humidity above some saturated salt solutions changes only very slightly with large temperature changes, the change in %RH due to room temperature variations during the calibration is negligible.

To calibrate the sensors, two different laboratory grade salts were used, Sodium-Chloride and Potassium-Carbonate, each providing approximately 43 % and 75 % relative humidity at room temperature, respectively. Since the SHT71 sensors have a maximum accuracy of 3 %, and the salts that were used have a relative humidity change of 1 % for every 100 °C temperature change, the calibration process is essentially an output verification check for the sensors. For this purpose, two Erlenmeyer containers (container capacity was 500 ml for K<sub>2</sub>CO<sub>3</sub> and 200 ml for NaCl) were filled with the saturated water-salt solution to an approximate height of 1 cm, which were then saturated with generic distilled water. At each time, ten sensors were passed through a rubber stopper that had a hole in the middle and the opening of the container was closed by the stopper. Then, the perimeter of the stopper

---

<sup>1</sup>It should not be a problem for calibrations with 1 °C accuracy. These sensors have a factory claimed accuracy of 0.5 °C at 25 °C, we expect 1 °C accuracy in the temperature range of the experiments which is  $0 < T < 70$  °C.

and the hole with the sensor wires were sealed (not perfectly airtight) with regular, wide, glass tape. Finally, after adequate time was allowed for the solution to reach equilibrium, the relative humidity was sampled at least 20 times. It should be mentioned that response time of these sensors for humidity is 4 s. Nevertheless, at least 15 s was allowed between each reading for a more stable result. At the end, the sensors that did not provide expected relative humidity values over the saturated salts were flagged as defective and excluded.

### 4.2.3 The Scale

The scale used to measure the weight of water in the tank was calibrated using specimen calibration weights (OHAUS brand). For each weight point, data was collected ten times. Ten weight points were measured ranging from 0.01 to 0.10 kg, ten weight points in the range of 0.10 to 1.00 kg and three readings at 2.00 kg, 3.00 kg and 4.00 kg.

## 4.3 Experiments

The experiments were performed in two series. In the first series, the configuration was initially at room temperature and after a certain amount of time, the radiant heaters were turned on to raise the surface temperature of the foam. Without cooling the water in the tank or the roof, natural convection would still appear due to the temperature difference between a high temperature surface in a lower temperature environment. For the second series, cooling was provided for the tank water and for the roof to keep them at a possibly constant lower temperature than the surface. These two experimental approaches towards simulating natural convection are discussed separately.

Temperature and relative humidity data were collected from thermocouples and temperature/humidity sensors at various locations in the foam, enclosure and the room. Since the temperature has a spatio-temporal variation in this experiment, the %RH alone cannot be used as an indication of water vapour concentration, due to the fact that the saturation water vapour pressure depends on temperature, hence the water vapour concentration (density) is a function of both the %RH and temperature at any point.

The water vapour saturation pressure can be calculated from [Wagner and Pruß, 2002], which is valid in the range of 273.16 K < T < 647.096 K,

$$\ln \left( \frac{P_{wsat}}{22.064 \times 10^6} \right) = \frac{647.096}{T} \left( -7.85951783v + 1.84408259v^{1.5} - 11.7866497v^3 + 22.6807411v^{3.5} - 15.9618719v^4 + 1.80122502v^{7.5} \right) \quad (4.3)$$

$$v = 1 - \frac{T}{647.096} \quad (4.4)$$

where T is in Kelvin and  $P_{wsat}$  is in Pa. Assuming water vapour to be an ideal gas and since %RH is defined as,

$$\%RH = \frac{P_{wv}}{P_{wsat}} \cdot 100 \quad (4.5)$$

then water vapour density can be calculated with the following formula,

$$\rho_{wv} = \frac{\%RHP_{wsat}M_w}{100RT} \quad (4.6)$$

where  $M_w=18.015 \text{ g mol}^{-1}$  is the molecular weight of water and  $\rho_{wv}$  is in  $\text{g m}^{-3}$ .

### 4.3.1 First Series

To reduce the water adsorption effects of the foam [Prieto, 2006], the experiment configuration was allowed to reach equilibrium with the room. This is achieved when the sensors show a relatively constant %RH over time.

The experiment was commenced by reading humidity and temperature data in the configuration and the room. After a certain time period elapsed, the radiant heaters were turned on to generate heat at the foam surface. The heaters remained on until the end of the experiment. The duration of each experiment was approximately 10 h. The repeatability of the experiment was tested with several runs for the first series, which all showed very close results under similar conditions. To study the effect of the natural convection generated by

the radiant heaters, the net water evaporation from the tank and the water density in the foam layers were compared with the case when natural convection was not present. For the sake of consistency, this comparison was done in the same run (before and after the heaters were turned on).

As a sample, one case is discussed here, which represents all other runs. For this run, the total experiment time was  $t_f=35015$  s (9:43 h). The heater was turned on at  $t_h=17350$  s (4:49 h), which corresponds to sample number 380 (S380). A total of 763 samples ( $\sim 1$  sample every 46 s) were taken from the 128 sensors.

Temperature and humidity at the room, tank and enclosure control locations can be seen from Fig. 4.8 to Fig. 4.12. The room is initially at 25° C and remains at this temperature until  $t_h$ . After the heater is turned on, there is a sudden increase in the temperature with the maximum values recorded at the heater reflector. The room experiences an approximately 5° C temperature rise in 5 h (Fig. 4.8). The tank water temperature, also, rises 5° C during this time (Fig. 4.8). This indicates that even without cooling, the water vapour density source variation due to temperature increase is negligible. An increase in the evaporation rate due to a higher temperature liquid (increase in the molecular energy levels) is also not significant, thus it may be assumed that any change in the water evaporation rate and net evaporation is caused by the surface natural convection.

Fig. 4.10 shows the water vapour density levels in the room. It is evident that water vapour density is relatively constant (6 to 8 g m<sup>-3</sup>) during the experiment run except for the sensor that is located near the enclosure. This sensor measured a slightly higher water concentration, which is expected due to the proximity to the water vapor source (the tank). However, after the heater is turned on, all sensors in the room show the same level of water density in the room. This may be due to the reason that when the heater is turned on, the temperature of the enclosure windows rise, thus creating a convection motion with an outward flow direction from the enclosure.

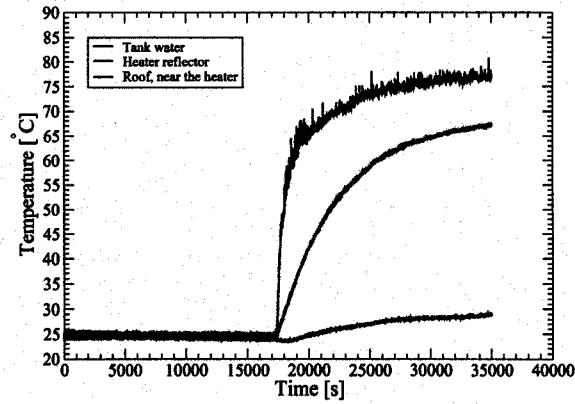


Figure 4.8: Control temperatures measured by thermocouples at various locations.

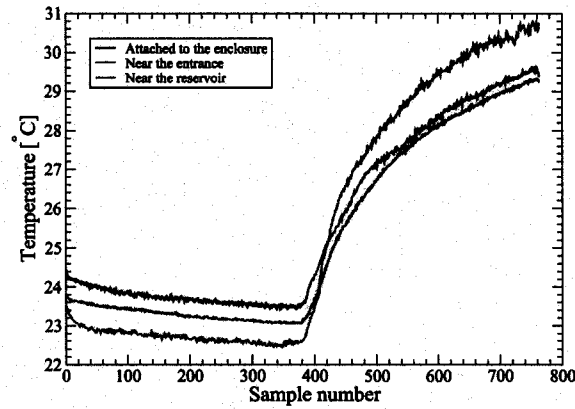


Figure 4.9: Control temperatures measured by sensors at various locations in the room.

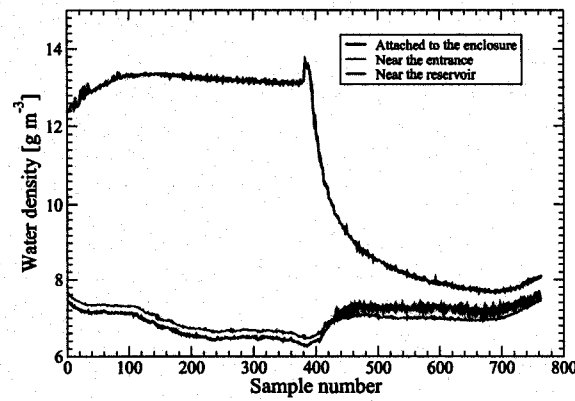


Figure 4.10: Water vapour density measured by sensors at various locations in the room.

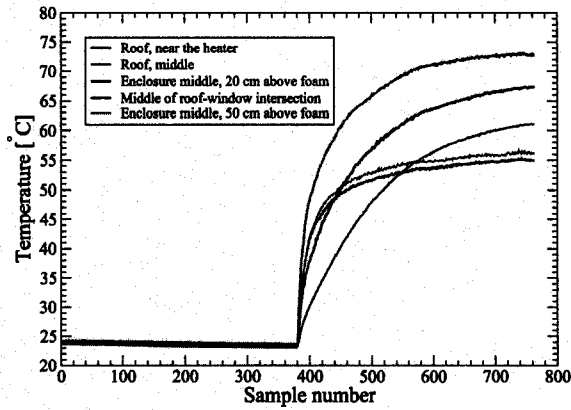


Figure 4.11: Control temperatures measured by sensors at various locations in the enclosure.

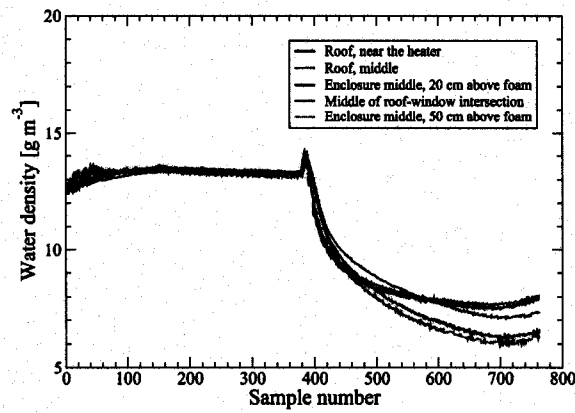


Figure 4.12: Water vapour density measured by sensors at various locations in the enclosure.

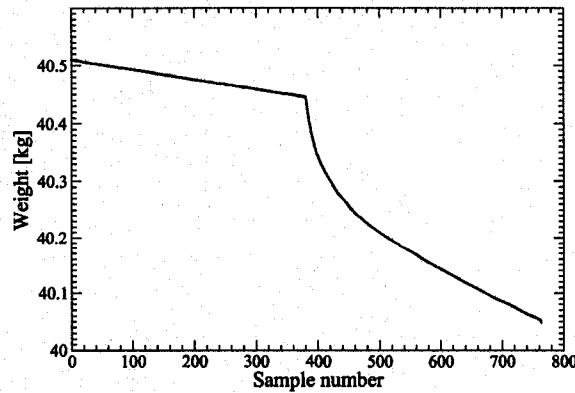


Figure 4.13: Instantaneous tank weight during the experiment period.



After the heaters are turned on ( $t_h$ ), it is evident from Fig. 4.13 that there is a sudden increase in the evaporation rate of the tank water. Over a period of 4:49 h before the heater is turned on, a total of 0.065 kg is evaporated, but after the heater is turned on for the same period of time, a significant amount of 0.392 kg evaporates. Immediately after  $t_h$ , there is a sharp gradient in the tank water weight. This steep gradient (very high evaporation rate) shortly changes to a milder slope which remains almost constant until the end of the experiment. Nonetheless, the evaporation rate of the tank water is always higher after the surface heating of the foam. To better illustrate this, three time periods can be defined for the experiment duration: the initial resting period with no heating ( $\Delta t_1=t_h$ ), the period of a very high water evaporation rate ( $\Delta t_2=2760$  s), which is very short, and the final time period until the end of the experiment ( $\Delta t_3=t_f-\Delta t_2-\Delta t_1$ ). If the water in the tank is linearly plotted for these time intervals, the linear evaporation rates can be easily compared (Fig. 4.14).

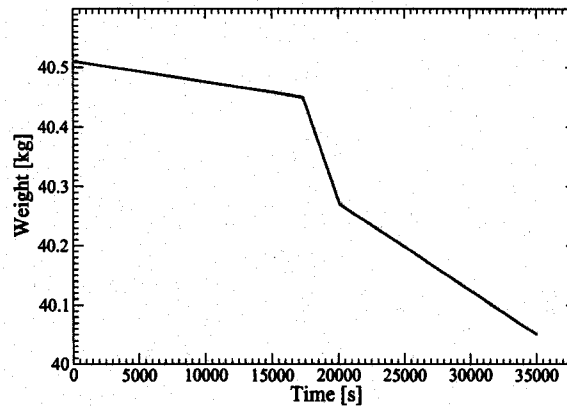


Figure 4.14: Linearized instantaneous tank weight during the experiment period.

During  $\Delta t_1$ ,  $\Delta t_2$  and  $\Delta t_3$ , a net amount of 0.065 kg, 0.177 kg and 0.222 kg evaporated respectively. If the linear evaporation rate is calculated as,

$$\dot{m} = \frac{m_2 - m_1}{\Delta t} \quad (4.7)$$

then for the three time periods,  $\dot{m}_1=0.0135$  kg h<sup>-1</sup>,  $\dot{m}_2=0.231$  kg h<sup>-1</sup> and  $\dot{m}_3=0.0536$  kg h<sup>-1</sup> or  $j_1=1.87 \times 10^{-6}$  kg m<sup>-2</sup> s<sup>-1</sup>,  $j_2=3.20 \times 10^{-5}$  kg m<sup>-2</sup> s<sup>-1</sup> and  $j_3=7.45 \times 10^{-6}$  kg m<sup>-2</sup> s<sup>-1</sup>, respectively.

The increase in the evaporation rate after the foam surface heating may be studied with the temperature and %RH data from the foam layers. For this purpose, the sensors at a concentrated square area of 25×25 cm at the centre of each sensor layer are designated as the primary sensors and their data is analyzed. Only the correctly functioning sensors are included in the analysis.

Fig. 4.20 to Fig. 4.22 show a temperature increase on all three sensor layers. Under the foam, the temperature slightly increases at about 3°C over the heating time period, which may be assumed constant in the numerical modelling. At the middle layer of the foam, the temperature gradually rises over the heating time to approximately 42°C, however, surface sensors show an initial sudden temperature increase to a maximum of 60°C and remaining almost at the same temperature until the end of the experiment. Fig. 4.21 illustrates the average temperature at each sensor layer by averaging the sensor readings at each layer. It is evident that approximately 2 h after surface heating, a stable, inverse, linear temperature gradient is formed in the porous medium and remains until the end of the experiment.

On the other hand, by observing the average water vapour density at the three sensor layers (Fig. 4.22), it is evident that the linear density gradient from the pre-heating period, changes drastically after surface heating. The water vapour density at the first layer (under the foam) increases very slightly after heating. This is expected because a slightly higher water temperature in the tank increases the evaporation rate. Since the density increase at the first layer is not significant, a constant water vapour source to the foam can be assumed. However, water vapour density decreases at the middle and top of the foam. Between the top and middle layer, a very high density gradient is evident, which implies a higher water vapour diffusion rate. This change in the vapour density gradient can be seen in Fig. 4.23, which illustrates a comparison of the water vapour density gradient at two arbitrary instances after and before surface heating.

The water vapour flux from tank, during the pre-heating time ( $\Delta t_1$ ), is  $j_1 = 1.87 \times 10^{-6} \text{ kg m}^{-2} \text{ s}^{-1}$  and the linear water vapour gradient, in the pre-heating time, from Fig. 4.23, is  $\left(\frac{\Delta \rho_w}{L}\right)_0 = 0.03 \text{ kg m}^{-4}$ . By using the relation,

$$j = \Gamma_l \left(\frac{\Delta \rho_w}{L}\right)_0 \quad (4.8)$$

$\Gamma_l$ , which is a coefficient that includes the foam porous properties (porosity, permeability and tortuosity), the diffusion coefficient of water vapour in air ( $D_{wa}$ ) and a compensating factor for the leakage of water vapour from the tank (which does not enter the foam), can be calculated and is  $\Gamma_l=6.23\times 10^{-5} \text{ m}^2 \text{ s}^{-1}$ . This coefficient can now be used to obtain the vapour flux in the foam, from the vertical vapour density gradient, for both the sensor readings and the numerical simulations.

The natural convection motion at the surface can be interpreted by the higher fluctuations in temperature and water density measured by the sensors (Figs. 4.17 and 4.20). These fluctuations are clearly evident when compared to the no-heating period and may indicate the chaotic flow structure at the surface due to natural convection.

Finally, the diffusion process in the middle of the foam can be assumed to be a one dimensional process. This is realized from the fact that, at all three sensor levels, sensors show the same water vapour density values with respect to time and do not have variations in the horizontal plane (Fig. 4.18 to Fig. 4.20).

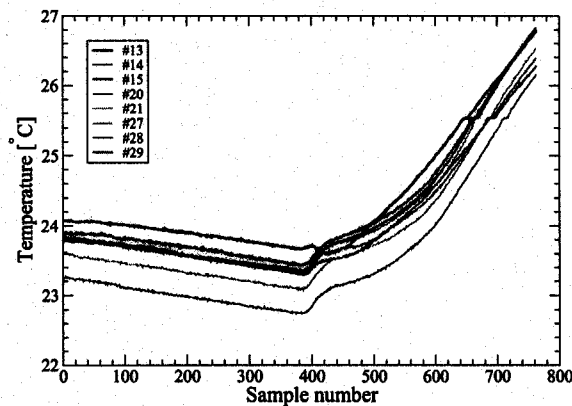


Figure 4.15: Temperatures measured by several sensors located under the foam in the middle of the tank.

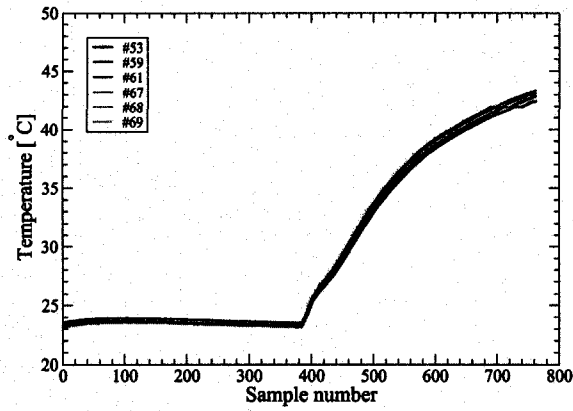


Figure 4.16: Temperatures measured by several sensors located between the two foam layers in the middle of the tank.

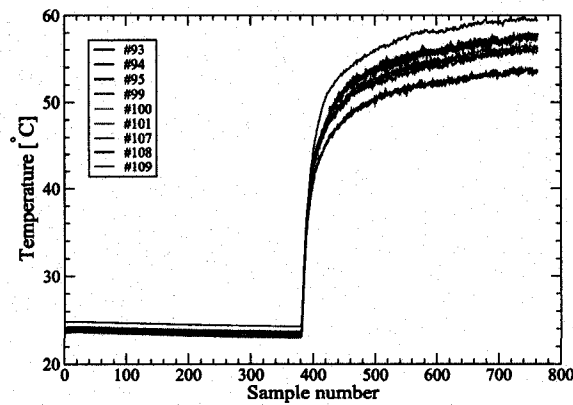


Figure 4.17: Temperatures measured by several sensors located at the foam surface in the middle of the tank.

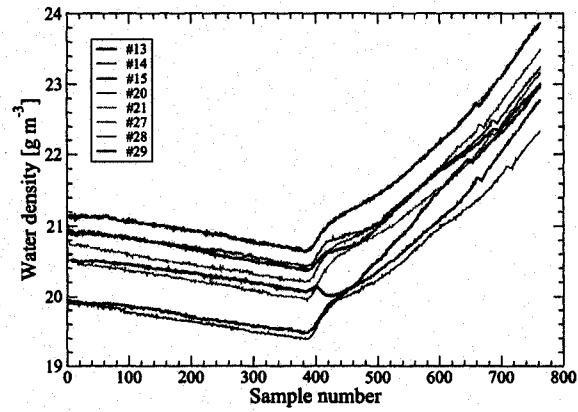


Figure 4.18: Water vapour density measured by several sensors located under the foam in the middle of the tank.

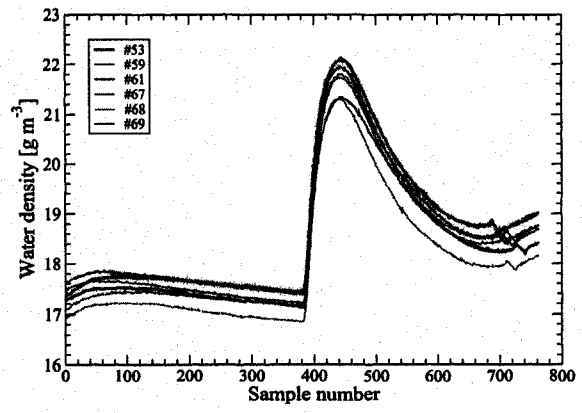


Figure 4.19: Water vapour density measured by several sensors located between the two foam layers in the middle of the tank.

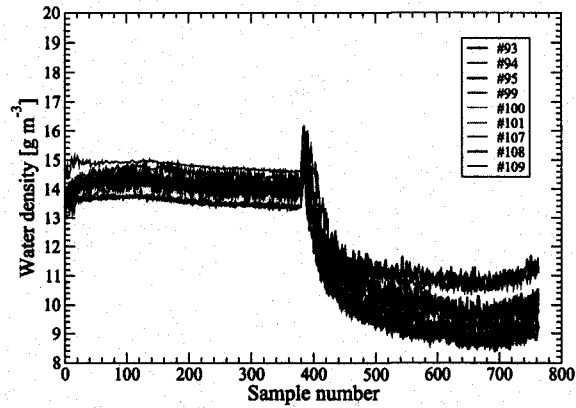


Figure 4.20: Water vapour density measured by several sensors located at the foam surface in the middle of the tank.

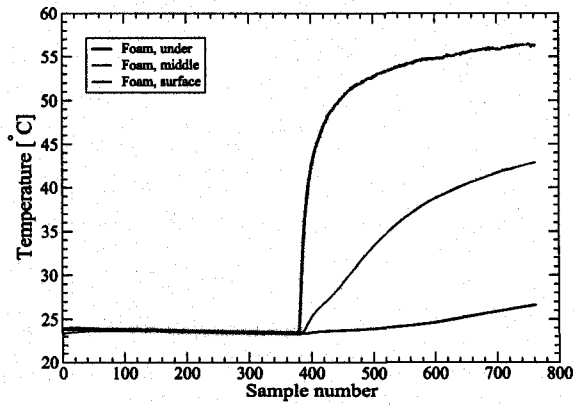


Figure 4.21: Layer averaged temperatures of several sensors located in the middle of the tank.

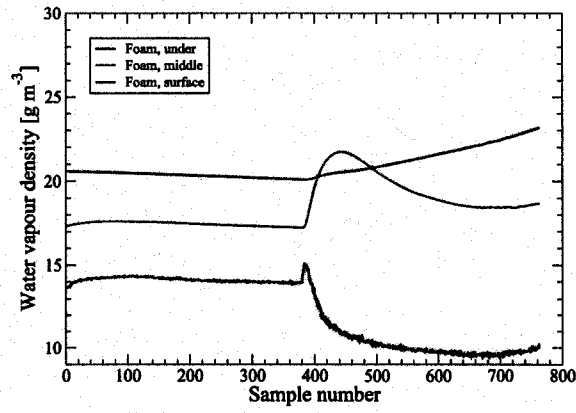


Figure 4.22: Layer averaged water vapour density of several sensors located in the middle of the tank, sample 1.

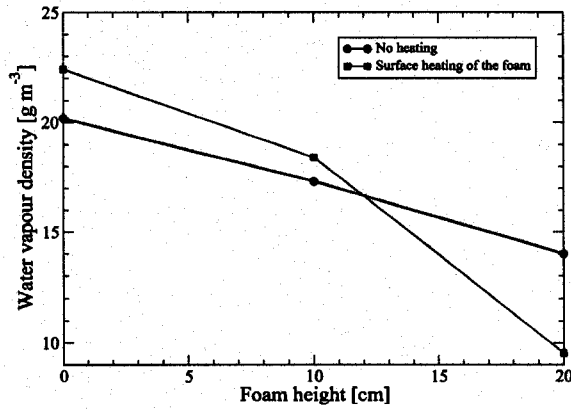


Figure 4.23: Layer averaged water vapour density in the foam comparison for after and before the surface heating of the foam.

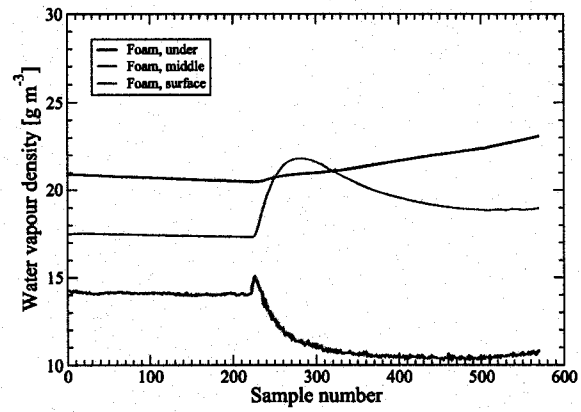


Figure 4.24: Layer averaged water vapour density of several sensors located in the middle of the tank, sample 2.



### 4.3.2 Second Series

It was mentioned that the natural convection experiments can be performed with the roof and the tank water being at a cold temperature and serving as heat sinks. This procedure has the advantage of providing a cold boundary above the foam surface in the enclosure, thus enhancing the convective recirculation and keeping the tank water at a constant temperature to avoid the effects of temperature rise on evaporation. However, a large reservoir of a cooling fluid with a high cooling capacity is needed for this purpose. The cold water reservoir that was available for this experiment was a chest freezer (the same that was used for calibrating the temperature sensors) filled with an ice-water mixture. Several times during the experiment, ice needed to be added to the mixture, which caused interruptions that affected the data. The sensitivity of this procedure to the cold reservoir is apparent from Fig. 4.25 to Fig. 4.28, which are included for reference. Several attempts were made to reduce the heat load transferred to the water to increase the period of stable temperatures, but these were unsuccessful. The data from this series are deemed unreliable to analyze.

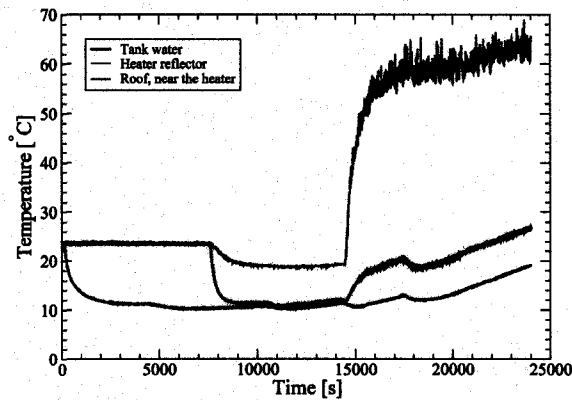


Figure 4.25: Control temperatures measured by thermocouples at various locations, series 2.

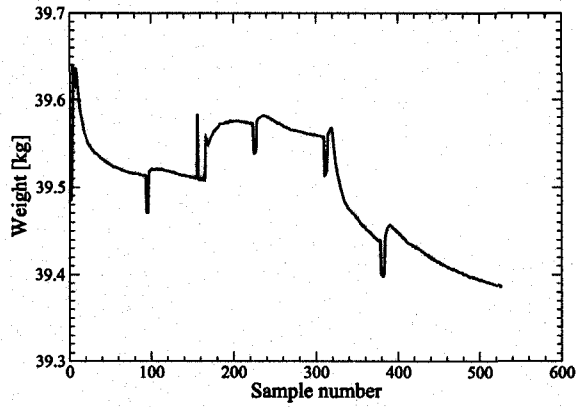


Figure 4.26: Instantaneous tank weight during the experiment period, series 2.

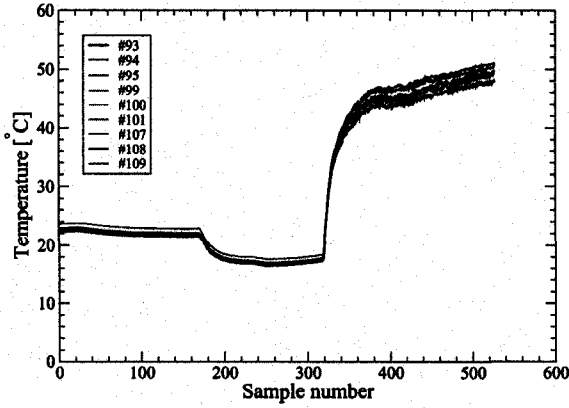


Figure 4.27: Temperatures measured by several sensors located at the foam surface in the middle of the tank, series 2.

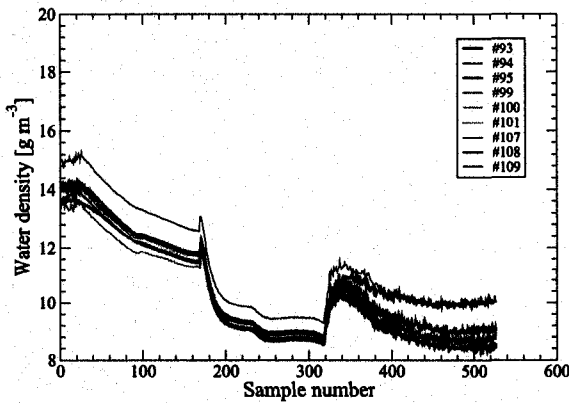


Figure 4.28: Water vapour density measured by several sensors located at the foam surface in the middle of the tank, series 2.

## 4.4 Numerical Model Validation

To partially validate the numerical model for natural convection on a porous medium, the experiment configuration was simulated. Since there are many uncertainties associated with the current setup, the simulations are not expected to exactly follow the experimental results. The main purpose of performing this simulation, is to observe the effects of a surface natural convection on water vapour transport through a porous medium, to explore the numerical modelling aspects of the experiment and to identify possible obstacles for future experimental approaches of this type. As an outcome, the numerical simulation may agree qualitatively with the experiments.

The numerical simulation discussed here is for the experimental case of surface heating of the foam with no cooling at the roof and the tank water. A numerical simulation is not performed for the cold boundary experiments (series 2) due to the major inconsistencies and the required interruptions during the runs.

### 4.4.1 Numerical Setup

For the numerical simulation, a 3-D geometry is created that approximately represents the experimental setup. The top part is a fluid domain, that simulates the natural convection enclosure, and the bottom part is a porous domain, that simulates the foam in the tank. The entire domain is meshed with tetrahedra elements and an interface area refinement is applied with the same procedure that was used for the Martian simulations (Fig.4.29).

The transport equations and their numerical discretization are also the same as the Martian simulations, which were described in Chapter 2 and Chapter 3.

The simulation is, transient with a 0.1 s timestep used for the second order implicit time discretization scheme, and a laminar model is used.

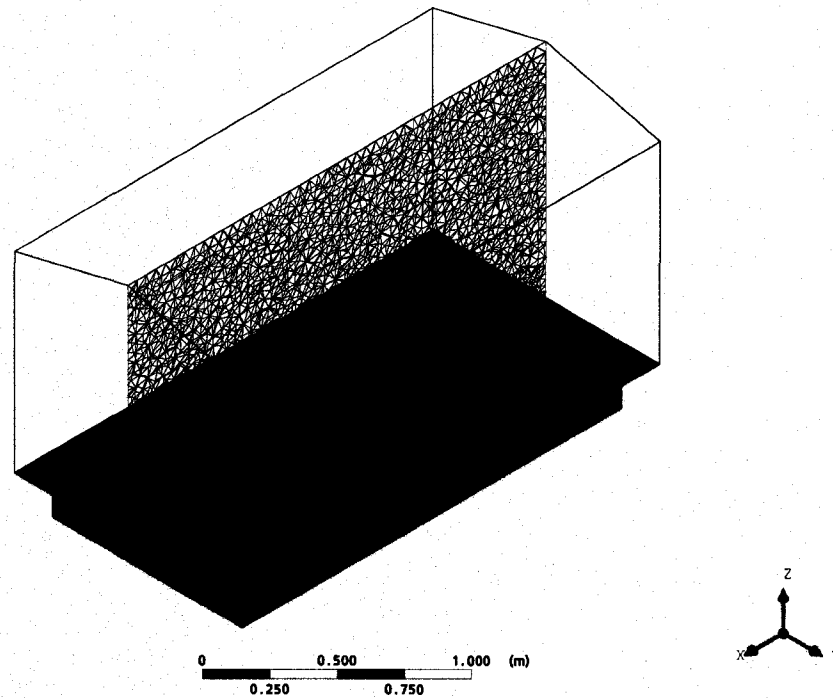


Figure 4.29: The 3-D model of the experiment setup and the mesh at the ZX plane.

### Material Properties

The fluid material in the enclosure domain is constant property dry air at 35°C (properties in Table 4.1 and Table 4.2).

The porous properties used for the foam are obtained from [Prieto, 2006], summarized in Table 4.3. Thermal conductivity of the foam is calculated using the single probe method outlined in Nusier and Abu-Hamdeh [2003], DeJager and Charles-Edwards [1969]. Thermal conductivity of an air-filled polyurethane foam can also be theoretically obtained from,

$$k_{foam} = \phi k_{air} + (1 - \phi) k_{PU} \quad (4.9)$$

where  $k_{PU}$  is the thermal conductivity of pure generic polyurethane and it is approximately

$0.2 \text{ W m}^{-1} \text{ K}^{-1}$  and  $\phi$  is the foam porosity.

The numerical modelling parameters and conditions are all prescribed as close as possible to the experimental results.

$T_{ref}, ^\circ \text{C}$	$P_{ref}, \text{atm}$	$\rho_{air}, \text{kg m}^{-3}$	$\eta, \text{Pa s}$	$M_{air}, \text{g mol}^{-1}$	$D_{wa}, \text{m}^2 \text{s}^{-1}$
35	1	1.149	$1.858 \times 10^{-5}$	28.96	$2.69 \times 10^{-5}$

Table 4.1: Transport properties used in the numerical simulation for air at  $35^\circ\text{C}$ .

$T_{ref}, ^\circ \text{C}$	$P_{ref}, \text{atm}$	$C_P, \text{J kg}^{-1} \text{K}^{-1}$	$\beta$	$k_{air}, \text{W m}^{-1} \text{K}^{-1}$
35	1	1005.8	0.003246	0.0268

Table 4.2: Thermal properties used in the numerical simulation for air at  $35^\circ\text{C}$ .

Foam thickness, cm	$\phi$	$K, \text{m}^2$	$k_{foam}, \text{W m}^{-1} \text{K}^{-1}$
20	0.97	$2.22 \times 10^{-9}$	0.0299

Table 4.3: The foam properties.

## Boundary Conditions

In the air enclosure domain, two types of boundary conditions were considered for water vapour at the top roof, a zero vapour flux and a Dirichlet condition with water density at  $0.012 \text{ g m}^{-3}$ . The zero flux condition represents a completely sealed enclosure and the prescribed density case may be assumed as a vapour sink, that takes into account the escape of vapour from an unsealed enclosure. For both cases, since the roof is insulated, an adiabatic boundary condition was prescribed. At the windows, temperature is set to room temperature, which increases from  $25^\circ\text{C}$  to  $30^\circ\text{C}$ , linearly over time and a zero vapour flux is assumed for water vapour.

For the foam domain, the foam vertical sides are adiabatic. The bottom boundary of this domain has Dirichlet boundary conditions for both temperature and water vapour. Water vapour is set to  $0.020 \text{ g m}^{-3}$  which increases linearly to  $0.024 \text{ g m}^{-3}$  over the experiment period. Temperature is set to  $24^\circ\text{C}$  and also linearly increase to  $26.5^\circ\text{C}$ .

At the foam-air interface, a  $100 \text{ W m}^{-2}$ , uniform surface heat flux is prescribed at the foam nodes, simulating heat generation due to irradiation from the radiant heaters. This value

was obtained by trial and error, which approximately causes the same temperature rise at the foam surface. The interface also has a conservative flux condition for all transport quantities.

Finally, all the walls have a no-slip boundary condition for velocity.

## Initialization

Velocity in the domain is set to zero, representing the still air in the room. The initial temperature of the domain is set to 25°C, which is the room temperature before heating.

In the enclosure, the initial amount of water vapour density has a linear distribution from 0.006 g m<sup>-3</sup> at the roof to 0.013 g m<sup>-3</sup> at the foam surface and for the foam, also a linear density gradient is prescribed. This density gradient approximately equals the same experimental, average, linear density gradient in the foam prior to surface heating. This gradient has a value of 0.02 g m<sup>-3</sup> at the foam bottom which decreases to 0.014 g m<sup>-3</sup> at the the foam-air interface. The higher water density that was prescribed at the foam side of the enclosure-foam interface causes a discontinuity of this amount at the interface. This discontinuity was implemented to compensate for the higher adsorbed moisture in the foam at the surface.

## 4.4.2 Results

In the enclosure, due to a 100 W m<sup>-2</sup> heat generation on the foam, the thermal buoyancy forces rapidly create the natural convection motion at the foam surface (Fig. 4.30). The natural convection motion immediately disrupts the steady state, linear, vertical water density profile in the enclosure (Fig. 4.31) and transports vapour concentration in the enclosure (Fig. 4.32). Fig. 4.33 illustrates the velocity vectors after 120 s in the simulation in the XZ plane. The convective rolls and plumes have a complete 3-D structure (Fig. 4.34 and Fig. 4.34), thus the transport of water vapour in the enclosure air is 3-D. However, the diffusion of water in the foam remains largely 1-D, except for locations which are very close to the surface that have very small 3-D variations (Fig. 4.36 to Fig. 4.38). Moreover, the surface and near surface horizontal temperature and humidity profiles are not symmetric

due to the chaotic nature of natural convection on top of the surface.

In order to compare the simulation results with the experiment, the average water vapour flux from the foam to the enclosure and the vertical water vapour density profile in the foam are studied.

After  $t_x=120$  s into the simulation time, the average surface integral of the water vapour density gradient at depth of 1 mm under the foam was  $\left(\frac{\partial \rho_w}{\partial z}\right)_{t_x}=0.068 \text{ kg m}^{-4}$ . To obtain the water vapour flux from the foam, using Eqn. 4.8 and  $\Gamma_l$ , yields  $j_{t_x}=4.26 \times 10^{-6} \text{ kg m}^{-2} \text{ s}^{-1}$ . This value is close to  $j_3=7.45 \times 10^{-6} \text{ kg m}^{-2} \text{ s}^{-1}$ , which corresponds to the experimental value of the more stable period of  $\Delta t_3$  after surface heating. Since this simulation time ( $t_x$ ) is immediately after heating, it should correspond to the initial period of a high water evaporation ( $\Delta t_2$ ). During this time, the vapour flux measured in the experiment was the highest ( $j_2=3.20 \times 10^{-5} \text{ kg m}^{-2} \text{ s}^{-1}$ ), which shows that the simulation fails to simulate the initial, highly transient, period of rapid evaporation and temperature spikes.

When the vertical water vapour density profiles in the foam at different simulation times are compared with the experimental result (Fig. 4.22), the same non-linearity in the profile, due to natural convection exists, which decreases with time (Fig. 4.39). At  $t=30$  s the vapour gradient near the surface is highest, due to stronger buoyancy forces caused by a larger surface-enclosure temperature difference, however, the near surface water vapour remains almost constant because of the vapour removal from the domain. This process is also observed in the experiments.

In time, the vapour profile in the regolith becomes linear, but with a larger gradient than when natural convection is not present.

Finally, it should be mentioned that, although the numerical model did not completely simulate the experiment process, it provided partial validation for bulk quantities, such as the flux from and the water vapour density profile in the foam.

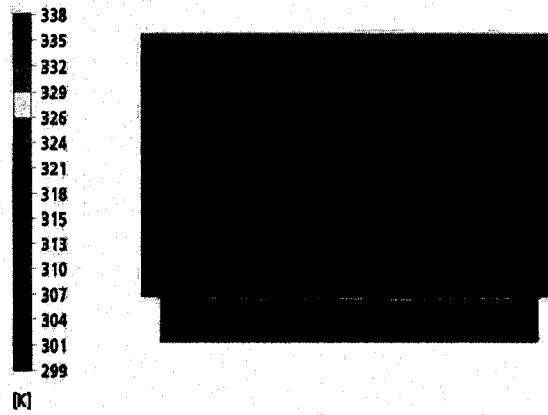


Figure 4.30: Thermal plumes and the transport of heat after 120 s of surface heating is evident from this temperature contour.

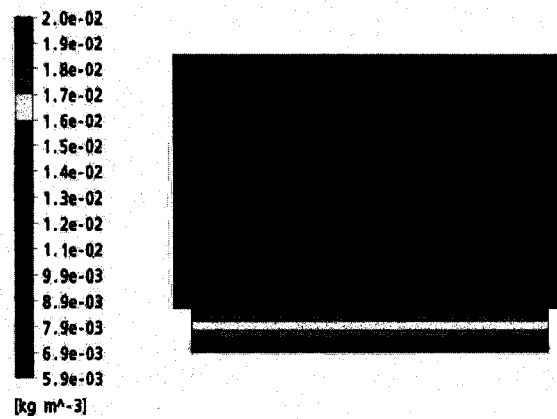


Figure 4.31: Initial water vapour density contour in the domain.



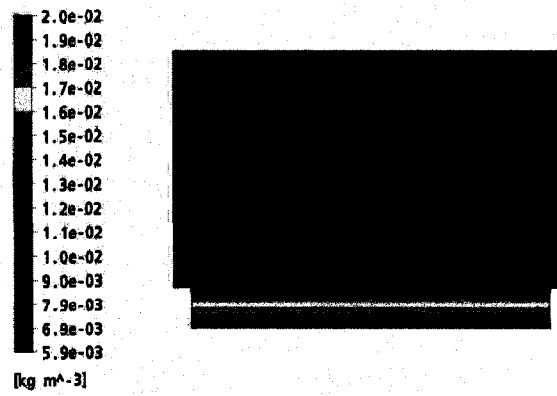


Figure 4.32: Water vapour density contour in the domain after 21 s of surface heating.

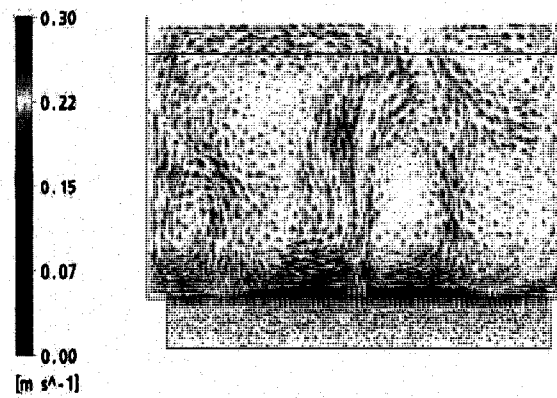


Figure 4.33: Velocity vectors in the XZ plane of the domain after 120 s of surface heating.

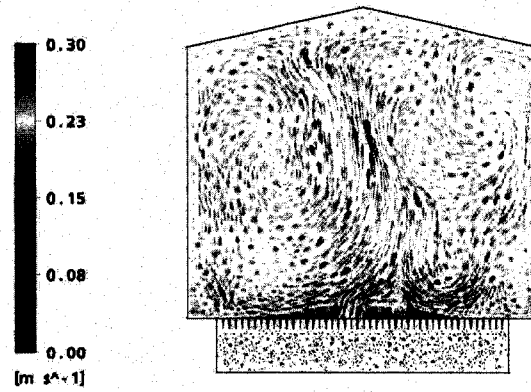


Figure 4.34: Velocity vectors in the YZ plane of the domain after 120 s of surface heating.

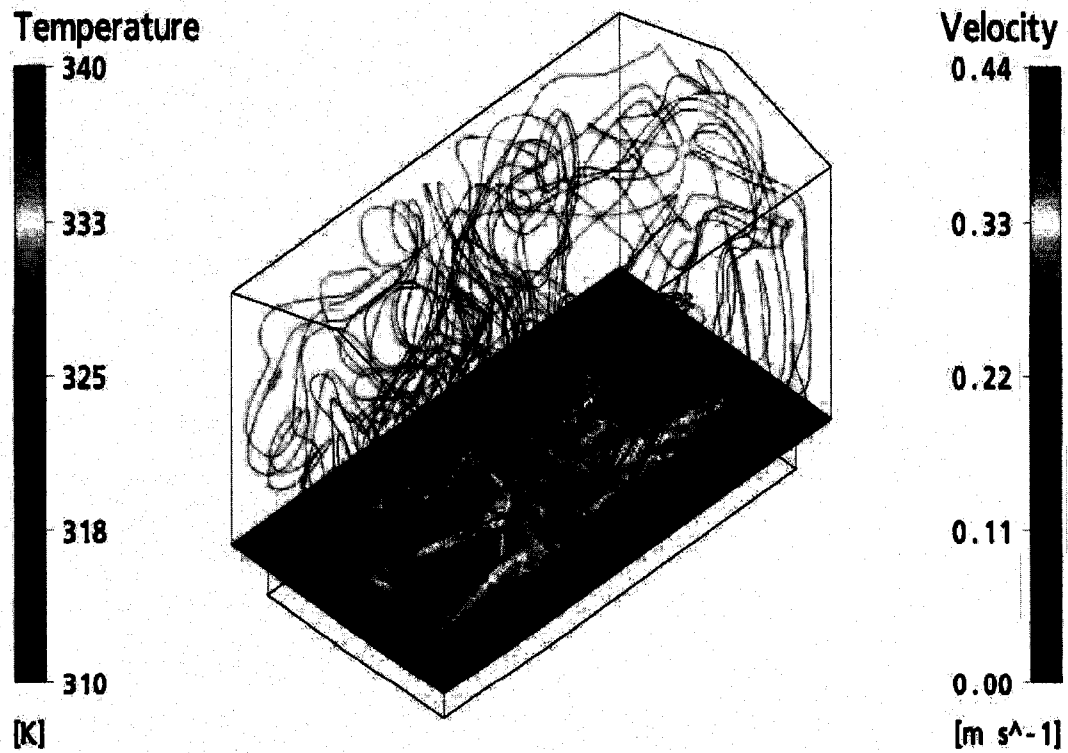


Figure 4.35: Streamlines in the domain and the foam surface temperature variation after 120 s of surface heating.

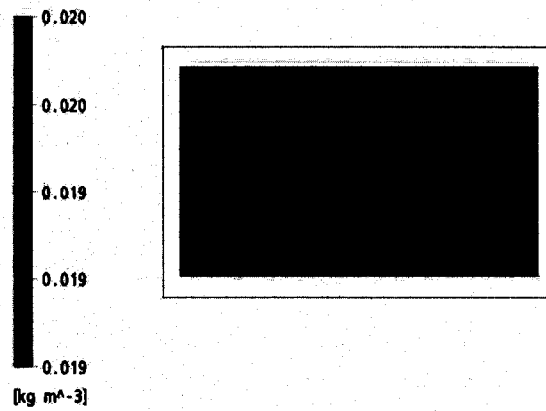


Figure 4.36: Water vapour density contour at a horizontal plane at the bottom of the foam.

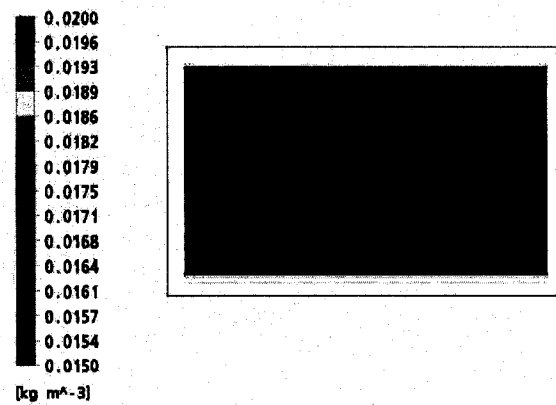


Figure 4.37: Water vapour density contour at a horizontal plane in the middle height of the foam.

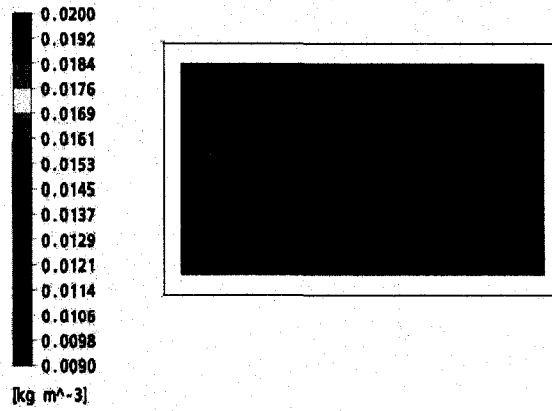


Figure 4.38: Water vapour density contour at a horizontal plane located at 1 mm under the foam surface.

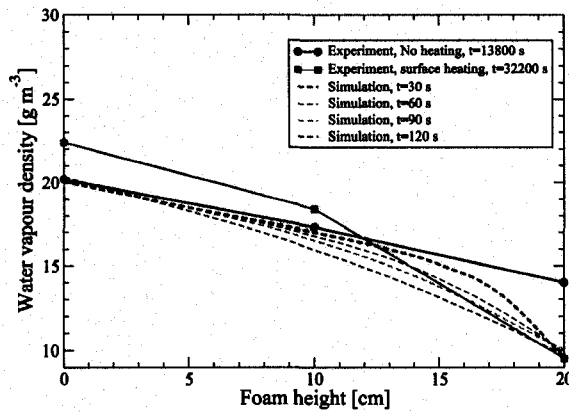


Figure 4.39: Experimental, layer averaged, water vapour density profile in the foam compared to the profiles obtained from the numerical simulation at different times, on a vertical line in the middle of the foam.

# Chapter 5

## Conclusions

In this study, it was shown that local surface flows, such as winds and natural convection, have a significant effect on water vapour mass transfer through a gas saturated porous medium. This type of water vapour transport exists in many industrial and scientific applications. Since the specific application of this study is on water vapour transport in the Martian regolith, it was demonstrated that surface winds and natural convection have a significant effect on the increase of water flux from the regolith to the atmosphere.

In order to model water vapour transport on Mars, firstly, a thorough study on the Martian regolith and the atmospheric properties was performed in Chapter 1. Then the required transport properties were specifically determined for the Phoenix landing site. For the regolith, different methods to assess its properties, such as density, porosity, permeability and thermal conductivity, were discussed. Furthermore, in order to model natural convection at the surface, the heat flux to the surface due to the solar irradiation was calculated for the site.

In Chapter 2, the mathematical modelling of surface flows over a porous medium with water vapour mass transfer was discussed. The mass, momentum and heat transport equations for a non-Newtonian, incompressible fluid were expanded with a simple porous medium model. An additional mass transport equation for water vapour was introduced and to include the effects of natural convection, the addition of a thermal buoyancy force was described. To model turbulence, the  $k-\epsilon$  and the  $k-\omega$  models were selected.

The diffusion mechanism in a porous medium and the flux calculation, along with the evaluation of the effective diffusion coefficient of water vapour in a CO<sub>2</sub> saturated regolith were also noted. The discretization of these governing equations using the Control Volume Method, as implemented in CFX, was briefly outlined.

Finally the special Sherwood number ( $\overline{Sh}^*$ ), which combines sub-surface and atmospheric transport mechanisms, was introduced in order to summarize the parameter study results of the simulations. It was suggested that this number can be used as a coefficient in models of pure regolith or pure atmosphere transport, to obtain a more accurate water vapour flux to the atmosphere. This coefficient includes all the non-linearities and complexities associated with the effects of surface flows on water vapour transfer in the porous regolith. It was mentioned that since a linear water vapour gradient in a local scale is easier to calculate, usually by having the water concentration at the ice-table under the regolith and an arbitrary near surface point in the atmosphere, it can then be simply multiplied by  $\overline{Sh}^*$  to give the real water flux from the regolith.

In Chapter 3, at the beginning, the numerical modelling procedure for surface winds was described and the inlet profiles that were obtained from a 1-D planetary boundary layer [Taylor et al., 2007] were illustrated. The simulation parameter study results were then presented. When winds were present, an increase of 1.5 to 12 times in the water vapour flux from the regolith was observed for the range studied, due to a higher convective transport of water vapour from the surface. It was seen that the regolith has a dominant “resistance” characteristic when subject to a surface flow, that is, at larger regolith thicknesses, the effect of a higher wind velocity on the vapour flux is less.

It was noticed that mostly because of the change in the diffusion coefficient (thus the diffusive transport), an increase of 300 Pa in pressure caused the flux to decrease by a factor of almost 1.5. A decrease of temperature in the domain, also primarily due to the change in the diffusion coefficient, caused a decrease in the flux to the atmosphere. In both cases, as the wind velocity increased, the change in the flux was less significant due to the dominance of diffusion resistance over convection. However, as the wind velocity increases, the difference in the flux value for different pressures at the same velocity increases, whereas the flux difference between different temperature cases decreases.

Moreover, it was found that CFX could not properly simulate turbulence for the surface winds on a porous domain, therefore either the turbulence models diverged or non-physical results using the  $k-\epsilon$  model were observed.

Furthermore, in this chapter, the numerical modelling of natural convection at a local scale on Mars was also described. The CFX solver capability to resolve the thermal buoyant flow over a porous medium was tested with a simple 1-D heat balance at the surface and also partially validated with experimental results from [Ampofo and Karayiannis, 2003] and [Leong et al., 1998]. The growth of the local plumes was observed in a large 2-D domain and in order to select a proper flow model to simulate natural convection at a local 3-D domain, several turbulence models were compared with a laminar model. In the end, the laminar simulations showed results that most closely agreed with the benchmark experiments.

The effect of surface temperature due to solar irradiation, thus the thermal buoyancy force strength, on the water vapour flux to the atmosphere was studied with four surface irradiation values. It was observed that the increase in the incident solar radiation to the surface significantly increases the flux to the atmosphere in a linear manner.

For all simulation cases, the special Sherwood number ( $\overline{Sh}^*$ ) was calculated.

Finally, in Chapter 4 an experiment was described, which was designed to investigate the effect of natural convection on water vapour transport in a porous medium at Earth conditions. The experiment configuration size is similar to the local scale simulations on Mars. This experiment was used to partially validate the numerical simulations of natural convection on Mars. For this purpose, the experiment was numerically simulated and bulk quantities, such as the average flux from the porous medium, the water vapour concentration profile in the porous medium and water vapour density at different locations were compared.

In this experiment, natural convection is created on top of a double layer polyurethane foam (a porous medium) by two radiant heaters, in a closed (but not sealed) enclosure. The foam pieces were located, within a small distance, above water in a tank. Water at the bottom of the tank was the source of water vapour to the foam layers. Humidity and temperature were measured at the foam surface, in the middle of the foam layers, under the foam in the tank, in the enclosure and at control locations in the room. The water weight in the tank

was also measured to record the mass loss due to evaporation at any time.

As a result of natural convection at the foam surface due to an approximately 30 °C temperature rise, the water evaporation rate from the tank increased significantly, especially during a short period of time after surface heating, when the thermal buoyancy forces are higher due to a higher temperature gradient with the enclosure. The evaporation rate during the short time period after heating increased almost 20 times and during the rest of the experiment, it was 4 times higher than when natural convection was not present.

Furthermore in this chapter, the numerical modelling of the experiment was described. As an outcome, when the values of the average water vapour flux from the foam, the water vapour concentration profile in the foam and the surface water vapour density from the numerical simulations were compared with the experimental results, a good agreement was observed.

In summary, the present study analyzed the relative effect of various parameters on the water vapour mass transport from the regolith, revealing the thickness of the regolith layer as the most important parameter at all wind speeds, while the wind speed itself is also an effective parameter at slower winds. As a result of the comparison of all models and boundary conditions, the laminar flow approach was shown to give the best results for simulations under Mars conditions and it is recommended for use in future studies. The mass transport results were summarized in a series of plots of the special Sherwood number that can be used by other researchers in the field for a more accurate calculation of the water vapour flux under known wind conditions and having only vapour concentration values at two points.



# Bibliography

- H. Akima. A new method of interpolation and smooth curve fitting based on local procedures. *J. of the Assoc. for Computing Machinery*, 17(4):589–602, 1970.
- F. Ampofo and T. G. Karayiannis. Experimental benchmark data for turbulent natural convection in an air filled square cavity. *Int. J. Heat and Mass Transfer*, 46:3551–3572, 2003.
- O. Andersson and H. Suga. Thermal conductivity of amorphous ices. *Physical Review B*, 65(140201):140201R, 2002.
- ANSYS. *ANSYS/CFX11 Manual, Theory*. Ansys Inc., Waterloo, Ontario, Canada, 2008.
- J. Appelbaum, G. A. Landis, and I. Sherman. Solar radiation on Mars-update 1991. *Solar Energy*, 50(1):35 – 51, 1993.
- R. E. Arvidson, E. A. Guinness, M. A. Dalebannister, J. Adams, M. Smith, P. R. Christensen, and R. B. Singer. Nature and distribution of surficial deposits in chryse-planitia and vicinity, Mars. *J. Geophys. Res.-Solid earth and planets*, 94(B2):1573 – 1587, 1989.
- V. Badescu. Different strategies for maximum Solar radiation collection on Mars surface. *Acta Astronautica*, 43(7-8):409 – 421, 1998.
- V. R. Baker. Geomorphological evidences for water on Mars. *Elements*, 2:139 – 143, 2006.
- J. L. Bandfield, W. C. Feldman, and H. H. Kieffer. Martian high latitude permafrost depth and surface cover thermal inertia distributions. In *Mars Water Cycle Workshop Abstracts*. CNRS, ESA, 2008.
- T. J. Barth and D. C. Jespersen. The design and application of upwind schemes on unstructured meshes. In *27th Aerospace Sciences Meeting*, number 89-0366 in 1, Reno, NV, 1989. AIAA.

- J. Bear. *Dynamics of Fluids in Porous Media*. American Elsevier Pub. Co., New York, 1972.
- A. Bejan. *Convection Heat Transfer*, chapter External Natural Convection, pages 156–205. John Wiley and Sons, 3rd Avenue, New York, NY, USA, 2 edition, 1995.
- W. V. Boynton, W. C. Feldman, S. W. Squyres, T. H. Prettyman, J. Bruckner, L. G. Evans, R. C. Reedy, R. Starr, J. R. Arnold, D. M. Drake, P. A. J. Englert, A. E. Metzger, I. Mitrofanov, J. I. Trombka, C. d’Uston, H. Wanke, O. Gasnault, D. K. Hamara, D. M. Janes, R. L. Marcialis, S. Maurice, I. Mikheeva, G. J. Taylor, R. Torkar, and C. Shinohara. Distribution of Hydrogen in the near surface of Mars: Evidence for surface ice deposit. *Science*, 297:81–85, 2002.
- S. Chapman and T. Cowling. *The Mathematical Theory of Non-Uniform gases*. Cambridge university press, Newyork, 3 edition, 1970.
- P. R. Christensen. Water at the poles and in permafrost regions of Mars. *Elements*, 2:151 – 155, 2006.
- P. R. Christensen. Regional dust deposits on Mars - physical-properties, age, and history. *J. Geophys. Res.*, 91(B3):3533 – 3545, 1986a.
- P. R. Christensen. The spatial distribution of rocks on Mars. *Icarus*, 68(2):217 – 238, 1986b.
- P. R. Christensen, D. L. Anderson, S. C. Chase, R. N. Clark, H. H. Kieffer, M. C. Mallin, J. C. Pearl, J. Carpenter, N. Bandiera, F. G. Brown, and S. Silverman. Thermal emission spectrometer experiment - Mars-observer mission. *J. Geophys. Res. - Planets*, 97(E5): 7719 – 7734, 1992.
- C. Clauser and E. Huenges. *Thermal Conductivity of Rocks and Minerals*, agu reference shelf 3 Rock Physics and Phase Relations, pages 105 – 126. American Geophysical Union, Washington, D. C., USA, 1995.
- S. M. Clifford. A model for the hydrologic and climatic behavior of water on Mars. *J. Geophys. Res.*, 98(E6):10973 – 11016, 1993.
- B. J. Conrath. Thermal structure of Martian atmosphere during dissipation of dust storm of 1971. *Icarus*, 24(E5):36 – 46, 1975.
- D. A. Crown, K. H. Price, and R. Greeley. Geologic evolution of the east rim of the Hellas Basin, Mars. *Icarus*, 100(1):1 – 25, 1992.

- J. M. DeJager and J. Charles-Edwards. Thermal conductivity probe for soil-moisture determinations. *J. of Experimental Botany*, 20(62):46 – 51, 1969.
- N. M. Dmitriev. Surface porosity and permeability of porous media with a periodic microstructure. *Translated from Izvestiya Rossiiskoi Akademii Mekhanika Zhidkosti i Gaza*, 1(1):79 – 85, 1995.
- K. S. Edgett and P. R. Christensen. The particle-size of Martian aeolian dunes. *J. Geophys. Res. - Planets*, 96(E5):22765–22776, 1991.
- D. Eisenberg and W. Kauzmann. *The structure and properties of water*. Oxford University Press, London, 1969.
- F. P. Fanale, J. R. Salvail, A. P. Zent, and S. E. Postawko. Global distribution and migration of subsurface Ice on Mars. *ICARUS*, 67(1):1 – 18, 1986.
- W. C. Feldman, M. T. Mellon, O. Gasnault, B. Diez, R. C. Elphic, J. J. Hagerty, D. J. Lawrence, S. Maurice, and T. H. Prettyman. Vertical distribution of hydrogen at high northern latitudes on Mars: The Mars Odyssey Neutron Spectrometer. *Geophys. Res. Lett.*, 34(L05201), 2007.
- J. H. Ferziger and M. Peric. *Computational Methods for Fluid Dynamics*, chapter Finite Difference Methods. Springer-Verlag, Berlin, heidelberg, germany, 1 edition, 1996.
- D. Fisher. Personal communication. From the note: how well will Phoenix be able to measure the water vapour flux through the surface of the soil during the mission. how good will be the estimate of net flux?(June 6 2007), 2007.
- D. A. Fisher, D. P. Winebrenner, and H. Stern. Lineations on the White accumulation areas of the residual northern ice cap of Mars: Their relation to the accublation and ice flow hypothesis. *Icarus*, 159(1):39–52, 2002.
- F. M. Flasar and R. M. Goody. Diurnal behaviour of water on Mars. *Planet. Space Sci.*, 24:161–181, 1976.
- Foamex. Permanently compressed reticulated foam polyester or polyether urethane. Report TS-696-FLT-5M, Foamex, 1500 East Second Street, Eddystone, Pa, 19022, 1999.
- F. Forget, F. Hourdin, R. Fournier, C. Hourdin, and O. Talagrand. Improved general circulation models of the Martian atmosphere from the surface to above 80 km. *J. Geophys. Res.*, 104(E10):24155–24175, 1999.

- T. Fouchet, E. Iellouch, N. I. Ignatiev, F. Forget, D. V. Titov, M. Tschimmel, F. Montmessin, V. Formisano, M. Giuranna, A. Maturilli, and T. Encrenaz. Martian water vapor: Mars express PFS/LW observations. In *The 7th international conference on Mars*, number 3150 in 1, 2007.
- B. Gebhart, Y. Jaluria, R. L. Mahajan, and B. Sammakia. *Buoyancy-Induced Flows and Transport*. Hemisphere Pub. Corp., ref. edition edition, 1988.
- E. R. Gilliland, R. Baddour, G. P. Perkinson, and K. Sladek. Diffusion on surfaces. *Ind. Eng. Chem. Fund.*, 13(3):95 – 99, 1974.
- P. Glerasch and R. Goody. The effect of dust on the temperature of the Martian atmosphere. *J. Atmos. Sci.*, 29:400 – 402, 1972.
- M. Grott, J. Helbert, and R. Nadalini. Thermal structure of Martian soil and the measurability of the planetary heat flow. *J. Geophys. Res.*, 112(E09004), 2007.
- G. Guglielmo. Sulla determinazione del coefficiente di diffusione del vapor acqueo per nell'aria, nell'idrogeno e nell'acido carbonico. *Ann. Phys. Chem.*, 6:457–477, 1882.
- R. M. Haberle. Atmospheric effects on the remote determination of thermal inertia on Mars. *Icarus*, 90(2):187 – 204, 1991.
- R. M. Haberle, C. P. McKay, J. Schaeffer, N. A. Cabrol, E. A. Grin, A. P. Zent, and R. Quinn. On the possibility of liquid water on present-day Mars. *J. Geophys. Res.*, 106: 23317 – 23326, 2001.
- R. M. Haberle, F. Montmessin, M. A. Kahre, and J. Schaeffer. The role of the north residual cap in the present Mars water cycle. In *The 7th international conference on Mars*, number 3161 in 1, 2007.
- M. H. Hecht. Metastability of liquid Water on Mars. *ICARUS*, 156:373 – 386, 2002.
- M. H. Hecht. Transient liquid Water near an artificial heat source on Mars. *Mars 2*, 156 (<http://dx.doi.org/10.1555/mars.2006.0006>):83 – 96, 2006.
- C. K. Ho and S. W. Webb. A review of porous media enhanced vapor-phase diffusion mechanisms, models, and data - does enhanced vapor-phase diffusion exist? Report 1198, Sandia National Laboratories, Albuquerque, New Mexico 87185 and Livermore, California 94550, 1996.
- J. Holman. *Heat Transfer*. McGraw-Hill, New York, 8 edition, 1997.

- F. Hourdin, P. L. Van, F. Forget, and O. Talagrand. Meteorological variability and the annual surface pressure cycle on Mars. *J. Atmos. Sci.*, 50:3625–3640, 1993.
- T. L. Hudson, O. Aharonson, N. Schorghofer, C. B. Farmer, M. H. Hecht, and N. T. Bridges. Water vapour diffusion in Mars subsurface environments. *J. Geophys. Res. - Planets*, 112: E05016, 2007.
- F. P. Incropera, D. P. Dewitt, T. L. Bergman, and A. S. Lavine. *Fundamentals of Heat and Mass Transfer*, chapter Natural Convection, pages 571 – 579. John Wiley and Sons, Hoboken, NJ, USA, 6 edition, 2007.
- A. P. Ingersoll. Mars: Occurrence of liquid water. *Science*, 168(3934):972 – 973, 1970.
- B. M. Jakosky. The role of seasonal reservoirs in the Mars water cycle. *Icarus*, 55:1–18, 1983.
- B. M. Jakosky, A. P. Zent, and R. W. Zurek. The Mars water cycle: Determining the role of exchange with the regolith. *Icarus*, 130(1):87–95, 1997.
- D. J. Jerolmack, D. Mohrig, J. P. Grotzinger, D. A. Fike, and W. A. Watters. Spatial grain size sorting in eolian ripples and estimation of wind conditions on planetary surfaces: Application to Meridiani Planum, Mars. *J. Geophys. Res. - Planets*, 111(E5):E12S02, 2006.
- F. S. Johnson. Atmosphere of Mars. *Science*, 150(3702):1445–1448, 1965.
- D. D. Joseph, D. A. Nield, and G. Papanicolaou. Nonlinear equation governing flow in a saturated porous medium. *Water Resour. Res.*, 18(4):1049–1052, 1982.
- M. Kaviany. *Principles of Heat Transfer in Porous Media*. Springer, New York, 1995.
- H. H. Kieffer, S. C. Chase, T. Z. Martin, E. D. Miner, and F. Donpalluconi. Martian north pole summer temperatures: dirty water ice. *Science*, 194:1341 – 1344, 1976.
- H. H. Kieffer, B. M. Jakosky, C. W. Snyder, and M. S. Matthews, editors. *Mars*, chapter Dynamics of the Atmosphere of Mars, pages 835 – 931. The University of Arizona Press, Tuscon, AZ, USA, 1992.
- C. Kleinstreuer. *Two-phase Flow-Theory and Applications*. Taylor and Francis, New York, 2003.

- K. J. Kossacki, W. J. Markiewicz, and M. D. Smith. Surface temperature of Martian regolith with polygonal features: influence of the subsurface water ice. *Plant. Space Sci.*, 51:569–580, 2003.
- R. B. Leighton and B. C. Murray. Behaviour of Carbon Dioxide and other volatiles on Mars. *Science*, 153(3732):136 – 144, 1966.
- M. T. Lemmon, M. J. Wolff, M. D. Smith, R. T. Clancy, D. Banfield, G. A. Landis, A. Ghosh, P. H. Smith, N. Spanovich, B. Whitney, P. Whelley, R. Greeley, S. Thompson, J. F. B. III, and S. W. Squyres. Atmospheric imaging results from the Martian Exploration Rovers: Spirit and Opportunity. *Science*, 306(5702):1753 – 1756, 2004.
- W. H. Leong, K. G. T. Hollands, and A. P. Brunger. Experimental Nusselt numbers for a cubical-cavity benchmark problem in natural convection. *Int. J. Heat and Mass Transfer*, 42(1999):1979 – 1989, 1998.
- C. Leovy. Weather and climate on Mars. *Nature*, 412:245 – 249, 2001.
- S. Litster, J. G. Pharoah, G. McLean, and N. Djilali. Computational analysis of heat and mass transfer in a micro-structured PEMFC cathode. *J. of Power Sources*, 156:334 – 344, 2006.
- J. R. Lloyd and W. R. Moran. Natural convection adjacent to horizontal surfaces of various planforms. *J. Heat Trans.-Transactions of the ASME*, 96(4):443–447, 1974.
- J. R. Lloyd and E. M. Sparrow. On the instability of natural convection flow on inclined plates. *J. Fluid Mech.*, 42:465 – 470, 1970.
- M. C. Malin. Density of Martian north polar layered deposits - implications for composition. *Geophys. Res. Lett.*, 13(5):444–447, 1986.
- M. C. Malin and K. S. Edgett. Evidence for recent groundwater seepage and surface runoff on Mars. *Science*, 288:2330, 2000.
- T. Marrero and E. Mason. Gaseous diffusion coefficients. *J. Phys. Chem. Ref. Data*, 1(1): 3–118, 1972.
- J. Marti and K. Mauersberger. A survey and new measurements of ice pressure at temperatures between 170 and 250 k. *Geophys. Res. Lett.*, 20(5):363–366, 1993.
- E. A. Mason and A. P. Malinauskas. *Gas Transport in Porous Media: The Dusty-Gas Model*. Elsevier, 1983.

- K. Mauersberger and D. Krankowsky. Vapor pressure above ice at temperatures below 170 K. *Geophys. Res. Lett.*, 30(3):1121, 2003.
- M. T. Mellon and B. M. Jakosky. High-resolution thermal inertia mapping from the Mars Global Surveyor Thermal Emission Spectrometer. *Icarus*, 148(2):437–455, 2000.
- M. T. Mellon and B. M. Jakosky. Geographic variations in the thermal and diffusive stability of ground ice on Mars. *J. Geophys. Res.*, 98(E2):3345–3364, 1993.
- M. T. Mellon and R. J. Phillips. Recent gullies on Mars and the source of liquid water. *J. Geophys. Res.*, 106:23165–23180, 2001.
- M. T. Mellon, B. M. Jakosky, and S. E. Postawko. The persistence of equatorial ground ice on Mars. *J. Geophys. Res.*, 102(E8):19357–19369, 1997.
- M. T. Mellon, W. C. Feldman, and T. H. Prettyman. The presence and stability of ground ice in the southern hemisphere of Mars. *Icarus*, 169(2):324–340, 2004.
- I. G. Mitrofanov, D. Animov, A. S. Kozyrev, M. L. L. A. B. Sanin, V. Tretyakov, A. Krylov, V. Shvetsov, W. V. Boynton, D. Hamara, C. Shinohara, and R. S. Saunders. Maps of subsurface Hydrogen from the High Energy Neutron Detector, Mars Odyssey. *Science*, 297(78):78–81, 2002.
- I. G. Mitrofanov, M. T. Zuber, M. L. Litvak, W. V. Boynton, D. E. Smith, D. Drake, D. Hamara, A. S. Kozyrev, A. B. Sanin, C. Shinohara, R. S. Saunders, and V. Tretyakov. CO<sub>2</sub> snow depth and subsurface water-ice abundance in the northern hemisphere of Mars. *Science*, 300:2081–2084, 2003.
- H. J. Moore and B. M. Jakosky. Viking landing sites, remote-sensing observations, and physical-properties of Martian surface materials. *Icarus*, 81(1):164–184, 1989.
- T. F. Morey and D. N. Gorman. Development of the Viking Mars Lander thermal control subsystem design. *J. of spacecrafts and rockets*, 13(4):229–236, 1976.
- J. R. Murphy and S. Nelli. Mars Pathfinder convective vortices: Frequency of occurrence. *Geophys. Res. Lett.*, 29(23):2103, 2002.
- O. K. Nusier and N. H. Abu-Hamdeh. Laboratory techniques to evaluate thermal conductivity for some soils. *Heat and Mass Transfer*, 39(2):119–123, 2003.
- S. L. Painter. Marsflo: A general tool for simulating hydrological processes in the subsurface of Mars. In *Sixth International Conference on Mars*, number 3161 in 1, 2003.

- S. L. Painter and R. E. Grimm. Three-phase simulations of moisture movement in the Martian subsurface. In *The 7th international conference on Mars*, number 3272 in 1, 2007.
- A. R. Peterfund. *Contemporary aeolian processes on Mars: Local Dust Storms*. PhD thesis, Arizona state university, 1985.
- C. D. Peters-Lidard, E. Blackburn, X. Liang, and E. F. Wood. The effect of soil thermal conductivity parameterization on surface energy fluxes and temperatures. *J. Atmos. Sci.*, 55(7):1209–1224, 1998.
- J. B. Pollack, D. S. Colburn, F. M. Flasar, R. Kahn, C. E. Carlston, and D. Pidek. Properties and effects of dust particles suspended in the Martian atmosphere. *J. Geophys. Res.*, 84 (NB6):2929–2945, 1979.
- J. B. Pollack, R. M. Haberle, J. Schaeffer, and H. Lee. Simulation of the general circulation of Martian atmosphere I: Polar processes. *J. Geophys. Res.*, 95(B2):1447–1473, 1990.
- M. A. Presley and P. R. Christensen. Thermal conductivity measurements of particulate materials, 1, a review. *J. Geophys. Res.*, 102(E4):6535–6549, 1997a.
- M. A. Presley and P. R. Christensen. Thermal conductivity measurements of particulate materials, 2, results. *J. Geophys. Res.*, 102(E4):6551–6566, 1997b.
- M. A. Presley and P. R. Christensen. The effect of bulk density and particle size sorting on the thermal conductivity of particulate materials under Martian atmospheric pressures. *J. Geophys. Res.*, 102(E4):9221–9229, 1997c.
- L. Prieto. A numerical model of local water vapour transport. Master's thesis, University of Alberta, 2006.
- R. Reid, J. Prausnitz, and B. Poling. *The Properties of Gases and Liquids*. McGraw-Hill, New York, 4 edition, 1987.
- M. I. Richardson and R. J. Wilson. Investigation of the nature and stability of the Martian seasonal water cycle with a general circulation model. *J. Geophys. Res.*, 107(E5):5031–5063, 2002.
- M. I. Richardson, R. J. Wilson, and A. V. Rodin. Water ice clouds in the Martian atmosphere: General circulation model experiments with a simple cloud scheme. *J. Geophys. Res.*, 107(E9):5064–5099, 2002.



- J. A. Ryan and R. M. Henry. Mars atmospheric phenomena during major dust storms, as measured at surface. *J. Geophys. Res.*, 84(B6):2821–2829, 1979.
- C. N. Satterfield. *Mass transfer in Heterogeneous Catalysis*, pages 1–77. R. E. Krieger Pub. Co., Malabar, Fla, 1981.
- H. Savijarvi. Mars boundary layer modeling: Diurnal moisture cycle and soil properties at the Viking lander 1 site. *Icarus*, 117:120–127, 1995.
- N. Schorghofer and O. Aharonson. Stability and exchange of subsurface ice on Mars. *J. Geophys. Res. - Planets*, 110(E5):E05003, 2005.
- D. W. G. Sears and S. R. Moore. On laboratory simulation and the evaporation rate of water on Mars. *Geophys. Res. Lett.*, 32(L16202), 2005.
- SensirionAG. Datasheet SHT7x. Data sheet V.4.0, Sensirion company AG, Staefa, ZH, Switzerland, 2008. [www.sensirion.com](http://www.sensirion.com).
- R. P. Sharp. Mars - fretted and chaotic terrains. *J. Geophys. Res.*, 78(20):4073–4083, 1973a.
- R. P. Sharp. Mars - troughed terrain. *J. Geophys. Res.*, 78(20):4063–4072, 1973b.
- R. P. Sharp. Mars - south polar pits and etched terrain. *J. Geophys. Res.*, 78(20):4222–4230, 1973c.
- H. G. Sizemore and M. T. Mellon. Effects of soil heterogeneity on Martian ground-ice stability and orbital estimates of ice table depth. *Icarus*, 185:358 – 369, 2006.
- H. G. Sizemore and M. T. Mellon. Laboratory measurements of tortuosity and permeability in Mars analog soils. In *The 7th international conference on Mars*, number 3055 in 1, 2007.
- G. A. Slack. Thermal conductivity of ice. *Physical review B*, 22(6):3065 – 3071, 1980.
- M. D. Smith. Mars water vapor climatology from MGS/TES. In *Mars Water Cycle Workshop Abstracts*. CNRS, ESA, 2008.
- P. H. Smith, M. J. Wolff, M. T. Lemmon, N. Spanovich, D. Banfield, C. J. Budney, R. T. Clancy, A. Ghosh, G. A. Landis, P. Smith, B. Whitney, P. R. Christensen, and S. W. Squyres. First atmospheric science results from the Mars exploration rovers Mini-TES. *Science*, 306:1750 – 1753, 2004.
- R. Smoluchowski. Mars: Retention of ice. *Science*, 159(3821):1348 – 1350, 1968.

- R. B. Stull. *An Introduction to Boundary Layer Meteorology*, volume 13 of *Atmospheric and Oceanographic Sciences Library*,. Dordrecht, 1988.
- R. Sullivan, D. Banfield, J. F. B. III, W. Calvin, D. Fike, M. Golombek, R. Greeley, J. Grotzinger, K. Herknhoff, M. Malin, D. Ming, L. A. Soderblom, S. W. Squyres, S. Thompson, W. A. Watters, C. M. Weitz, and A. Yen. Aeolian processes at the Mars Exploration Rover Meridiani Planum landing site. *Nature*, 436(7047):58–61, 2005.
- K. L. Tanaka. Sedimentary history and mass flow structures of chryse and acidalia planitiae, Mars. *J. Geophys. Res. - Planets*, 102(E2):4131–4149, 1997.
- K. L. Tanaka and G. J. Leonard. Geology and landscape evolution of the hellas region of mars. *J. Geophys. Res. - Planets*, 100(E3):5407–5432, 1995.
- P. A. Taylor, P.-Y. Li, D. V. Michelangeli, J. Pathak, and W. Weng. Modelling dust distributions in the atmospheric boundary layer on Mars. *Boundary Layer Meteorology, Special Issue*, 2007. in print, DOI 10.1007/s10546-007-9158-9.
- W. Wagner and A. Pruß. The IAPWS formulation 1995 for the thermodynamic properties of ordinary water substance for general and scientific use. *Journal of Physical and Chemical Reference Data*, 31(2):387–535, 2002.
- D. Wallace and C. Sagan. Evaporation of ice in planetary-atmospheres - ice-covered rivers on Mars. *Icarus*, 39(3):385 – 400, 1979.
- E. W. Washburn, editor. *International Critical Tables of Numerical Data, Physics, Chemistry and Technology (1st Electronic Edition)*, volume V, ebook Interdiffusion of gases and vapors, pages 62–63. Knovel, 2003.
- D. C. Wilcox. *Turbulence Modeling for CFD*. DCW industries, La Canada, CA, USA, 1993.
- D. R. Wing and G. L. Austin. Description of the university of Auckland global Mars mesoscale meteorological model. *ICARUS*, 185:370 – 382, 2006.
- A. Winkelmann. uber den einfluss der temperatur auf die verdampfung and auf die diffusion von dampfen. *Ann. Phys. Chem.*, 272(1):93 – 114, 1889.
- C. L. Yaws, editor. *Chemical Properties Handbook*, chapter Heat Capacity of Gas, pages 30–31. Mc Graw-Hill, 1999a.
- C. L. Yaws, editor. *Chemical Properties Handbook*, chapter Thermal Conductivity of Gas, pages 505–506. Mc Graw-Hill, 1999b.

- C. L. Yaws, editor. *Chemical Properties Handbook*, chapter Viscosity of Gas, pages 452–453. Mc Graw-Hill, 1999c.
- A. P. Zent, F. P. Fanale, J. R. Salvail, and S. E. Postawko. Distribution and state of H<sub>2</sub>O in the high-latitude shallow subsurface of Mars. *ICARUS*, 67(1):19 – 36, 1986.
- N. G. Zharkova, V. V. Prokkoev, A. K. Rebrov, and V. N. Yarygin. Nonequilibrium expansion of Carbon Dioxide gas at retardation temperatures up to 1200 K. *Translated from Zhurnal Prikladnoi Mekhaniki i Tekhnicheskoi Fiziki*, 1(5):41 – 45, 1976.
- R. W. Zurek. Martian great dust storms - an update. *Icarus*, 50:288 – 310, 1982.

# **Appendix A**

## **Humidity/Temperature Sensor Calibration Data**

# Appendix A

## Humidity/Temperature Sensor Calibration Data

In this appendix, the linear regression coefficients (a and b) are provided for the temperature measurement of the SHT71 sensors. These coefficients fit the equation  $T_{real} = aT_{read} + b$ .

Name	a	b	Name	a	b
CH01	1.01491	-0.87292	CH17	0.98498	1.06286
CH02	1.01023	-0.83745	CH18	0.99611	0.18669
CH03	1.01203	-1.09280	CH19	0.99539	0.41808
CH04	1.00623	-0.42527	CH20	0.99850	0.09315
CH05	1.01085	-0.75272	CH21	0.98834	0.72446
CH06	1.02006	-0.46725	CH22	0.99189	0.49369
CH07	1.00511	-0.13317	CH23	1.02200	-0.29672
CH08	0.99972	-0.22358	CH24	1.01037	0.70704
CH09	1.00160	0.16108	CH25	0.98360	0.96628
CH10	0.98732	0.00457	CH26	1.02717	0.06981
CH11	0.99780	0.22373	CH27	1.03002	-0.14543
CH12	0.99668	0.54617	CH28	1.02989	0.17523
CH13	1.01377	-0.40548	CH29	1.05870	-0.94569
CH14	1.02032	-0.51018	CH30	1.02373	-0.14259
CH15	0.99581	0.05099	CH31	1.03587	-0.10044
CH16	0.98961	0.91282	CH32	1.02876	-0.06516

Table A.1: Regression coefficients for sensors 1 to 32.

Name	a	b	Name	a	b
CH33	1.01195	-0.47432	CH49	0.99651	0.58280
CH34	0.99519	-0.05464	CH50	1.02822	-0.20472
CH35	1.01678	-0.75171	CH51	0.99564	0.08090
CH36	1.01705	-0.56891	CH52	1.00466	0.36130
CH37	0.99432	0.22509	CH53	1.01558	0.26844
CH38	0.99030	0.18104	CH54	1.01012	0.63644
CH39	0.99509	0.16050	CH55	1.03658	-0.09394
CH40	0.99206	-0.05133	CH56	1.03169	-0.44089
CH41	0.99862	-0.23322	CH57	1.03384	-0.11844
CH42	1.01477	-0.08761	CH58	1.03775	-0.45229
CH43	1.02552	-0.42747	CH59	1.05200	-0.68830
CH44	1.01286	0.02206	CH60	1.02525	-0.06181
CH45	0.99820	0.40554	CH61	1.02604	-0.07028
CH46	0.99933	0.45771	CH62	1.02478	0.02960
CH47	1.00349	0.21744	CH63	1.02701	0.00961
CH48	1.00981	0.06775	CH64	1.02086	0.19527

Table A.2: Regression coefficients for sensors 33 to 64.

Name	a	b	Name	a	b
CH65	0.99011	0.14319	CH81	1.01089	0.28775
CH66	1.00599	0.11161	CH82	1.01705	0.48921
CH67	1.00313	-0.05173	CH83	1.01495	0.24030
CH68	1.02568	-0.73838	CH84	1.03545	-0.13096
CH69	1.00599	0.07985	CH85	1.01794	0.39649
CH70	0.99456	0.26198	CH86	1.02306	0.28417
CH71	1.01628	-0.17629	CH87	1.02880	0.24705
CH72	1.02827	-0.81213	CH88	1.03407	-0.08487
CH73	0.99996	-0.06393	CH89	1.02286	0.12273
CH74	1.02297	-0.49844	CH90	1.00855	0.22935
CH75	1.00859	0.14640	CH91	1.02927	-0.01285
CH76	1.00576	0.23846	CH92	1.01040	0.43007
CH77	1.01168	0.14828	CH93	1.03713	-0.25648
CH78	1.01275	-0.06728	CH94	1.01428	0.15959
CH79	1.03188	-0.46456	CH95	1.01934	-0.05148
CH80	1.00464	0.42269	CH96	1.01687	0.16339

Table A.3: Regression coefficients for sensors 65 to 96.

Name	a	b	Name	a	b
CH97	1.01223	-1.80614	CH113	1.01568	-1.16128
CH98	0.98151	-1.09851	CH114	1.00616	-1.08165
CH99	1.01250	-1.99709	CH115	0.99174	-0.54411
CH100	0.99094	-1.52077	CH116	0.99271	-0.71808
CH101	1.01093	-1.59288	CH117	1.00432	-0.77096
CH102	0.98780	-1.37238	CH118	1.01817	-0.69132
CH103	1.01384	-1.82793	CH119	1.01802	-1.21834
CH104	0.98696	-1.28145	CH120	1.01698	-0.87922
CH105	1.00699	-1.56465	CH121	1.00027	-0.46621
CH106	0.99930	-1.60583	CH122	0.99827	-0.88384
CH107	0.99867	-0.97718	CH123	1.00565	-1.04000
CH108	0.98537	-0.48188	CH124	1.02195	-1.26125
CH109	0.98863	-1.17693	CH125	1.00307	-0.86728
CH110	0.99643	-1.47608	CH126	0.99768	-0.79938
CH111	1.01720	-1.83981	CH127	1.00902	-0.99291
CH112	0.99941	-1.01770	CH128	1.01733	-1.05427

Table A.4: Regression coefficients for sensors 97 to 128.